# ”Heusler compounds for thermoelectric applications”

Dissertation
zur Erlangung des Grades
”Doktor der Naturwissenschaften”
im Promotionsfach Chemie
am Fachbereich Chemie, Pharmazie und Geowissenschaften
der Johannes Gutenberg-Universität
in Mainz

Michael Schwall
geb. in Mayen
Mainz, den 28.09.2012

**Contents**

## I. INTRODUCTION

The demands for energy is leading to social and political conflicts in the world. For example, the limited resources of fossil fuels causing a dependence on the oil conveying countries in the world, leading to political discords.
One way to save energy is to increase the efficiency of a process. In the field of thermoelectricity waste heat is used to produce electricity, this leads to an improvement of the efficiency. Heusler compounds with $C1_b$ structure with the general formula $XYZ$ ($X, Y$ = transition

metal, $Z$ = main group element) are in focus of the present thermoelectric research.[1–14] Their mechanical and thermal stability is exceptional in comparison to the commonly used thermoelectric materials.[15] The possibility to substitute small amounts of elements from the parent compound without destructing the lattice structure allows tuning the electronic properties.[16, 17] This tunability also allows to avoid the use of toxic and expensive elements. The reported thermoelectric Heusler compounds exhibit high electrical conductivity and moderate values of the Seebeck coefficients, which lead to a high powerfactor.[18] The disadvantage of Heusler compounds is their high thermal conductivity. Introducing mass disorder on the X-site lattice is one effective way to produce additional phonon scattering and with it to decrease the thermal conductivity.[19, 20] Another approach is to implement a nano or micro structure in the thermoelectric material. This can be achieved by phase separation, composite materials, pulverization with additional spark plasma sintering or by a complex lattice structure.[21, 22]

In the first part of this work, the influence of element substitutions on the $Zr_{0.5}Hf_{0.5}NiSn$ system was investigated, to obtain the knowledge on how to optimize the electronic properties of the Heusler compounds with $C1_b$ structure. In line with this, the change of the electronic structure was investigated and a possible mechanism is predicted. In the second part of this work, the phenomenon of phase separation was investigated. First, by applying a phase separation in the well-known system $Co_2MnSn$ [23] and subsequently by systematic investigations on the $Ti_xZr_yHf_zNiSn$. In the third part, the results from the previous parts before were used to produce and explain the best reported Heusler compound with $C1_b$ structure exhibiting a Figure of Merit of ZT= 1.2 at 830 K.

# II. THEORETICAL BACKGROUND

## A. Thermoelectric effects

### 1. *Seebeck effect*

The simplest way to explain the Seebeck effect is to have a look on a schematic thermoelectric circuit consisting of two materials A and B (Figure 1). These materials, which later can be named thermoelectric legs, are connected electrically in series and thermally parallel. If a temperature $T_C$ and a temperature $T_H$ with $T_H > T_C$ is applied at the two junctions, a voltage is measurable at V.[24–26]

$$V = \alpha(T_H - T_C) => \alpha = \frac{V}{\Delta T} \tag{1}$$

With $\alpha$ as the differential Seebeck coefficient between the two junctions. This relationship is linear for small differences between the temperatures and can be written as:

$$\alpha = \frac{\delta V}{\delta T} \tag{2}$$

The sign of the Seebeck coefficient $\alpha$ is per definition related to the sign of the established voltage.[24]

### 2. *Peltier effect*

If, contrary to the Seebeck effect, a current is applied to the circuit, one junction will be heated and the other will be cooled [24–26]. This effect is named after Jean Peltier and the relationship is given as:

$$\pi = \frac{I}{Q}, \tag{3}$$

with I as the applied current and Q as the cooling or heating rate. This two effects are connected via the Kelvin relation:

$$\alpha = \frac{\pi}{T} \tag{4}$$

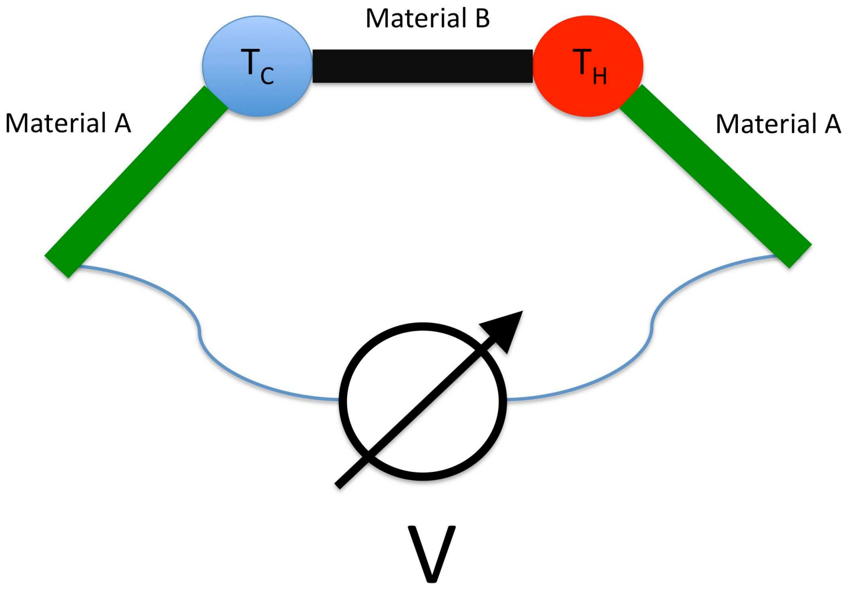

FIG. 1: Schematic hot and cold junction of two materials A and B [24, 25].

### B. Figure of Merit

The thermoelectric Figure of Merit $ZT$ is an instrument to evaluate the efficiency of a thermoelectric material[24, 26, 27].

$$ZT = \frac{\alpha^2\sigma}{\kappa} \cdot T = \frac{\alpha^2}{\rho\kappa} \cdot T, \tag{5}$$

with $\alpha$ as the Seebeck coefficient, $\sigma$ as the electrical conductivity, $\kappa$ as the thermal conductivity and $\rho$ as the electrical resistivity. The Figure of Merit is included in the definition of the maximum thermoelectric efficiency $\eta_{max}$ via

$$\eta_{max} = \frac{T_H - T_C}{T_H} \frac{\sqrt{1 + \overline{ZT}} - 1}{\sqrt{1 + \overline{ZT}} + \frac{T_C}{T_H}}, \tag{6}$$

with $T_C$ as the temperature at the cold junction, $T_H$ as the temperature at the hot junction and $\overline{ZT}$ as Figure of Merit, which takes the n-type and p-type material properties into account and uses the average temperature between the hot and the cold junction $\overline{T}$[27],

$$\overline{ZT} = \frac{(\alpha_p - \alpha_n)^2 \overline{T}}{(\sqrt{\rho_n \kappa_n} + \sqrt{\rho_p \kappa_p})^2}. \tag{7}$$

### C. Transport theory

#### 1. *Boltzmann transport theory: the relaxation time approximation*

The Boltzmann transport equation describes the statistical distribution of carriers in a certain volume.[24, 28, 29] It gives respect to the diffusion, external fields and scattering processes. The relaxation approximation assumes that the mean free path $\Lambda$ of an excitation is longer than its wavelength $\lambda$.

$$\Lambda > \lambda \tag{8}$$

By solving the Boltzmann equation in the relaxation approximation the currents $J_i$ are observed.

$$J_i = \sigma_{ij} E_i \ + \nu_{ij} \nabla_j T \ + \sigma_{ijk} E_j H_k + ... \tag{9}$$

with

$$\sigma_{ij}(T) = \frac{-e^2}{4\pi^3 V} \int\int \tau_k \nu_i(k) \nu_j(k) \frac{dS}{\nabla_k E(k)} \frac{\partial f(E, \mu, T)}{\partial E} dE \tag{10}$$

and

$$\nu_{ij}(T) = \frac{-e^2}{4\pi^3 V}\int\int \tau_k \nu_i(k)\nu_j(k)\frac{dS}{\nabla_k E(k)}(E-\mu)\frac{\partial f(E,\mu,T)}{\partial E}dE \tag{11}$$

In these equations $e$ is the elementary charge, $V$ the investigated volume, $\tau$ the relaxation time, $\nu$ the spatial velocities, $S$ the entropy, $E$ the electric field, $\mu$ the chemical potential and $T$ the temperature.[28] Out of these equations we can receive the electric current as:

$$J = \sigma E \tag{12}$$

this leads in comparison with equation 9 to the electrical conductivity tensor:

$$\sigma = \sigma_{ij}(T) \tag{13}$$

Also the Seebeck coefficient $\alpha$ can be determined out of the equation 9:

$$\alpha = \frac{\nu_{ij}(T)}{\sigma_{ij}(T)} \tag{14}$$

Analogous the thermal conductivity $\kappa$ is obtained [28],

$$\kappa = \frac{ST^2 + T\nu_{ij}(T)E}{\nabla T} + \frac{\nu_{ij}(T)^2 T}{\sigma_{ij}(T)}. \tag{15}$$

### 2. *Seebeck coefficient and the electrical conductivity*

The commonly used equation in the field of thermoelectricity is the Mott equation, into which by using the approximation of a single parabolic band the Boltzmann equation is extracted to [24, 25, 27, 30–32]:

$$\alpha = \frac{\pi^2 k_b^2}{3e} T \left\{\frac{d[ln(\sigma(\varepsilon))]}{d\varepsilon}\right\}_{\varepsilon=\varepsilon_F}, \tag{16}$$

with $k_b$ as the Boltzmann constant, $e$ the elementary charge and $\sigma(E)$ the energy-dependent electrical conductivity. In this equation the conductivity is calculated as if the Fermi level is at $\varepsilon$. For infinitesimal energy steps the electrical conductivity is proportional to the density of states (DOS), which means that $\frac{d[ln(\sigma(\varepsilon))]}{d\varepsilon}_{\varepsilon=\varepsilon_F}$ is the slope of the DOS at the Fermi energy. Therefore the Seebeck coefficient is dependent on the slope of the DOS($\varepsilon_F$) at the Fermi energy [27, 29, 30, 32].

The electrical conductivity is given by:

$$\sigma = ne\mu, \tag{17}$$

with $n$ as the carrier concentration, $e$ the elementary charge and $\mu$ the carrier mobility. By implementation of the electrical conductivity $\sigma$ to the Mott equation, we get:

$$\alpha = \frac{\pi^2 k_b^2}{3e} T \left\{ \frac{1}{n} \frac{dn(\varepsilon)}{d\varepsilon} + \frac{1}{\mu} \frac{d\mu(\varepsilon)}{d\varepsilon} \right\}_{\varepsilon = \varepsilon_F} . \tag{18}$$

This shows the dependence of the Seebeck coefficient on the carrier mobility $\mu$ as well as the carrier concentration. To simplify the equation 18 two more approximations have to be applied [27, 29, 30, 32]. For a degenerate semiconductor, which is a semiconductor that acts like a metal with pure acoustic phonon scattering of the carriers, because of a very high level of doping, the equation is:

$$\alpha = \frac{8\pi^2 k_b^2}{3eh^2} T m^* \left( \frac{\pi}{3n} \right)^{\frac{2}{3}} , \tag{19}$$

with $h$ as Planck‘s constant and $m^*$ as the effective mass. The values of $m^*$ and $n$ are dependent on $\varepsilon_F$, which determines the degeneracy of the material. Thereby, this equation underlines the problem of the optimization of the Seebeck coefficient without decreasing the carrier concentration $n$, which would decrease the electrical conductivity (see equation 17) and simultaneously the Figure of Merit. The dependence of the Seebeck coefficient on the carrier concentration for a degenerate semiconductor is given in equation 19.[27, 30, 32] The dependence for a non-degenerate semiconductor is

$$\alpha \propto \left( \frac{1}{ln(n)} \right) . \tag{20}$$

As seen above the Seebeck coefficient is dependent on the carrier concentration (see equations 20,19,18) [27, 30]. From equation 19 it can be observed that $\alpha$ also depends on the effective mass $m^*$ of carriers, what means that a high density of states at the Fermi energy, what usually means a high $m^*$, leads to high Seebeck coefficients [33]. In equation 18 the Seebeck coefficient is also dependent on the mobility $\mu$, which is given as

$$\mu = \frac{e}{m^*} \overline{\tau}, \tag{21}$$

with $e$ as the elemental charge, $m^*$ as the carrier effective mass and $\overline{\tau}$ as the average scattering time.[34, 35] Thus a high effective mass leads to a high Seebeck coefficient and a low mobility, what means a low electrical conductivity (see equation 17). This shows that a balance between the effective mass, high Seebeck coefficients, and a low mobility, i.e. low electrical conductivity, has to be found. If the equations 17, 19 and 20 are combined, the dependence of the Seebeck coefficient on the electrical conductivity is recognizable. For a degenerate semiconductor

$$\alpha \propto \left(\frac{\mu e}{\sigma}\right)^{\frac{2}{3}} \propto \left(\frac{e^2\overline{\tau}}{m^*\sigma}\right)^{\frac{2}{3}}, \tag{22}$$

and for a non-degenerate semiconductor

$$\alpha \propto \left(\frac{1}{ln(\frac{\mu e}{\sigma})}\right) \propto \left(-ln(\frac{e^2\overline{\tau}}{m^*\sigma})\right). \tag{23}$$

If the mobility is constant, what means that the carrier effective mass and the scattering time do not change, $\alpha$ is only dependent on the electrical conductivity or the carrier concentration (see equation 17). In Figure 2 the resulting development for a degenerate and non-degenerate semiconductor is shown.[27, 32, 34, 35]

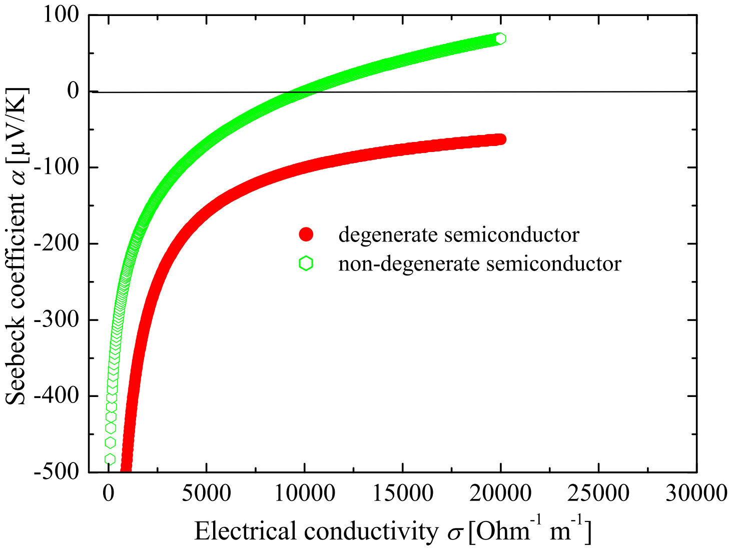

FIG. 2: Electrical conductivity dependence on the Seebeck coefficient for a degenerate semiconductor and a non-degenerate semiconductor.

The sign of the Seebeck coefficient is determined by the sort of carrier, which causes the conduction. For large Seebeck coefficients only one sort of carrier is present, but for small Seebeck coefficients the bipolar conduction, where holes and electrons participate in the conduction, is observed. The resulting Seebeck coefficient of the bipolar conduction is

$$\alpha = \frac{\alpha_e\sigma_e + \alpha_h\sigma_h}{\sigma_e + \sigma_h}, \tag{24}$$

with $\alpha_{e/h}$ as the contribution of the holes $h$ and electrons $e$ to the Seebeck coefficient and $\sigma_{e/h}$ as the contributions to the electrical conductivity [27, 30].

Energy in case of heat can be carried via electrical carriers - holes and electrons - lattice vibrations - phonons - or other excitations. The thermal conductivity consists of the lattice contribution to the thermal conductivity $\kappa_l$ and the electronic contribution to the thermal conductivity $\kappa_e$,

$$\kappa = \kappa_l + \kappa_e. \tag{25}$$

For a metal the electronic contribution is dominating, for an insulator the lattice contribution is dominating [34, 36].

### The electronic contribution to the thermal conductivity $\kappa_e$

Via the Boltzmann transport theory and the free electron theory the electronic contribution to thermal conductivity is given by the Wiedemann-Franz law [29, 36, 37]:

$$\kappa_e = L\sigma T, \tag{26}$$

with $L$ as the Lorenz number, which is $2.4453 \cdot 10^{-8}$ W Ohm $K^{-2}$ [29, 37] for metals and highly degenerate semiconductors. Under the assumption of acoustic phonon scattering the Lorenz number for non-degenerate semiconductors is $1.4866 \cdot 10^{-8}$ W Ohm $K^{-2}$. For temperatures high above the Debye temperature $\theta_D$ (T $\gg \theta_D$) and below the Debye temperature (T $\ll \theta_D$) the Wiedemann-Franz law gives proper values for $\kappa_e$. At intermediate temperatures the law fails due to inelastic phonon scattering of the charge carriers, which leads to a lower value of the Lorenz number.

### The lattice thermal conductivity $\kappa_l$

The heat in solids is transferred by vibrations of the lattice, which can be described as quasi particles (phonons). The starting point is the definition of the phonon mean free path

$$\Lambda = \nu_g \tau, \tag{27}$$

with $\nu_g$ as the group velocity of the phonons and $\tau$ as the relaxation time [25, 28, 29, 38, 39]. The group velocity of the phonons can be divided into several parts, because of the broad spectrum of the phonons. The high energetic optical phonons exhibit low group velocities, which are not effective heat carriers, but interact with acoustic phonons and influence the heat transfer [34, 36, 39]. This acoustic phonons are the main heat carriers and so the group velocity is high. The mean free path is also influenced by the relaxation time. With a short relaxation time the mean free path is reduced, this is done by several scattering mechanism like point defect scattering, boundary scattering or Umklapp scattering. By reducing the boundary size the mean free path is reduced, which can be applied by nano structures, a complex crystal structure or an amorphous structure [25, 33, 36, 38, 40]. Combined with the kinetic gas theory $\kappa_l$ is

$$\kappa_l = \frac{1}{3} C_V \nu_g \Lambda, \tag{28}$$

with $C_V$ as the heat capacity. A low heat capacity leads (according to equation 28) to a low lattice thermal conductivity. The heat capacity can be reduced by heavy atoms, large unit cell volumes or low bonding strength. With increasing unit cell volume the atom number increases, leading to a higher number of optical phonon branches. At temperatures of $\theta_D \ll$ T almost all optical states are occupied (Dulong-Petit law), this leads to a lower contribution of the acoustic phonons to the heat capacity.

$$C_V = 9 N k_B \left(\frac{T}{\theta_D}\right)^3 \int_0^{\frac{\theta_D}{T}} \frac{z^4 e^z}{(e^z - 1)^2} dz, \tag{29}$$

with the Debye temperature

$$\theta_D = \frac{\hbar \omega_D}{k_B} = \frac{\hbar \nu_D}{k_B} \sqrt[3]{\frac{6\pi^2 N}{V}}, \tag{30}$$

and $N$ as the number of atoms in the unit cell, $V$ the volume of the unit cell and $\nu_D$ as the Debye velocity. In Keyes‘ expression all intrinsic properties, which determine the lattice conductivity, are combined:

$$\kappa_l \cdot T = \frac{(RT_m)^{\frac{3}{2}} \rho^{\frac{2}{3}}}{3\gamma^2 \epsilon_A^3 N_A^{\frac{1}{3}} M^{\frac{7}{6}}}, \tag{31}$$

with $R$ as the ideal gas constant, $T_m$ the melting point of the material, $\rho$ the density, $\gamma$ the Grüneisen constant, $\epsilon_A$ the fractional amplitude of interatomic thermal vibration, $N_A$ the Avogadro‘s number and $M$ as the mean atomic weight.[30, 41]

### D. Thermoelectric modules

In Figure 3 a schematic thermoelectric module is shown.[27] The p-type material legs (green) are connected in series with the n-type material legs (red). From the hot side (top) the carrier, holes in the p-type material and electrons in the n-type material, diffuse to the cold side (see zoom in). This diffusion establishes a positive charge at the cold side of the p-type material and at the hot side of the n-type material. A negative charge is measured at the hot side of the p-type material and at the cold side of the n-type material. This enables a current flow from the cold side of the n-type material through the leg pair.

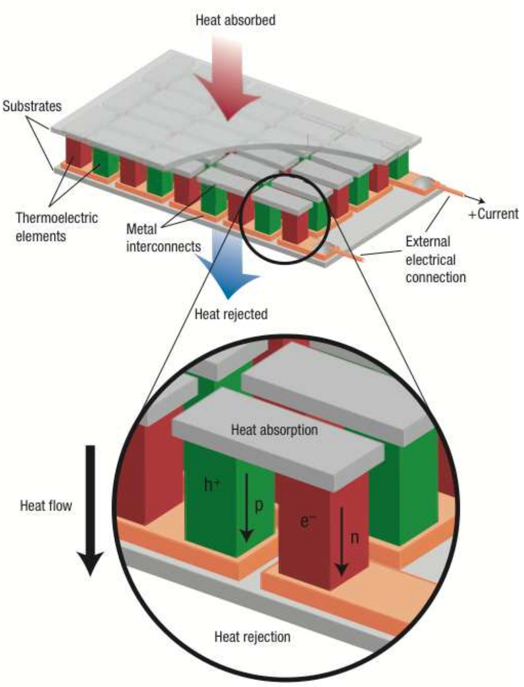

FIG. 3: Schematic thermoelectric module. Shown are the connected n-type and p-type thermoelectric legs [27].

### E. Heusler compounds

#### 1. *Heusler compounds with $L2_1$ structure*

The structure prototype of Heusler compounds with $L2_1$ structure is $Cu_2MnAl$ (225, $Fm\overline{3}m$)[1, 2, 42–49], the first known compound with this structure. The common composition is $X_2YZ$, with X, Y as transition metals and Z as main group elements. The X atoms occupy the 8c Wyckoff positions, the Y atoms the 4a positions and the Z atoms the 4b positions. The structure is build up by the Z atoms, which form a face centered cubic lattice. The Y atoms occupy the octahedral cavities at the middle of the edging of the fcc lattice and in the center of this lattice. The X atoms fill up all tetrahedral cavities, and are in each case surrounded by four Y and four Z atoms.

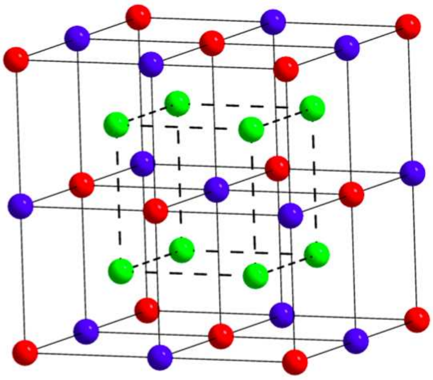

FIG. 4: The Heusler L2$_1$ structure $X_2YZ$.

### 2. *Heusler compounds with C1$_b$ structure*

The prototype for Heusler compounds with C1$_b$ structure is MgAgAs (216, $F\overline{4}3m$) with the common composition $XYZ$. This structure is related to the L2$_1$ structure, but just 50% of the tetrahedral cavities are occupied. The Z atoms occupy the Wyckoff 4d positions, the Y atoms the 4c and the X atoms the 4a positions. The structure can also be seen as zinc blende structure with filled octahedral cavities. Jung *et al* [50] recognized that many XYZ compounds can be thought of as comprising $X^{n+}$ ions stuffed in a zinc-blende-type [YZ]$^{n-}$ sublattice, where the number of valence electrons associated with the [YZ]$^{n-}$ sublattice is 18 ($d^{10}$+$s^2$+$p^6$). Such closed-shell 18-electron compounds are nonmagnetic and semiconducting [51, 52].

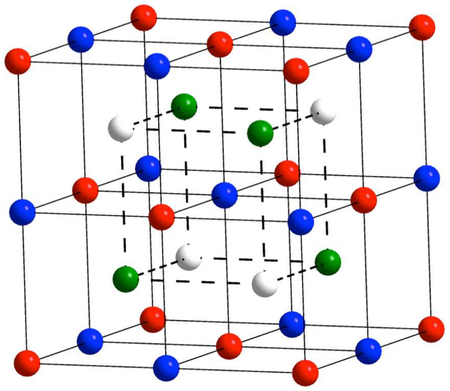

FIG. 5: The Heusler C$1_b$ structure XYZ.

### F. Phase separation

First of all, the difference between decomposition, segregation and separation has to be defined. Phase separation means that more than one phase is present in a sample. Usually, in almost all samples small impurities exist, which are second phases, but are not considered as a phase separation. Samples with a phase separation exhibit at least one additional phase, which occupies 10% of the volume of the sample. This means that a phase decomposition and a phase segregation is a phase separation. The difference between a decomposition and a segregation is that in a decomposition the new phase, which is created out of the parent phase, exhibits the same crystal structure. In a segregation the new phase has a different crystal structure.[53, 54] A phase separation is also defined by the lattice misfit. In Figure 6 the three different possible precipitates are shown, which form three different interfaces. In a) the coherent precipitate with almost no lattice misfit is recognizable. This case is found in decompositions, in which the crystal structures of the phases are the same. In b) the case of a slight misfit in the crystal structure due to, e.g. different lattice parameters is demonstrated. The last case (c) is the incoherent precipitate, which exhibits a completely different crystal structure. This incoherent precipitates are often found in segregations.[53–56]

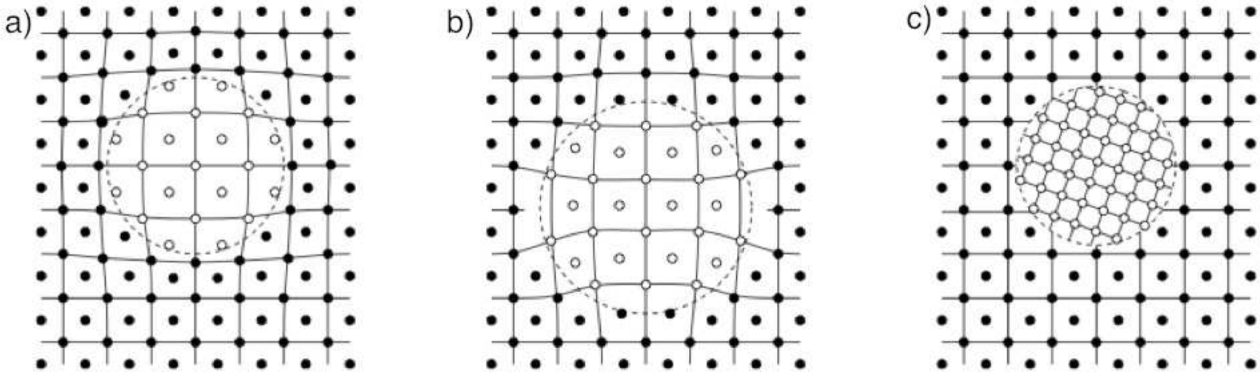

FIG. 6: Schematic lattice misfits with different precipitates. Shown is a coherent precipitate with almost no misfit (a); a semicoherent precipitate with a slight misfit (b); a incoherent precipitate with a completely different crystal structure (c).[54]

As indicated in Fig. 6 the misfit influences the shape of the precipitate or segregation or decomposition. Mainly two energies determine the shape of the precipitate, the surface energy of the precipitate and the misfit strain energy.[57] In Table I the circumstances for three forms of a decomposition are listed. Form I is the case of a coherent precipitate, which leads to a spherical precipitate. Form II is the common case of a semicoherent precipitate, which exhibits a huge misfit in the lattice parameter and forms a disk-like or needle-like precipitate. Form III is the special case of a normal eutectic growth, which is diffusion determined due to a planar solidification front moving in one direction. Behind this front the two phases grow in a lamellar shape. In Fig. 7 the dependence of the c/a ratio is shown, demonstrating the influence of the lattice parameter misfit.

| Form I | Form II | Form III |
|---|---|---|
| same crystal structure and | large misfit | eutectic decomposition |
| similar lattice parameter | in the lattice parameter | (a→ b + c) |
| ⇓ | ⇓ | ⇓ |
| misfit strain energy | huge surface energy | diffusion |
| negligible | with low misfit strain energy | determined |
| ⇓ | ⇓ | ⇓ |
| sphere -like precipitates | disk-like or needle-like precipitates | lamellar growth |
|  |  | ⇓ |
|  |  | conversion at |
|  |  | the grain boundaries |
|  |  | (high diffusion) |

TABLE I: Three forms of the precipitates in a decomposed sample.

Two different decomposition processes can be described. In Figure 8 the two growth process are shown. The composition in dependence on the growth time and the distance in the sample is demonstrated. In a) the spinodal decomposition is described. This decomposition begins spontaneously and the steady state composition is established by up-hill diffusion after a time $t_\infty$. In b) the nucleation and growth process is shown. In this process the steady state composition is directly build up (seed) due to thermal fluctuations. After the seed is created it grows by down-hill diffusion. So the main difference between the two processes is that if a spinodal decomposition is quenched, phases with different compositions are recognizable. In the nucleation and growth process just one composition,

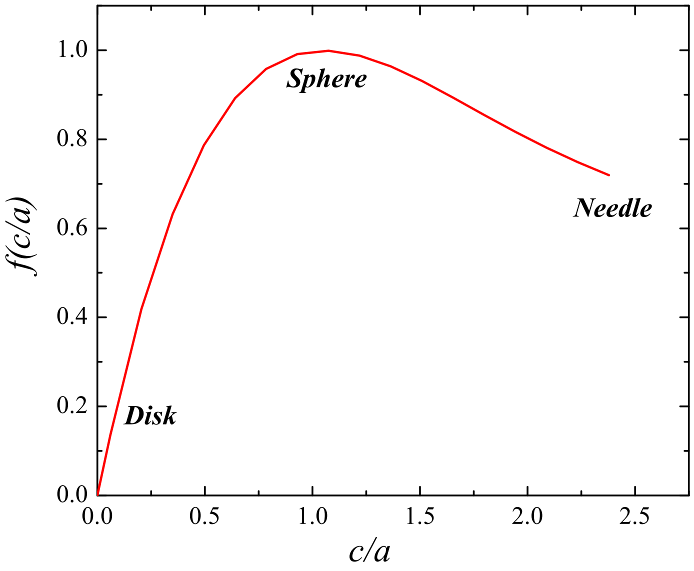

FIG. 7: The shape effects in dependence of the c/a ratio. Indicated are the shapes of the precipitates at the c/a ratio. After F.R.N. Nabarro.[57]

the steady state composition, can be found [53, 54].

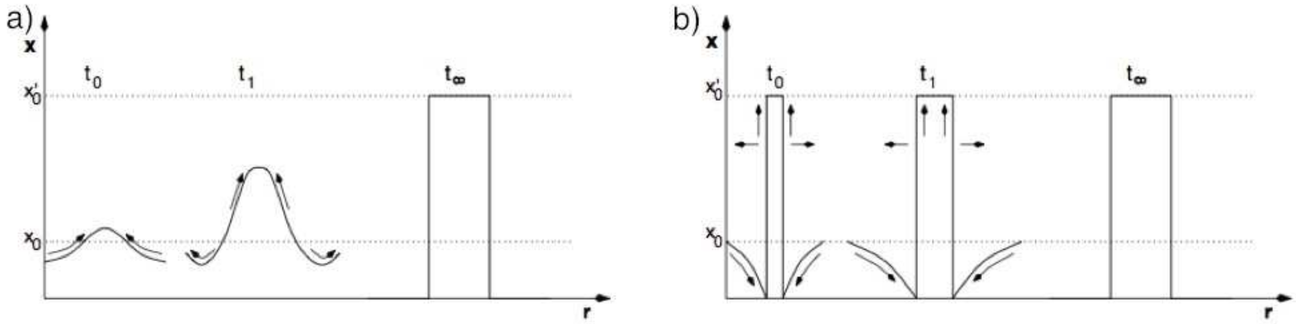

FIG. 8: Schematic growth processes of a decomposition. Shown is the composition in dependence on the growth time and distance in the sample. In a) the spinodal decomposition process is demonstrated. b) describes the nucleation and growth process.[54]

# III. METHODS

## A. Synthesis

### 1. *Conventional preparation method*

Three different preparation methods were investigated for the synthesis of the Heusler compounds. The conventional preparation method (see Fig. 9) is the simplest method. The constituting elements were stoichiometric weighed, then arc melted three times with a home-made system (see Figure 10). After this the samples were crushed and remelted, to insure the homogeneity of the sample. An additional heat treatment was necessary for all Heusler compounds with $C1_b$ structure for 7 days at 950°C under argon.

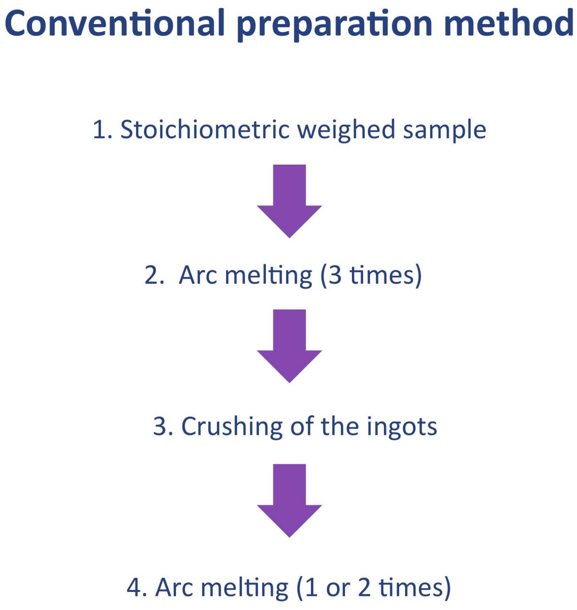

FIG. 9: Sample preparation via the conventional method.

### 2. *Conventional cold-pressing sintering method (CCS)*

In the conventional cold-pressing sintering method the samples were first arc melted analogous to the conventional method (see Fig. 9) and then powdered by ball milling. The Fritsch *Planeten-Mikromühle PULVERISETTE 7 premium line* was used. The obtained

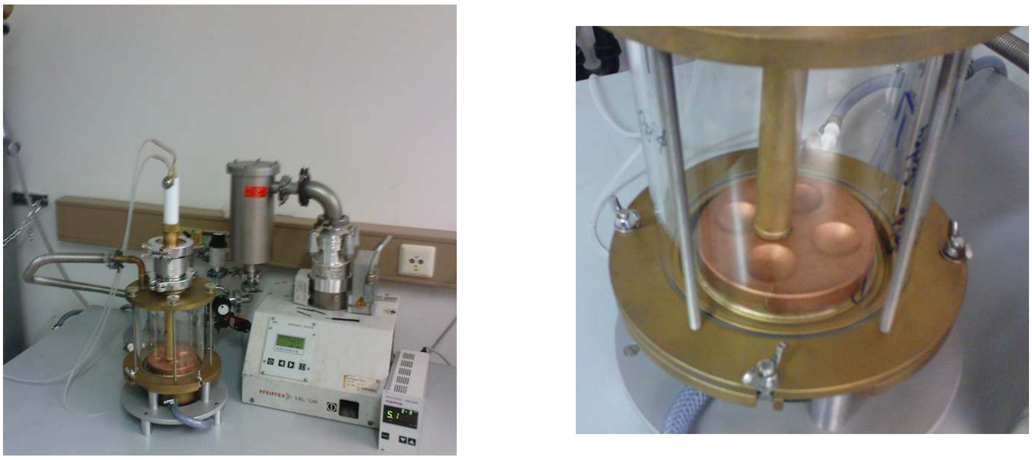

FIG. 10: The arc melter setup.

powder was cold pressed and sintered again by arc melting. This improved the homogeneity significantly. The additional heat treatment for 7 days at 950°C under argon was necessary for an improved lattice structure. This method was used for every samples without volatile elements synthesized in this work.

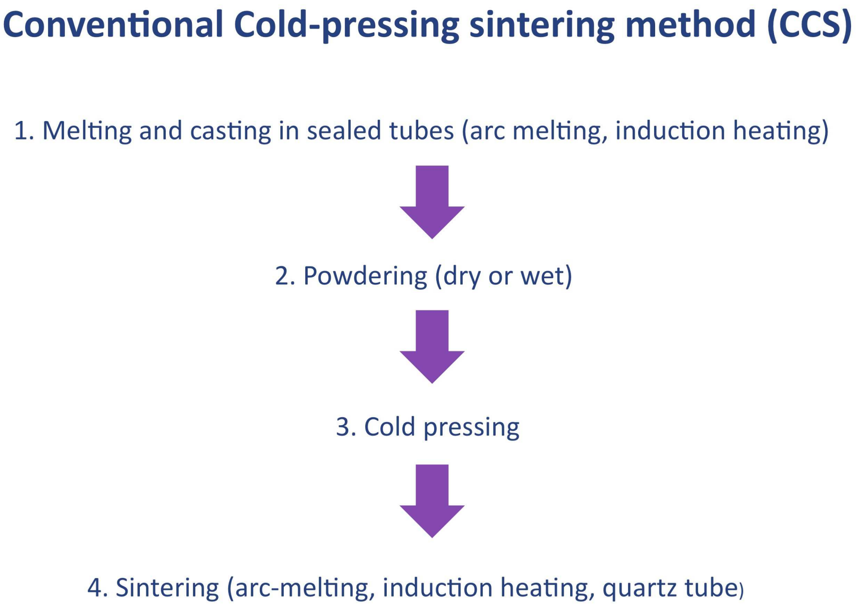

FIG. 11: Sample preparation via the conventional cold-pressed sintering method.

### *3. Pulverized powder and intermixed elements sintering method (PIES)*

In the pulverized and intermixed elements sintering method all elements or pre-melted alloys were pulverized and intermixed. Afterwards the mixture was mechanical alloyed by a ball mill. The obtained powder, which already exhibits the Heusler structure, was cold pressed and sintered again [24]. A heat treatment for 7 days at 950°C under argon was necessary. All samples in this work with volatile elements were synthesized with this method.

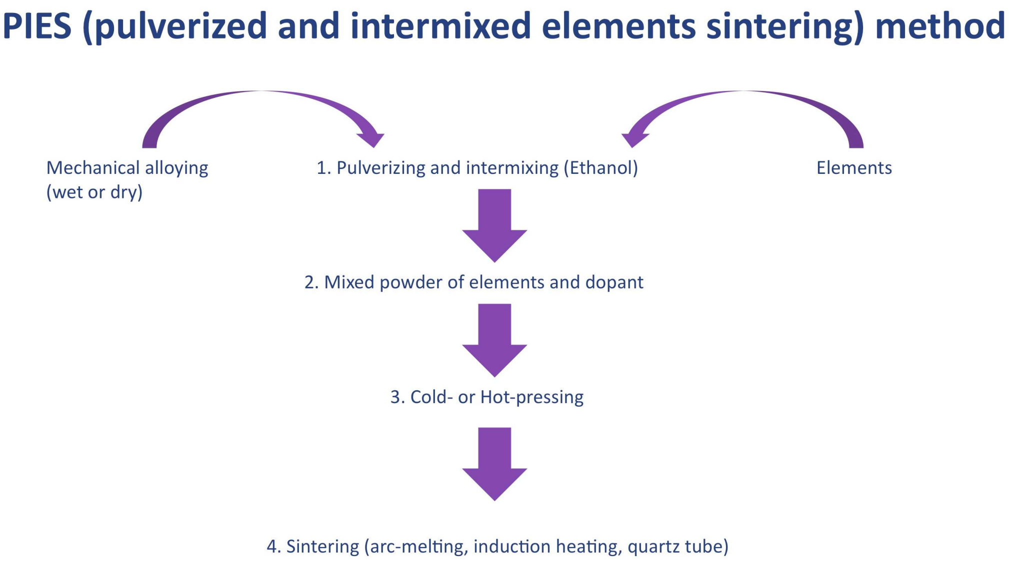

FIG. 12: Sample preparation via the pulverized and intermixed elements sintering method.

### B. Characterization

#### 1. *Powder X-ray diffraction*

The lattice structure was determined by powder X-ray diffraction. In Fig. 13 the schematic Bragg diffraction is shown. An incident beam hits the surface of a sample and the resulting reflections show a interference pattern. This is described by the Bragg equation (see equation 32).

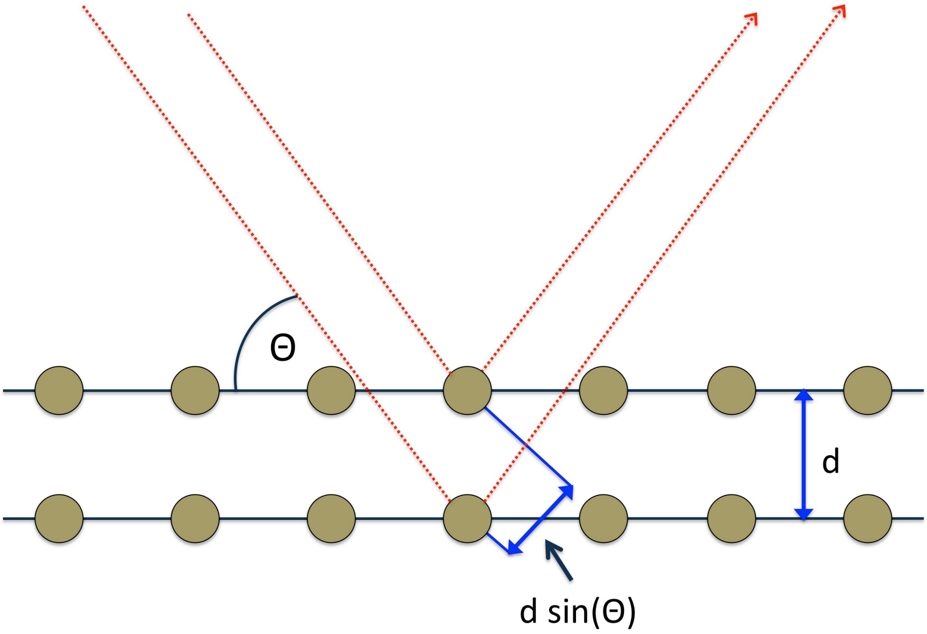

FIG. 13: Schematic Bragg diffraction. Shown are two atomic layer, which are separated by one Miller plane distance and an incident beam with the an incidence angle of $\theta$.

$$2dsin(\theta) = n\lambda \tag{32}$$

with $d$ as the Miller plane distance and $\lambda$ as the wavelength of the incident beam. The Miller indices describe the origin of the obtained reflections of a certain lattice structure. These reflections are the fingerprints of the lattice structure, see for example Fig. 14. The samples in this work were characterized by the Siemens D5000 using Cu $K_\alpha$ radiation.

$$d = \frac{a}{\sqrt{h^2 + k^2 + l^2}} \tag{33}$$

with $a$ as lattice parameter of a cubic crystal, $h$, $k$, $l$ as the Miller indices of the Bragg plane [33].

$$h^2 + k^2 + l^2 = sin^2(\theta) \cdot \left(\frac{2a}{\lambda}\right)^2 \tag{34}$$

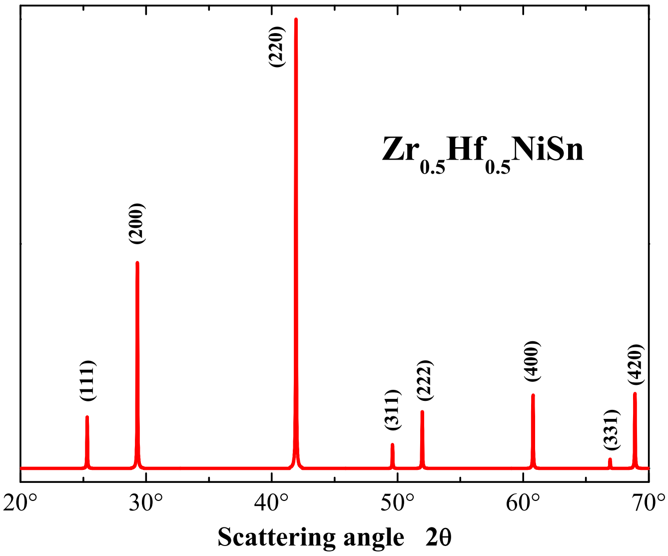

FIG. 14: Powder X-ray diffraction pattern of the Heusler compound $Zr_{0.5}Hf_{0.5}NiSn$ measured with Cu $K_\alpha$ radiation. In brackets are the Miller indices indicated.

### 2. *Scanning electron microscope with energy dispersive X-ray spectroscopy*

A scanning electron microscope (SEM, Jeol JSM-6400) equipped with an energy dispersive X-ray spectroscopy (EDX) detection system (EUMEX EDX) was used to identify the micro stucture and local stoichiometry of the phase separated compound. The measurements were carried out at a pressure of 3 x $10^{-6}$ mbar. An acceleration voltage of 20 kV was applied and an inspection angle of 35° was set up. For the correction of the quantitative data the ZAF method was used which relies on atomic number (Z), absorption (A) and fluorescence (F) effects. The images were acquired via the Digital Image Processing System (DIPS) and the quantitative chemical analysis was performed with the program WINEDS 4.0. Figure 15 shows the signals of the backscattering image, produced by backscattered electrons, and of the energy dispersive X-ray spectroscopy, which is element characteristic X-ray radiation.

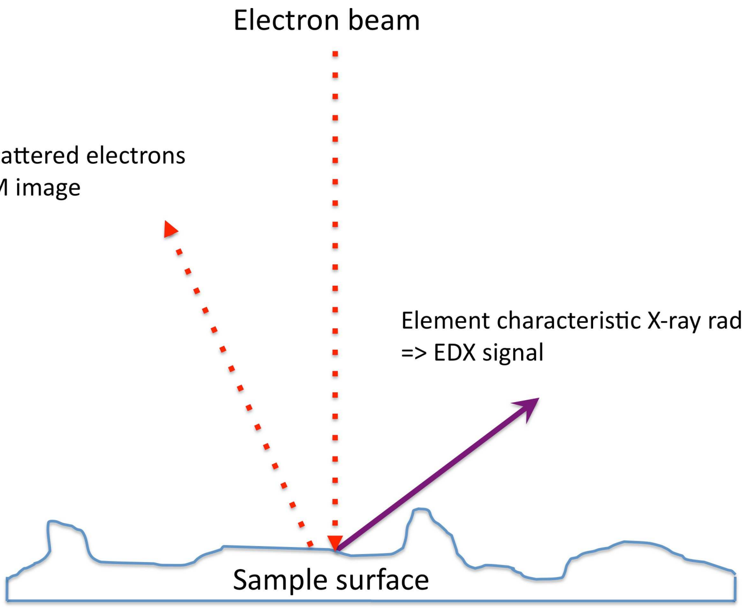

FIG. 15: Schematic view of the signals produced and used in a SEM. Shown is an incident electron beam on an arbitrary sample surface and the resulting signal measured by a SEM and EDX detector.

*3. Physical property measurement system (PPMS)*

The low temperature transport properties were investigated by the physical property measurement system (*PPMS, Quantum Design*). For transport measurements the samples were cut into bars with the approximate dimensions of 2 x 2 x 10 mm$^3$. The samples were polished immediately before contacting in order to remove oxide layers.

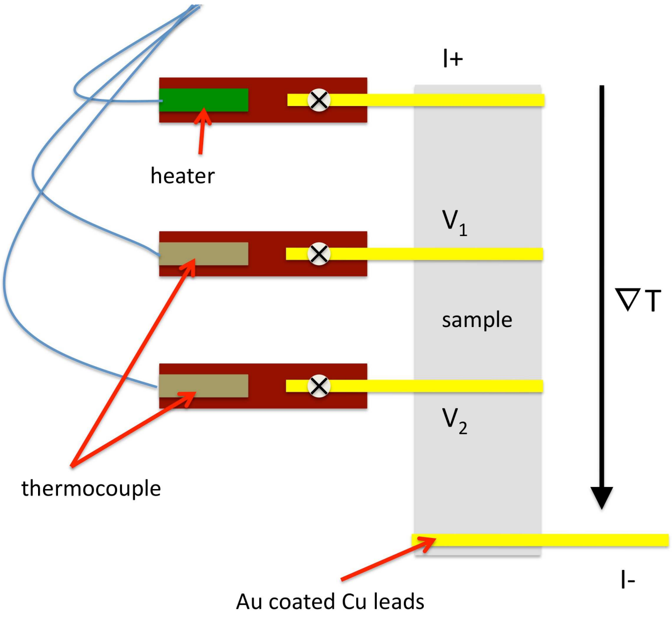

FIG. 16: Schematic contacting of a sample in the thermal transport mode of the PPMS.

The samples were contacted with four gold-coated copper leads that were wrapped around the bars to homogenize the current passing through. The sample chamber was flooded with helium and evacuated afterwards. The transport measurements were carried out at a pressure of 1.2 x $10^{-4}$ mbar by a standard four point ac method from 2-300 K. The schematic contacting of a sample is shown in Figure 16. At the top contact ($I$+) the current for the electrical resistivity measurement is applied. The bottom contact is the back contact ($I$-). Between the two contacts in the middle the voltage is measured. The resistivity is determined by

$$\rho = R\frac{A}{l} = \frac{U}{I}\frac{A}{l}, \tag{35}$$

with $R$ as the resistance, $A$ the cross-section area, $l$ the lead-separation, $U$ the voltage between $V_2$ - $V_1$ and $I$ the applied current. To determine the Seebeck coefficient the heater (green) at the top contact is switched on. A temperature gradient $\nabla T$ in the sample is established and the temperature difference ($T_2$-$T_1$) at the two contacts in the middle are measured by the two thermocouples (gold). Parallel the voltage is measured and with equation 1 the Seebeck coefficient is determined. The thermal conductivity is obtained by switching on the heater together with a stop watch, which counts the time till the same temperature change is visible at both thermocouples. Under the approximation that the heat is just carried through the sample (no irradiation losses), the thermal conductivity can be determined.

The high temperature Seebeck coefficient and electrical resistivity measurements were done by the . In comparison to the *PPMS* the contacting for the *LSR-3* is forced-fitted (see Figure 17) for the top and bottom contacted and the contacts in the middle are spring-loaded contacts. The electrical resistivity and Seebeck coefficient are determined analogous to the low temperature determination. The samples were measured from 50 to 600°C to avoid reaction with the platinum contacts.

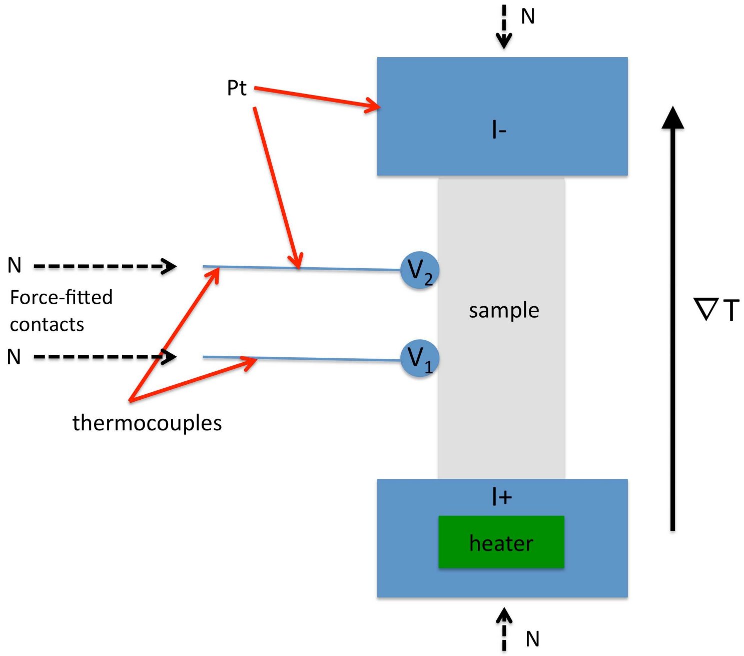

FIG. 17: Schematic contacting of a sample in the Linseis LSR-3.

The high temperature thermal conductivity determination is not so simple as in the low temperature range. The thermal conductivity has to measured via

$$\kappa = \alpha_d \cdot c_P \cdot \rho_D, \tag{36}$$

with $\alpha_d$ as the thermal diffusivity, $c_P$ the specific heat capacity and $\rho_D$ the density of the sample.[24, 28]

### Diffusivity $\alpha_d$ determination

The diffusivity was determined by the *Netzsch LFA 457*. For this the samples were cut into disks and coated with graphite (to insure that no reflections appear). In Figure 18 the schematic measurement setup is shown. A infrared laser pulse was applied on the bottom side of the sample. Together with the laser pulse a stop watch was started and counts until a signal is registered at the InSb detector above the sample. From the shape and the time interval the thermal diffusivity was determined.

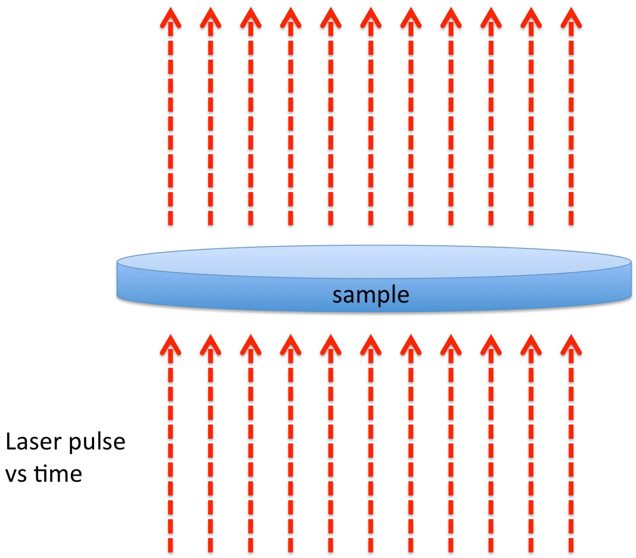

FIG. 18: Schematic measurement setup of the LFA.

### Heat capacity $cp$ determination

The difference scanning calorimetry measurements were done with a *Netzsch DSC 404 F3*, which uses the integration of the $\Delta T$-$T_R$ plot to determine the enthalpy changes $\phi$ (heat flux). A sample and a reference material was placed in a crucible ($Al_2O_3$ inlay in a Pt crucible) and set on the DSC probe head, which consists of a thermally well conducting material (Pt). When the furnace heats the sample and the reference material, the heat flows from the sample and reference material into the DSC probe head, where the thermocouples of the reference material and the sample are placed. When the heat flux $\phi$ for both is the same, no voltage V is detected, because the voltage is proportional to $\Delta T$, which is proportional to $\phi_S$-$\phi_R$. When the enthalpy of the sample changes during the measurement due to phase transition e.g., the heat flux $\phi$ is changes and a voltage is measured. When the heat capacity of the reference material is know the heat capacity of the sample can be calculated by comparison with these values.

$$c_p = \frac{\delta H}{\delta T} \tag{37}$$

with $H$ as the enthalpy and $T$ the temperature.

### Density $\rho_D$ determination

The density of the samples $\rho_S$ were determined by a pycnometer, which allows to determine the density via equation 38.

$$\rho_S = \frac{m_{sp} - m_p}{(m_{wp} - m_p) - (m_{spw} - m_{sp})} \cdot \rho_w \tag{38}$$

with $\rho_w$ as the density of the water, $m_{sp}$ as the mass of the pycnometer and the sample, $m_p$ as the mass of the empty pycnometer, $m_{wp}$ as the mass of the pycnometer filled with water and $m_{spw}$ the mass of the pycnometer, the sample and water.

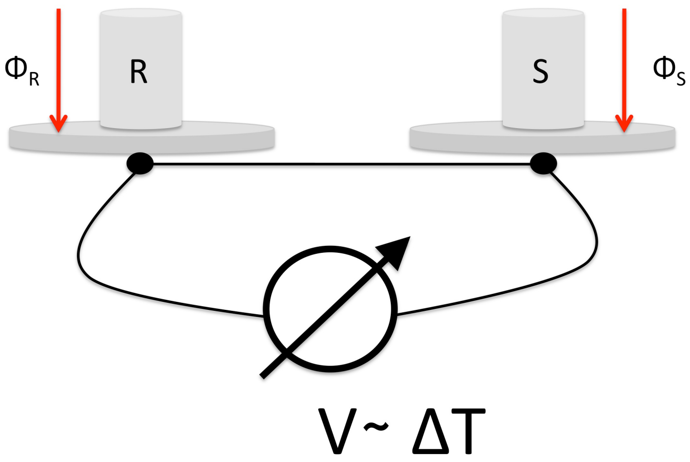

FIG. 19: Schematic measurement setup of the DSC. Shown are the sample and reference crucible connected with to thermocouples, which produce a voltage if $\phi_S$ is not equal to $\phi_R$.

## 6. *Superconducting quantum interference device (SQUID)*

With the superconducting quantum interference device (*SQUID*) the magnetic properties of the Heusler samples with $L2_1$ structure were determined. The magnetometer *MPMS* (*Quantum Design*) in the temperature region of 2 K -800 K was used with magnetic fields up to 5 T. The setup is based on the sensitivity of the SQUID sensor, which consists of a superconducting coil disconnected by two Josephson contacts, on a change in the magnetic flux. A Josephson contact is a tunnel barrier, which is passable under certain conditions for the cooper-pair. Both of the Josephson contacts are placed in the SQUID so that a highly coherent supra current is distributed on the contacts. After the passing of the tunnel barrier both currents are combined and a closed current circuit, which exhibits a phase difference, is obtained. The phase shift can be applied by an external magnetic field, which is set into the superconducting coil. The established interference can be used to measure small magnetic fields. During the measurement the sample is pulled through the superconducting coil, what induces an electrical current in the detection coil (SQUID coil). This induction current is connected to the supra current, what causes a change in the supra current proportional to the magnetic field. This leads to a variation of the input voltage. If the change is calibrated, very accurate measurements are possible.

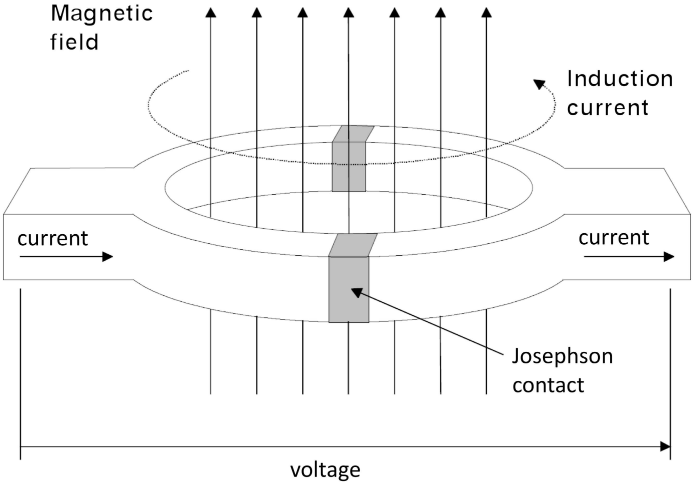

FIG. 20: Schematic principle of the SQUID.

The electronic structure of the several Heusler compounds with $C1_b$ structure were explored by means of high energy X-ray photo electron spectroscopy. The measurements were performed at the beamline BL47XU of the synchrotron *SPring 8* (Hyogo, Japan). The photons are produced by means of a 140-pole in vacuum undulator and are further monochromized by a double-crystal monochromator. The first monochromator uses Si(111) crystals and the second a Si(111) channel-cut crystal with (444) reflections (for 8 keV X-rays). The energy of the photo electrons is analyzed using a Gammadata - Scienta R 4000-12kV electron spectrometer. For the reported experiments in this work, a photon energy of 7939.9 eV has been employed. Under the present experimental conditions an overall resolution of 250 meV has been reached. All values concerning the resolution are determined from the Fermi-edge of a gold sample. Due to the low cross-section of the valence states from the investigated compounds, the spectra had to be taken with $E_{pass} = 100$ eV and a 500 $\mu$m slit in order to achieve a good signal to noise ratio. The polycrystalline samples have been cleaved in-situ before taking the spectra to remove the native oxide layer. Core-level spectra have been taken to check the cleanliness of the samples. No traces of impurities were found. All measurements have been made at a sample temperature of 300 K.

The errors in the determination differ over the different characterization methods. The errors in the powder X-ray diffraction are caused by bad sample preparation or installation in the measurement device, meaning that the sample is not in the right distance between the X-ray source and the detector. This leads to an offset error in the diffraction pattern. Additional errors can be produced due to fluorescence of elements of the sample, by huge backgrounds due to bad sample preparations or by too short measurement times and errors during the refinements. However, the crystal structure of the Heusler compounds should be visible. The estimated error of the lattice parameter counts at least 0.005 Å. The errors of the energy dispersive X-ray spectroscopy are mainly due to the detector and the sample preparation. For all results it has to be kept in mind that the penetration depth of electrons with 20 keV for the investigated Heusler compounds is approximately 1 $\mu$m, meaning that the composition of the illuminated volume (area of the electron spot multiplied by penetration depth) is determined. This means that possibly more than one phase is measured. The second error is caused by overlapping signals and the fitting of the signals. Overall the estimated error for the determined composition is at least 5% per element. The errors in the electrical resistivity and Seebeck coefficient determination for low and high temperatures are dominated by the kind of the sample contacting. The *PPMS* uses firmly bonded contacts and the *LSR-3* uses force-fitted contacts. This leads to a mismatch in the measured resistivity values. Usually, the force-fitted contacts lead to lower resistivity values, because of the better contacts. However, this error shifts the resistivity curve just slightly. The estimated error of a resistivity measurement is 5%. The determination of the Seebeck coefficient is not as much sensitive to the contacts. The reproducibility of the Seebeck coefficient measurements are mainly influenced by the appliance of a temperature gradient. The error of the Seebeck coefficient measurements is estimated as 10% of the measured value. The measured thermal conductivity at the *PPMS* is dependent on the contacts, the appliance of the temperature gradient and the thermocouples, leading to at least an error of 1 $\frac{W}{Km}$. For the high temperature thermal conductivity determination three parameters have to be determined (see equation 36). The errors of the diffusivity determination with the *LFA 457* are dominated by the sample shape and the applied calculation model. The error is estimated to 3% of the measured value. The heat capacity contributes the main part to the error of the thermal conductivity. The heat capacity measured with the *DSC* is dependent on the temperature program, the sample preparation and the contact resistance between the crucible and the sample holder as well as the contact resistance between the sample and the crucible. Due to the differential methods, with sapphire as standard sample, the accuracy is not very high. The estimated error counts at least 10% of the measured values. The last parameter for the thermal conductivity determination is the density, which was measured by a *pycnometer*. The measurement is dependent on the accuracy of the used balance and the temperature of the used water as well as on the volume of the sample. By using different pieces of one sample and repeating the measurements the error is just in the range of 3% of the measured value. Combined, the estimated error of the determined Figure of Merit is at least 20% of the measured value.

## IV. RESULTS

### A. Influence of element substitutions on $Zr_{0.5}Hf_{0.5}NiSn$

To investigate the influence of different elemental substitutions on a known thermoelectricly used Heusler compound with $C1_b$ structure, the known Heusler compound $Zr_{0.5}Hf_{0.5}NiSn$ [19, 20] was chosen and substituted with several elements. The $Zr_{0.5}Hf_{0.5}NiSn$ compound exhibits promising thermoelectric properties (see Figure 21). The thermal conductivity is low in comparison to other Heusler compounds, the value of the Seebeck coefficient lies in an adequate range, only the electrical resistivity is too high to lead to a high value of the Figure of Merit. Altogether this is a good compound for making a starting point of investigations on the influence of element substitutions and with it for an optimization of the thermoelectric properties. The element substitutions were chosen with respect to the GADSL (Global Automotive Declarable Substance List), which means avoiding toxic elements, and paying attention to the prices of the elements.

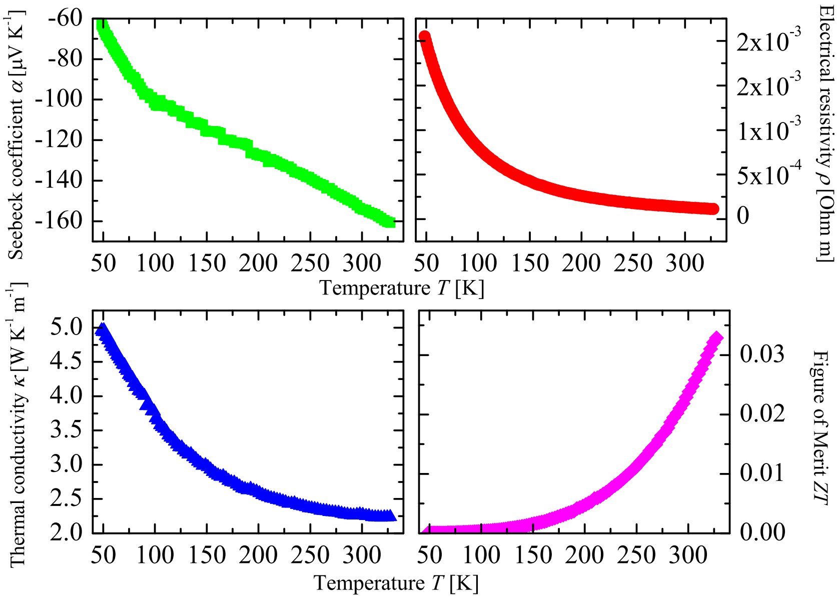

FIG. 21: Thermoelectric properties of $Zr_{0.5}Hf_{0.5}NiSn$. Shown are the temperature dependence of the Seebeck coefficient $\alpha$, the thermal conductivity $\kappa$, the electrical resistivity $\rho$ and the dimensionless Figure of Merit ZT from 50 K to 350 K.

### *1. Vanadium substitution*

First of all, the Zr/Hf atoms were substituted with vanadium, which formally exhibits one valence electron more than zirconium and hafnium and should increase the carrier concentration.

All samples from this series exhibit the $C1_b$ structure. In Figure 22, the measured electronic properties of the $(\mathrm{Zr}_{0.5}\mathrm{Hf}_{0.5})_{1-x}\mathrm{V}_x\mathrm{NiSn}$ samples are compared with the parent compound $\mathrm{Zr}_{0.5}\mathrm{Hf}_{0.5}\mathrm{NiSn}$. The values of the Seebeck coefficient exhibit a dependence on the vanadium concentration. With the help of Figure 26 it is easy to understand this dependence, which seems to be dominated by possible resonant levels build up by the added vanadium.[5, 31, 38, 58–62] At low vanadium concentrations (1% and 2%) the values of the Seebeck coefficient increase due to the increase of the localized resonant states caused by the distortion of the vanadium atoms in the lattice. Possibly leading to a higher effective mass $m^*$ which increases the values of the Seebeck coefficient. An indication for this can be seen in Figure 23, which shows the dependence of the Seebeck coefficient on the electrical conductivity. For a non-degenerated semiconductor, which is just dependent on the carrier concentration (constant mobility), the development should approximately follow the $(\sigma)^{-\frac{3}{2}}$ behavior (see Figure 2). This behavior can not be found in all samples, which indicates that the mobility changes. The change in the mobility is caused either by a change of the scattering time or by a change of the carrier effective mass. The additional increase of the carrier concentration, which is achieved by substituting Zr/Hf with vanadium, does not have a high impact on the Seebeck coefficient at low concentrations of V. The resistivity values are decreased due to the fact that the carrier concentration is increased. From 3% to 5% V substitution the localized states near the conduction band (CB) are broadened and thereby the gap between the localized states and the CB is decreased. Due to the small gap between the localized states and the CB and due to the increasing number of electrons the resistivity is decreased as well as the values of the Seebeck coefficient. In comparison to the parent sample the resistivity values of all substituted samples are decreased to almost one order of magnitude, but the values of the Seebeck coefficient are increased or in almost the same order of magnitude. This is a real improvement of the electronic properties of the parent sample.

In Figure 24 the thermal conductivity of the $(\mathrm{Zr}_{0.5}\mathrm{Hf}_{0.5})_{1-x}\mathrm{V}_x\mathrm{NiSn}$ samples is compared

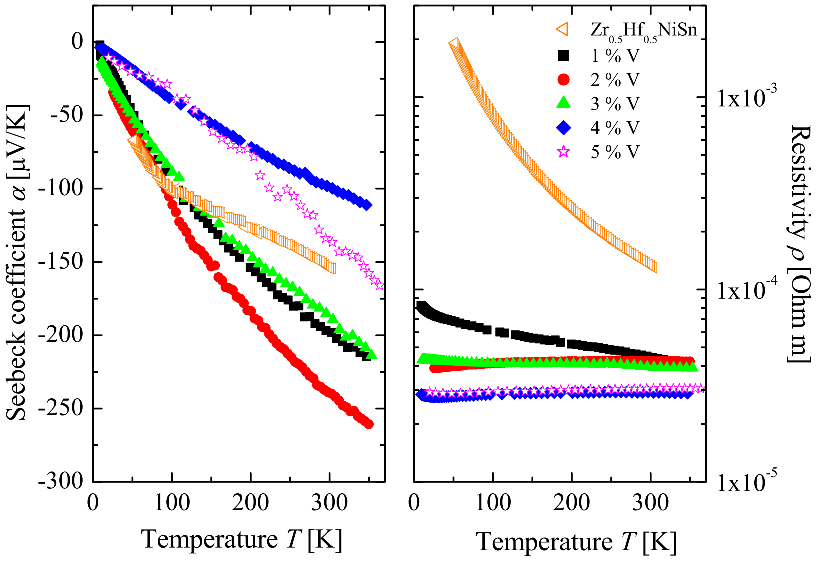

FIG. 22: Temperature dependence of the Seebeck coefficient and resistivity of $(Zr_{0.5}Hf_{0.5})_{(1-x)}Z_xNiSn$ | $Z$: V ; x: 0.01-0.05 samples.

with the parent sample. All vanadium substituted samples exhibit a higher thermal conductivity in comparison to the parent compound, except the 5% V substituted sample, which exhibits as mentioned above a high distortion in the structure. It has to be kept in mind that all the vanadium substituted samples have lower values of the resistivity, meaning that the electronic contribution to the thermal conductivity is higher and this way is not unexpected that the values of the thermal conductivity of the V samples are higher (see Figure 25). The calculated electronic contribution to the thermal conductivity $\kappa_e$ is shown in Figure 25 and is compared to the lattice thermal conductivity $\kappa_l$. The V samples show a dependence of the lattice thermal conductivity on the vanadium concentration except the 4% V, which can be explained by the increased disorder or defects in the samples due to the increasing substitution. The 4% vanadium substituted sample seems to exhibit a higher crystallinity recognizable in the maximum at $\approx$ 50 K, which is due to compensation of the increasing number of phonons contributing to the transport and due to the increasing contribution from Umklapp processes causing scattering with increasing temperature. The additional scattering at grain boundaries causes a decrease of $\kappa_l$. The higher crystallinity causes the higher thermal conductivity, because the phonon scattering is decreased by the decreased

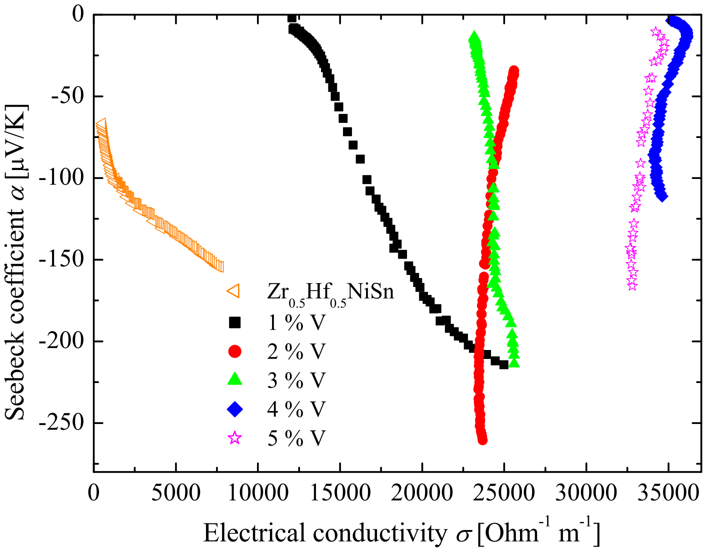

FIG. 23: Electrical conductivity dependence of the Seebeck coefficient of $(\mathrm{Zr}_{0.5}\mathrm{Hf}_{0.5})_{(1-x)}Z_x\mathrm{NiSn}$ | $Z$: V ; x: 0.01-0.05 samples.

distortion of the lattice. The samples with higher V concentrations (3%, 4%, 5%) show the typical behavior of a compound with a complex unit cell in quasicrystal or amorphous metals[63, 64]. The parent sample and the samples with low vanadium concentrations show a maximum at intermediate temperatures like the 4% V sample due to the higher crystallinity (see Fig.25). Combined all vanadium samples exhibit higher values for the Figure of Merit ZT as the parent sample due to the lower resistivity and the comparable values of the Seebeck coefficient. The maximum Figure of Merit is obtained in the 5% V substituted with ZT= 0.12 at 300 K.

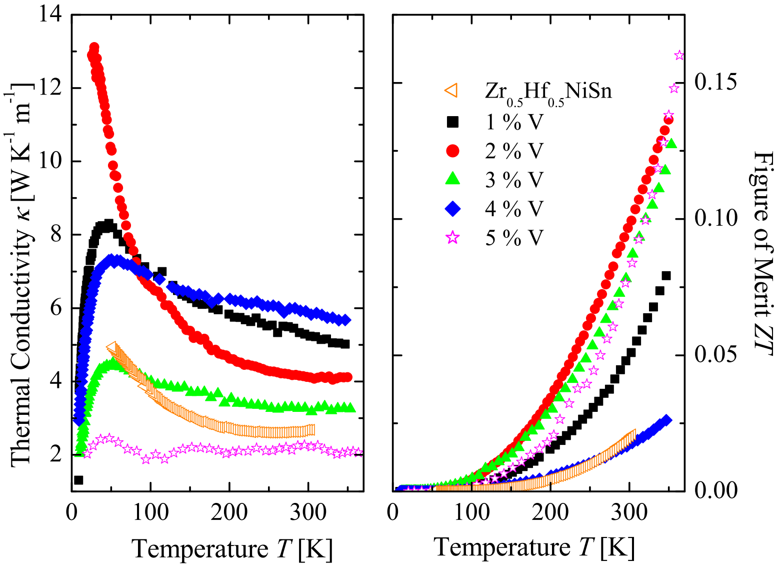

FIG. 24: Temperature dependence of the Figure of Merit and the thermal conductivity of $(\mathrm{Zr}_{0.5}\mathrm{Hf}_{0.5})_{(1-x)}Z_x\mathrm{NiSn}$ | $Z$: V ; x: 0.01-0.05 samples.

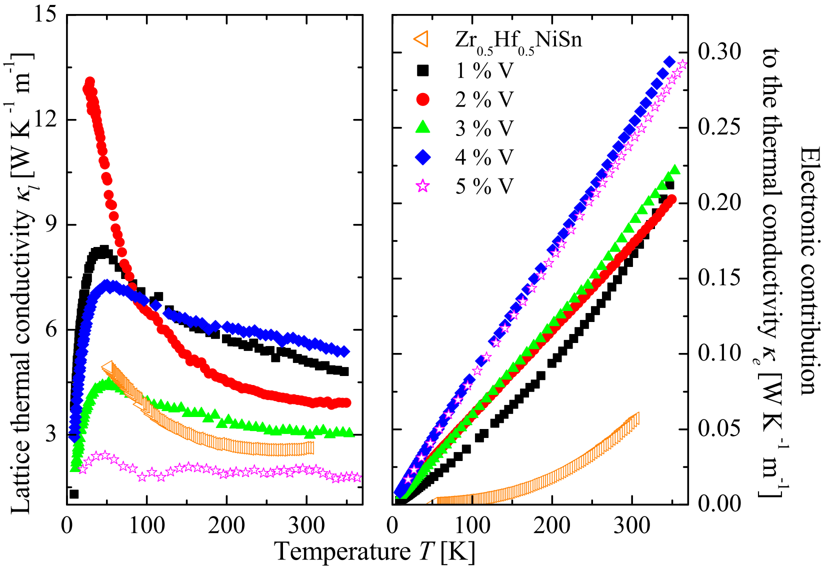

FIG. 25: Temperature dependence of the lattice thermal conductivity and the electronic contribution on the thermal conductivity of $(\mathrm{Zr}_{0.5}\mathrm{Hf}_{0.5})_{(1-x)}Z_x\mathrm{NiSn}$ | $Z$: V ; x: 0.01-0.05 samples.

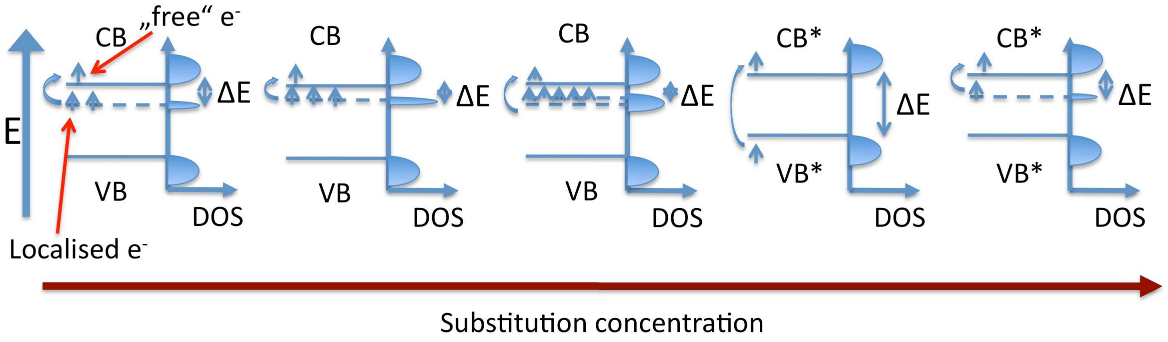

FIG. 26: Possible schematic change in the electronic structure and density of states of the parent Heusler compound in dependence on the substitution concentration at 300 K.

Niobium, which formally owns the same valence electron number in comparison to vanadium, but has a higher effective nuclear charge, should increase the impact of the substitution on the electronic properties and increase the phonon scattering due to mass distortion.
All samples from this series exhibit the $C1_b$ structure.[18] In Figures 27+29, the measured physical properties of the $(\mathrm{Zr}_{0.5}\mathrm{Hf}_{0.5})_{1-x}\mathrm{Nb}_x\mathrm{NiSn}$ samples are compared to the unsubstituted $\mathrm{Zr}_{0.5}\mathrm{Hf}_{0.5}\mathrm{NiSn}$. The thermal conductivity $\kappa$ of the unsubstituted $\mathrm{Zr}_{0.5}\mathrm{Hf}_{0.5}\mathrm{NiSn}$ has the lowest value. This could be partially explained by the low electrical resistivity $\rho$ of the substituted compounds, which is almost two orders of magnitude higher than the unsubstituted compound. An increase of the electrical conductivity $\sigma$ by substituting the $(\mathrm{Zr}_{0.5}\mathrm{Hf}_{0.5})$ with Nb is the expected behavior, because the carrier concentration is increased and simultaneously the electrical conductivity.

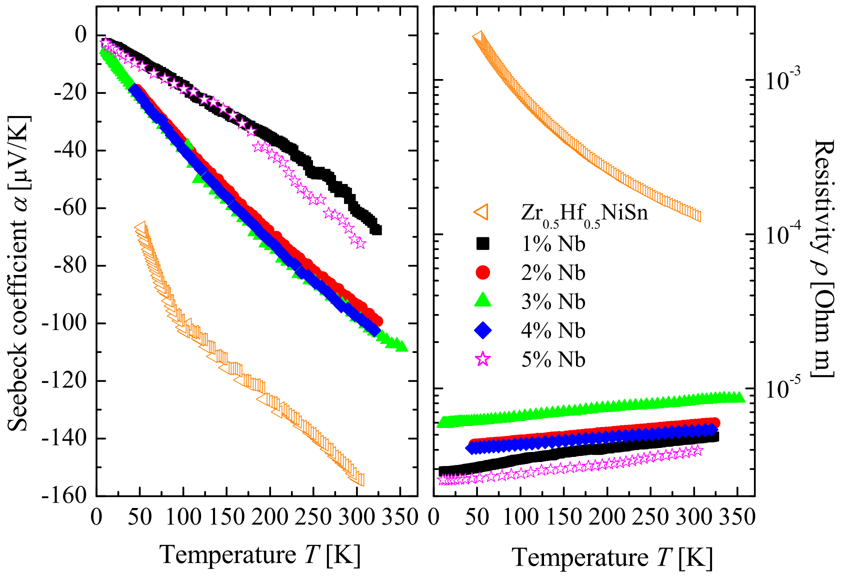

FIG. 27: Temperature dependence of the Seebeck coefficient and resistivity of $(\mathrm{Zr}_{0.5}\mathrm{Hf}_{0.5})_{(1-x)}Z_x\mathrm{NiSn}$ | $Z$: Nb ; x: 0.01-0.05 samples.

The substitution of $(\mathrm{Zr}_{0.5}\mathrm{Hf}_{0.5})$ with Nb is as strong that it changes the temperature dependence of the resistivity from a semiconducting behavior to a metallic behavior (see Figure 27). The sign of the Seebeck coefficient was negative for all samples in the temperature range from 50 K to 300 K, which indicates n-type conduction. The comparison of the Seebeck coefficient $\alpha$ of the $(\mathrm{Zr}_{0.5}\mathrm{Hf}_{0.5})_{1-x}\mathrm{Nb}_x\mathrm{NiSn}$ samples to the unsubstituted sample shows that the absolute values of the substituted samples are much lower. This is due to the higher carrier concentration. The Seebeck coefficient shows a monotonous dependence on the niobium concentration till 5% Nb. This can possibly be explained by Figure 26. With a substitution concentration of 1% Nb the localized states in the band gap (*in-gap states* [5, 31, 38, 58–62]) are filled up and the gap between the states and the conduction band is decreased (see third DOS in Fig.26), this also explains the metallic behavior of the resistivity. With higher substitutions the Seebeck coefficient increases until 3-4% Nb, which is possibly due to the new established states in the gap between the new valence band (VB*) and conduction band (CB*) (last DOS in Fig.26). 4% Nb is the point at which the carrier concentration is as high that the Seebeck coefficient is decreased. Because of this the resistivity for 5% Nb is the lowest of all samples.

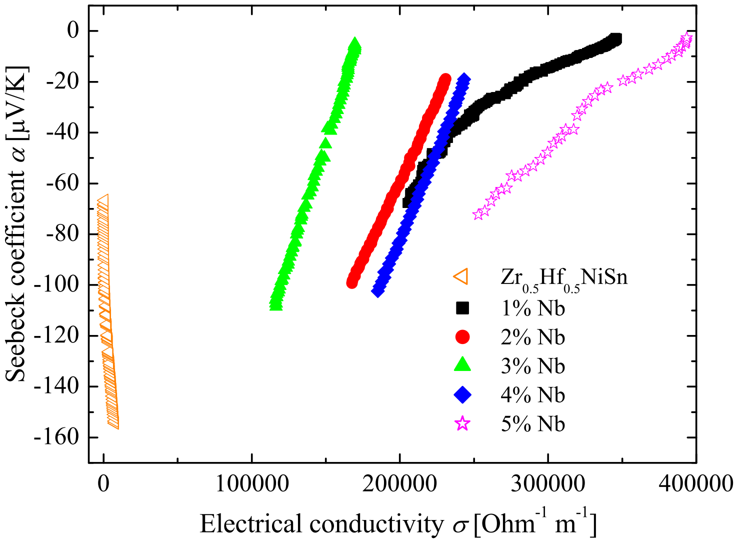

FIG. 28: Electrical conductivity dependence of the Seebeck coefficient of $(\mathrm{Zr}_{0.5}\mathrm{Hf}_{0.5})_{(1-x)}Z_x\mathrm{NiSn}$ | $Z$: Nb ; x: 0.01-0.05 samples.

Figure 28 shows the dependence of the Seebeck coefficient on the electrical conductivity. As obtained in the vanadium substitution no sample exhibits a behavior of a degenerated semiconductor with a constant mobility, just depending on the carrier concentration. In the samples with 1% Nb and 5% Nb the behavior of a non-degenerated semiconductor with a constant mobility can be obtained, meaning that the developing is approximately proportional to $ln(\frac{1}{\sigma})$. In the other three cases the mobility changes and hence the carrier effective mass and/or the scattering time changes. This is a possible prove for the assumption of resonant levels or *in-gap states* in these samples, because of the changing of the electronic structure and DOS shown in Figure 26. In Figure 29 the total thermal conductivity is shown and to compare this the electronic contribution to the thermal conductivity and the lattice thermal conductivity were calculated (Fig.30). It is recognizable that the samples with 1% and 3% Nb exhibit a development of a distorted or complex lattice structure[63, 64] due to the flat maximum at intermediate temperatures. Additionally, the samples with high Nb concentrations show the lowest lattice thermal conductivity due to the higher distortion of the lattice, which increases the phonon scattering. High electronic contributions to the thermal conductivity $\kappa_e$ are obtained, which is caused by the low resistivity values. The 5% Nb sample exhibits the lowest lattice thermal conductivity but the highest $\kappa_e$. This shows one of the main problems in thermoelectricity.

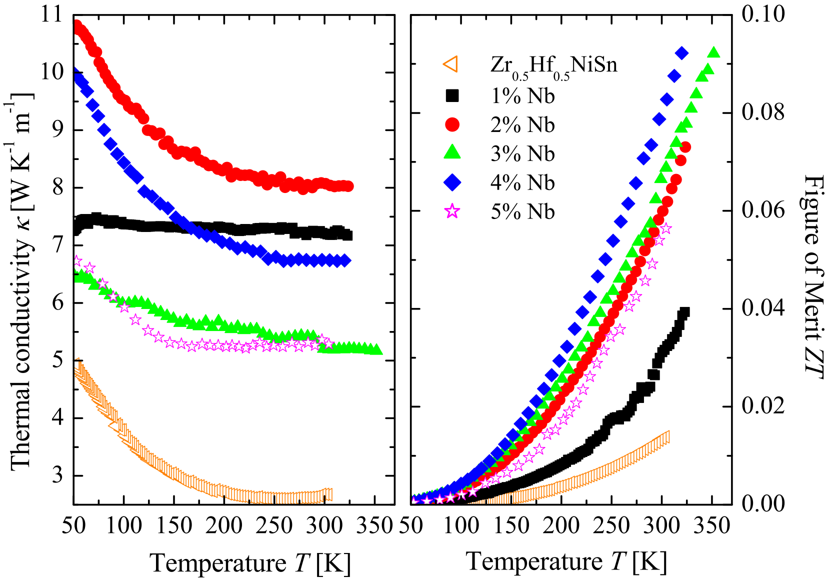

FIG. 29: Temperature dependence of the Figure of merit and the thermal conductivity of $(Zr_{0.5}Hf_{0.5})_{(1-x)}Z_xNiSn$ | $Z$: Nb ; x: 0.01-0.05 samples.

In Figure 29 the Figure of Merit of the unsubstituted $Zr_{0.5}Hf_{0.5}NiSn$ is set as a benchmark for the Nb substituted samples. The values of the dimensionless Figure of Merit of all samples increase with increasing temperature. All $ZT$ values of the substituted samples are higher than the unsubstituted once, this is due to the higher electrical conductivity of all substituted samples, except the sample with $x = 0.05$ of which the Figure of Merit increases with the increasing amount of Niobium. The maximum of the Figure of Merit is reached at $x = 0.04$ Nb concentration with a value of 0.09 at 300 K.

In summary, it has been shown that small substitutions of the $\mathrm{Zr_{0.5}Hf_{0.5}NiSn}$ system can improve the thermoelectric properties. The best value for the substitution with Nb was found at $x = 0.04$ for the $\mathrm{(Zr_{0.5}Hf_{0.5})_{1-x}Nb_xNiSn}$ series. Beyond this concentration of Nb the thermoelectric properties are decreasing due to the increasing carrier concentration. The values of the dimensionless Figure of Merit $ZT$ of the sample with $x = 0.04$ were improved by the factor of 5 in comparison to the $\mathrm{Zr_{0.5}Hf_{0.5}NiSn}$ sample.

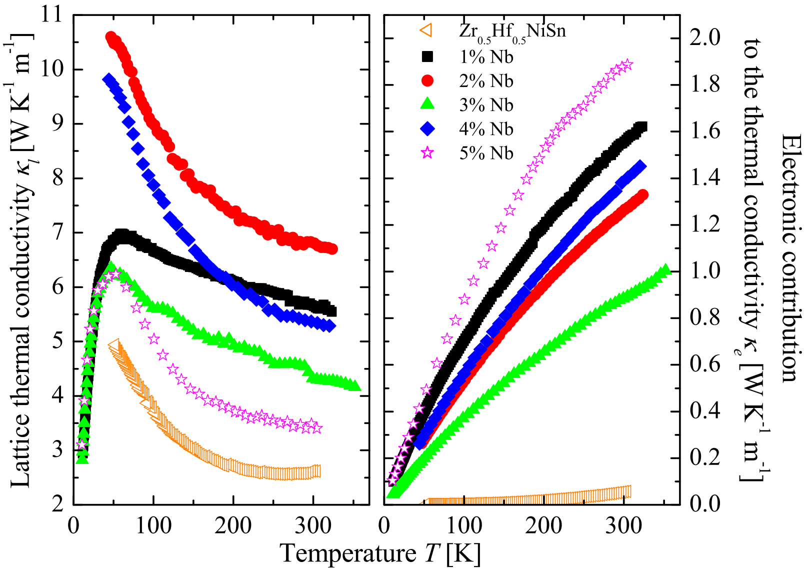

FIG. 30: Temperature dependence of the lattice thermal conductivity and the electronic contribution to the thermal conductivity of $\mathrm{(Zr_{0.5}Hf_{0.5})_{(1-x)}}Z_x\mathrm{NiSn}$ | $Z$: Nb ; x: 0.01-0.05 samples.

After the substitutions with vanadium and niobium, the idea was to see the impact of manganese substitution on the transport properties, because manganese exhibits formally three electrons more than Zr/Hf and hence the carrier concentration should be increased faster. All samples from this series exhibit the $C1_b$ structure.

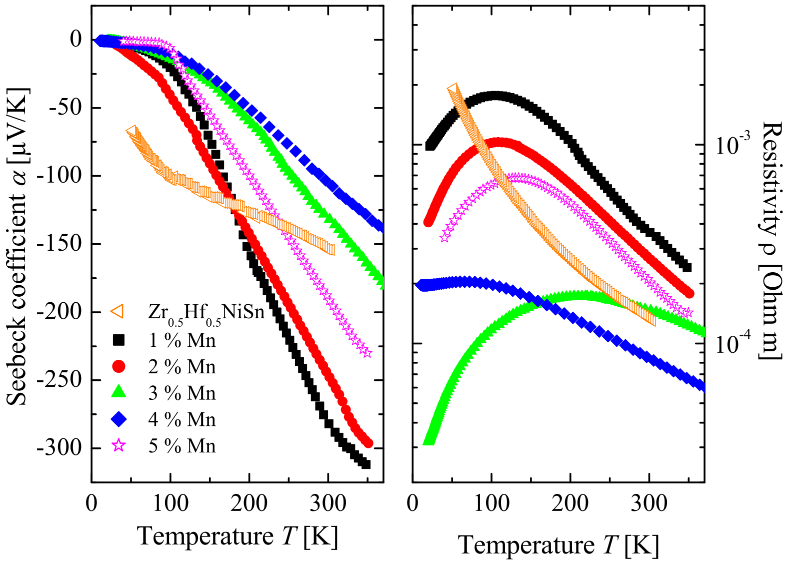

FIG. 31: Temperature dependence of the Seebeck coefficient and resistivity of $(Zr_{0.5}Hf_{0.5})_{(1-x)}Z_xNiSn$ | $Z$: Mn ; x: 0.01-0.05 samples.

In Figure 31, the measured electronic properties of the $(Zr_{0.5}Hf_{0.5})_{1-x}Mn_xNiSn$ samples are compared with the parent compound $Zr_{0.5}Hf_{0.5}NiSn$. A dependence of the values of the Seebeck coefficient and the resistivity on the manganese concentration is recognizable. The changes of the values of the Seebeck coefficient and the resistivity in the Mn substituted samples are analogous to the vanadium substitution up to a concentration of 4% manganese (see Figure 26). Above a concentration of 5% Mn the former conduction band (CB) is probably totally filled and becomes the new valence band (VB*). Additionally, between the new valence band and the new conduction band (CB*) there are still localized states (*in-gap states*) caused by the high distortion in the structure, what leads to a n-type semiconducting sample.[5, 28, 31, 38, 58–62] An indication for the former filled conduction band is that even the sample with the lowest resistivity value exhibits a high resistivity value in comparison

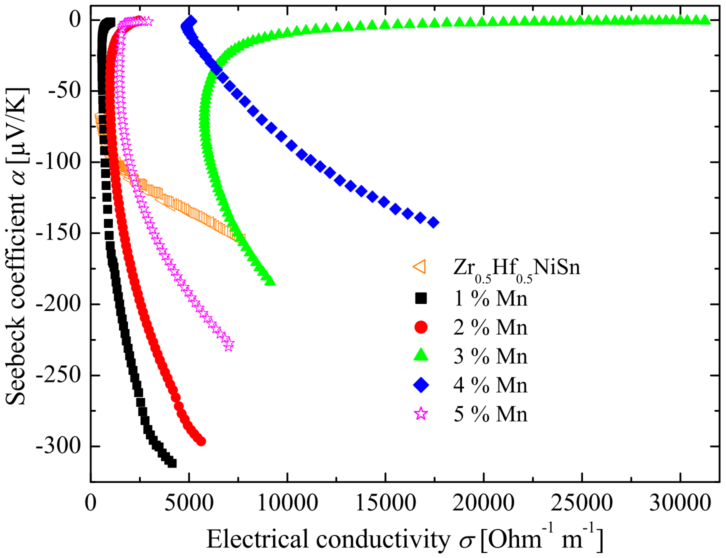

FIG. 32: Electrical conductivity dependence of the Seebeck coefficient of $(\mathrm{Zr}_{0.5}\mathrm{Hf}_{0.5})_{(1-x)}Z_x\mathrm{NiSn}$ | $Z$: Mn ; x: 0.01-0.05 samples.

to the other substitutions, e.g. vanadium. This probably means that the conduction band is really flat and can be easily filled by adding certain number of electrons. This was done by increasing the Mn concentration, because the manganese formally exhibits three electrons more than Zr/Hf. In Figure 32 the dependence of the Seebeck coefficient on the electrical conductivity is shown. No sample exhibits the $(\sigma)^{-\frac{3}{2}}$ or $ln(\frac{1}{\sigma})$ behavior, proving that the carrier effective mass and/or the scattering time change. The developing of the electrical resistivity of the samples with 1%, 2% and 5% Mn is similar, fitting to the possible explanations above, because of their analogy in the DOS (see Figure 26). Also the maxima in the temperature dependent resistivity measurements at low temperatures is typical for established resonant levels.[28, 59] In Figure 33 the thermal conductivity of the $(\mathrm{Zr}_{0.5}\mathrm{Hf}_{0.5})_{1-x}\mathrm{Mn}_x\mathrm{NiSn}$ samples is compared to the parent sample. All manganese substituted samples exhibit a higher thermal conductivity in comparison to the parent compound. The Mn samples of the higher substituted samples show the lowest lattice thermal conductivity (see Figure 34) due to the same reason like the ones for vanadium and niobium, the higher distortion of the lattice structure. The electronic contribution to the thermal conductivity $\kappa_e$ has a lower impact on the total thermal conductivity, because of the high values of the resistivity, what leads into low $\kappa_e$ values. Altogether, the Figure of Merit of the low Mn concentrations is comparable with the parent sample. The huge disadvantage is the really high resistivity, which decreases the Figure of Merit. The highest values for the Figure of Merit are obtained in the 1% and 2% Mn substituted samples with ZT= 0.02 at 300 K.

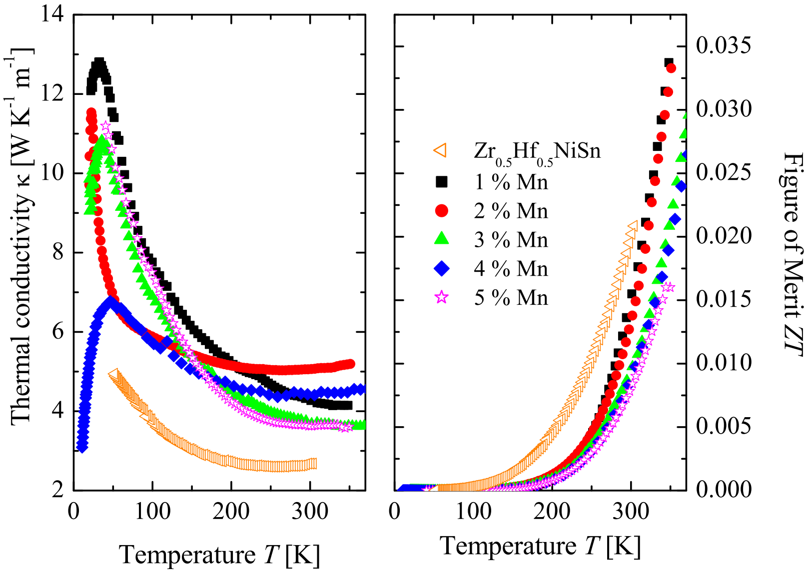

FIG. 33: Temperature dependence of the Figure of Merit and the thermal conductivity of $(Zr_{0.5}Hf_{0.5})_{(1-x)}Z_x$NiSn | $Z$: Mn ; x: 0.01-0.05 samples.

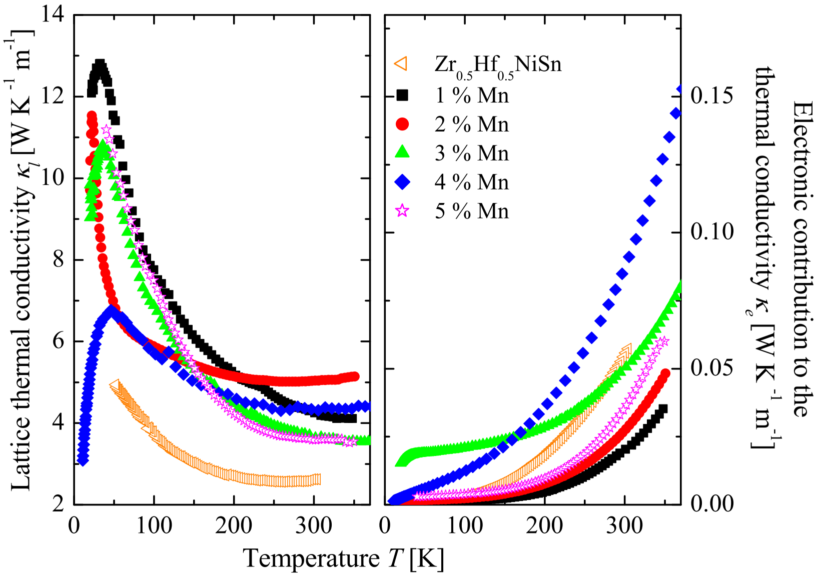

FIG. 34: Temperature dependence of the lattice thermal conductivity and the electronic contribution to the thermal conductivity of $(\mathrm{Zr}_{0.5}\mathrm{Hf}_{0.5})_{(1-x)}Z_x\mathrm{NiSn}$ | $Z$: Mn ; x: 0.01-0.05 samples.

The intention of the experiment of substituting the Ni atoms with Ag atoms was on the one hand to see the influence of the substitution on this position and on the other hand to possibly decrease the high values of the resistivity of the parent sample. With respect to the demands of the industry, small concentrations of silver were added to keep the material cost low. All samples from this series exhibit the $C1_b$ structure.

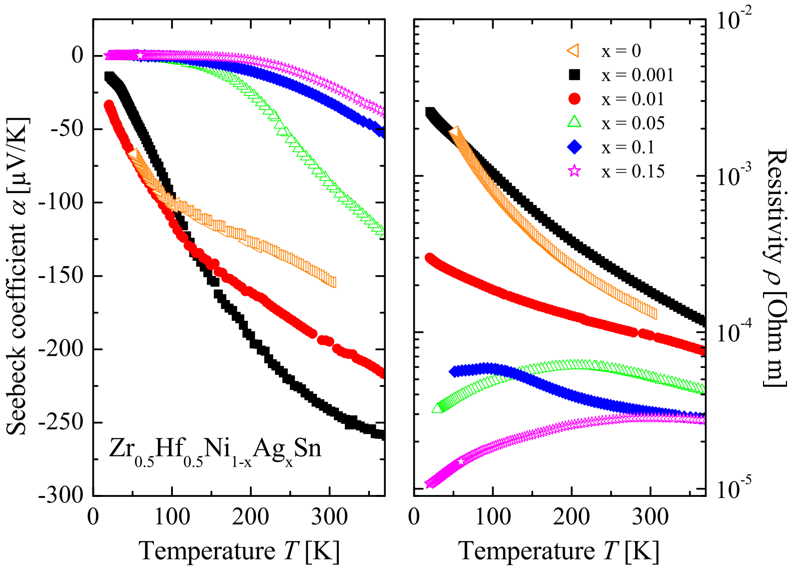

FIG. 35: Temperature dependence of the Seebeck coefficient and resistivity of $\mathrm{Zr}_{0.5}\mathrm{Hf}_{0.5}\mathrm{Ni}_{(1-x)}Ag_x\mathrm{Sn}$ | x: 0.001; 0.01; 0.01; 0.05; 0.1; 0.15 samples.

In Figure 35, the measured electronic properties of the $\mathrm{Zr}_{0.5}\mathrm{Hf}_{0.5}\mathrm{Ni}_{1-x}\mathrm{Ag}_x\mathrm{Sn}$ samples are compared with the parent compound $\mathrm{Zr}_{0.5}\mathrm{Hf}_{0.5}\mathrm{NiSn}$. Concerning the values of the Seebeck coefficient a clear dependence on the Ag concentration is obtained. With an increasing silver concentration the Seebeck coefficient is decreased. The 0.1% Ag substitution exhibits a larger value of the Seebeck coefficient due to the introduced distortion of the structure. The number of states near the conduction band is possibly increased and hence the effective mass $m^*$ is increased, which increases the value of the Seebeck coefficient (see Figure 26).[5, 31, 38, 58–62]. The possible increase of the effective mass can also be seen in Figure 36. Additionally, the dependence of the Seebeck coefficient on the electrical conductivity is shown. It is recognizable that non of the samples follows the behavior of a degenerated

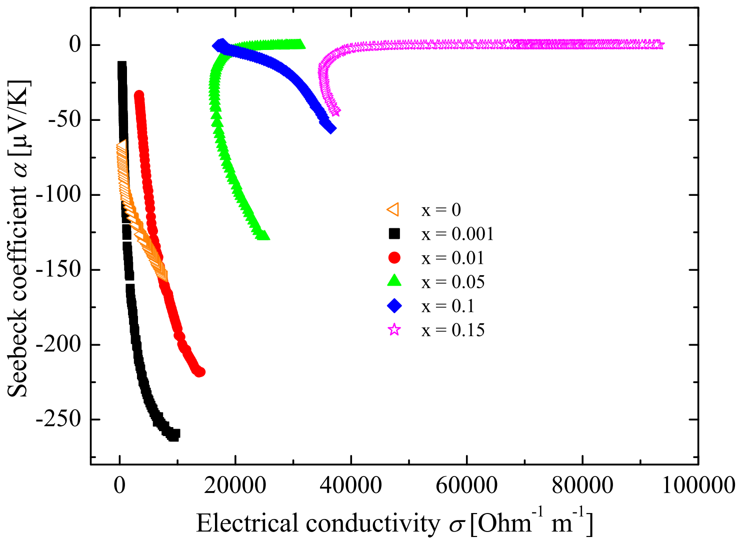

FIG. 36: Electrical conductivity dependence of the Seebeck coefficient of $\mathrm{Zr}_{0.5}\mathrm{Hf}_{0.5}\mathrm{Ni}_{(1-x)}Ag_x\mathrm{Sn}$ | x: 0.001; 0.01; 0.01; 0.05; 0.1; 0.15 samples.

or non-degenerated semiconductor with constant mobility. This means that the mobility is changed due to a change of the carrier effective mass and/or the scattering time. Above 0.1% Ag the gap between the localized states and the conduction band is decreased due to the increasing carrier concentration, because silver formally exhibits one valence electron more than Zr/Hf, and with thus the values of the Seebeck coefficient decreases. Concerning the values of the resistivity they act analogous to the Seebeck coefficient. With 0.1% Ag the resistivity is slightly increased. At higher silver concentrations the resistivity is decreased by the increasing carrier concentration.

In Figure 37 the thermal conductivity of the $\mathrm{Zr}_{0.5}\mathrm{Hf}_{0.5}\mathrm{Ni}_{1-x}\mathrm{Ag}_x\mathrm{Sn}$ samples is compared to the parent sample. All silver substituted samples exhibit a higher thermal conductivity in comparison to the parent compound. But almost all the silver substituted samples have lower values of the resistivity, meaning that the electronic contribution to the thermal conductivity $\kappa_e$ is higher and hence it is not unexpected that the values of the thermal conductivity of the Ag samples are higher (see Figure 38). A clear dependence of the thermal conductivity on the silver concentration is recognizable. The thermal conductivity is increased with increasing silver concentration and the same trend is obtained for $\kappa_e$. The increase of the electronic contribution to the thermal conductivity is due to the decreasing resistivity with increasing

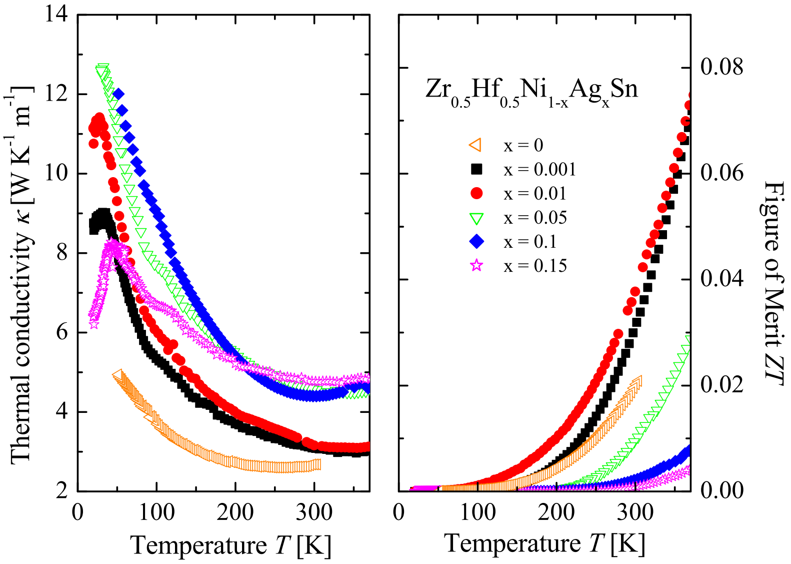

FIG. 37: Temperature dependence of the Figure of Merit and the thermal conductivity of $\mathrm{Zr}_{0.5}\mathrm{Hf}_{0.5}\mathrm{Ni}_{(1-x)}Ag_x\mathrm{Sn}$ | x: 0.001; 0.01; 0.01; 0.05; 0.1; 0.15 samples.

silver concentration, because of the increasing carrier concentration. By comparing the lattice thermal conductivity of the 0.1%, 1% Ag and the parent sample almost the same value is obtained at 300 K. This can be explained by the extremely low silver concentrations, which do not significantly disturb the lattice structure. The samples with 5%, 10% and 15% silver exhibit almost the same lattice thermal conductivity, which can possibly explained by the higher crystallinity in the samples. All properties combined lead to an increased Figure of Merit for the low silver concentration due to the higher values of the Seebeck coefficient and the comparable values for resistivity and thermal conductivity. A maximum value is obtain for the 0.1% and 1% Ag substituted samples of ZT= 0.04 at 300 K. In summary the Figure of Merit was increased by the factor of two with slight substitution of Ag on the Ni position.

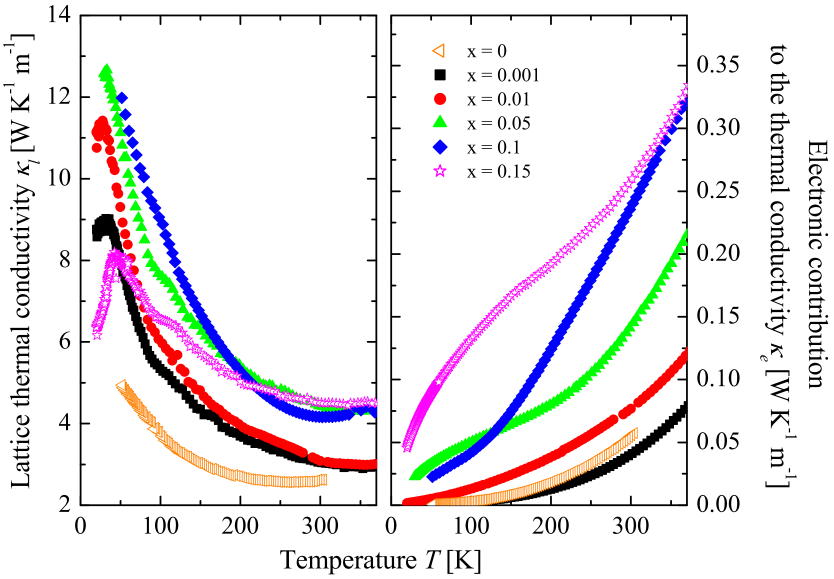

FIG. 38: Temperature dependence of the lattice thermal conductivity and the electronic contribution to the thermal conductivity of $Zr_{0.5}Hf_{0.5}Ni_{(1-x)}Ag_xSn$ | x: 0.001; 0.01; 0.01; 0.05; 0.1; 0.15 samples.

The p-type substitution was an attempt to create a p-type semiconductor with adequate thermoelectric properties. The benefit of a p-type thermoelectric material, which has almost the same composition as the n-type material, is that almost all mechanical properties are equal and thus the handling is comparable.

All samples from this series exhibit the $C1_b$ structure. In Figure 39, the measured electronic properties of the $(\mathrm{Zr}_{0.5}\mathrm{Hf}_{0.5})_{1-x}\mathrm{Sc}_x\mathrm{NiSn}$ samples are compared with the unsubstituted $\mathrm{Zr}_{0.5}\mathrm{Hf}_{0.5}\mathrm{NiSn}$. The values of the Seebeck coefficients increase with increasing Sc concentration, this is due to the fact that electrons of the parent compound are removed and at a scandium concentration of 2% holes are the dominating carrier type. The slope of all p-type semiconducting samples show a linear dependence of the values of the Seebeck coefficient from the temperature. The maximum value of the Seebeck coefficient is achieved in the 5% Sc substituted sample and exhibits a value of $\alpha \approx 57\ \frac{\mu V}{K}$ at 300 K. Additionally, in Figure 39 the values of the electrical resistivity are compared with the parent compound. In comparison to the parent phase the resistivity of the 1% Sc sample exhibits a value one order of magnitude lower. The resistivity values of the Sc substituted sample increase with

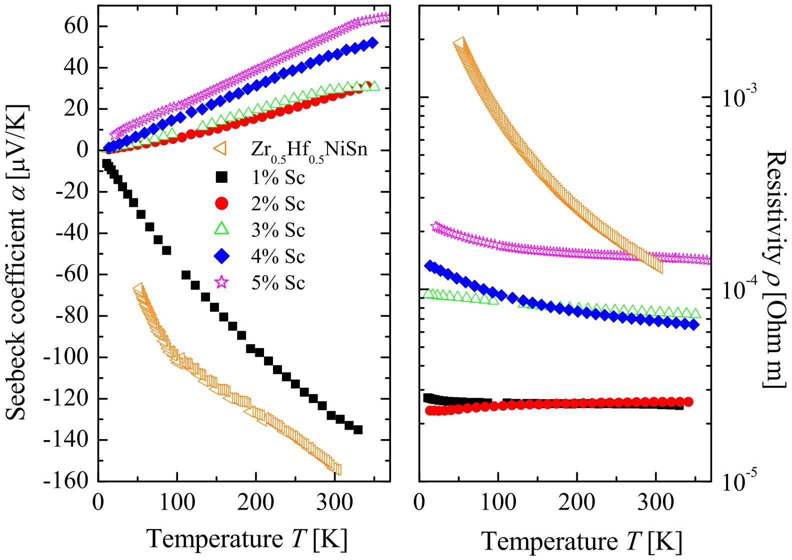

FIG. 39: Temperature dependence of the Seebeck coefficient and resistivity of $(\mathrm{Zr}_{0.5}\mathrm{Hf}_{0.5})_{(1-x)}Z_x\mathrm{NiSn}$ | $Z$: Sc ; x: 0.01-0.05 samples.

increasing scandium concentration due to the decreasing number of electrons in the samples. Also the temperature behavior of the resistivity changes from metallic behavior at 2% Sc to almost temperature independent at 3% Sc to semiconducting at 4% Sc and 5% Sc. The 1% Sc substituted sample and the 2% Sc sample exhibit values of the resistivity in the same order of magnitude, but they have different carrier types. The same behavior is recognizable within the 3% Sc and 4% Sc samples. They have comparable resistivity values. The 5% Sc substituted sample exhibits a resistivity value in the same order of magnitude like the parent phase and shows the largest positive values for the Seebeck coefficient. In Figure 40 the dependence of the Seebeck coefficient on the electrical conductivity is shown. Non of the samples exhibits the behavior of a degenerated or non-degenerated semiconductor with constant mobility. So the mobility changes due to the change of the effective mass and/or the scattering time. This can be explained by the fact that the electrons are removed out of the localized states in the band gap by adding Sc into the system. Somewhere between 1% and 2% Sc the localized states are empty, by adding more Sc the Fermi energy is shifted into the valence band (see Figure 43). In Figure 41 the thermal conductivity of the $(Zr_{0.5}Hf_{0.5})_{1-x}Sc_xNiSn$ samples is compared to the parent sample. All scandium substituted samples exhibit a higher thermal conductivity in comparison to the parent compound.

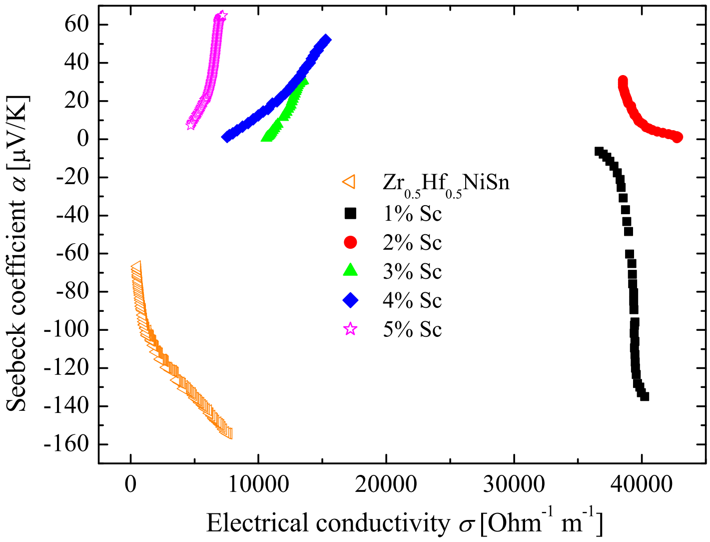

FIG. 40: Electrical conductivity dependence of the Seebeck coefficient of $(Zr_{0.5}Hf_{0.5})_{(1-x)}Z_xNiSn$ | $Z$: Sc ; x: 0.01-0.05 samples.

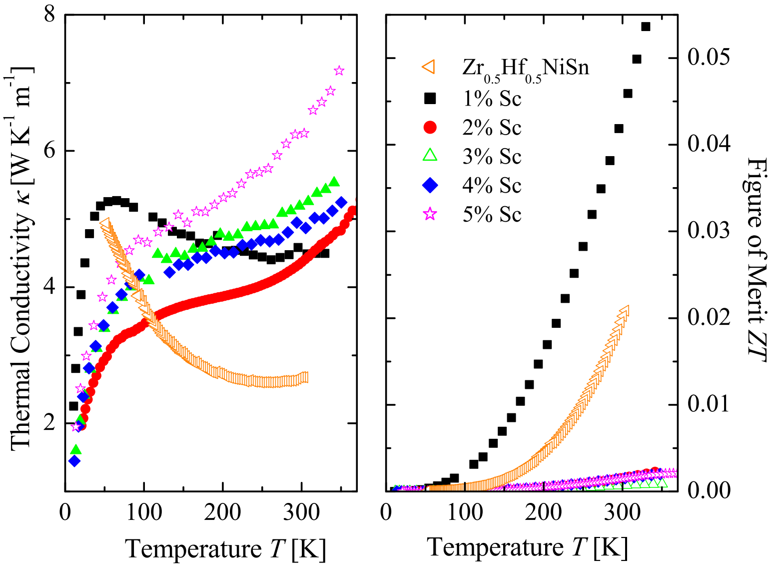

FIG. 41: Temperature dependence of the Figure of Merit and the thermal conductivity of $(\mathrm{Zr}_{0.5}\mathrm{Hf}_{0.5})_{(1-x)}Z_x\mathrm{NiSn}$ | $Z$: Sc ; x: 0.01-0.05 samples.

The scandium substituted samples have lower values of the resistivity, meaning that the electronic contribution to the thermal conductivity is higher and hence it is not unexpected that the values of the thermal conductivity of the Sc samples are higher (see Figure 42). The lattice thermal conductivity shows the same behavior of the Sc substitution like the Seebeck coefficients. It can be seen easily that the development of the lattice thermal conductivity of the parent sample and the 1% Sc substituted one is alike, related to this the development of the 2% till 5% Sc substituted sample is similar. The thermal conductivity of the parent sample is expected to show a maximum at intermediate temperatures due to a compensation of the increasing number of phonons contributing to the transport and due to the increasing contribution from Umklapp processes causing scattering with increasing temperatures. The additional scattering at grain boundaries cause a decrease of $\kappa_l$. This expected temperature dependence of $\kappa(T)$ is observed at lower temperatures with the maximum located below T= 50 K. The maximum of the 1% Sc substituted sample is located at T= 65 K. The lattice thermal conductivity of the other scandium substituted samples show typical behavior of a compound with a complex unit cell in a quasicrystal or amorphous metal.[63, 64] The tail at 300 K in the lattice thermal conductivity of these samples can be explained by bipolar diffusion.[36]

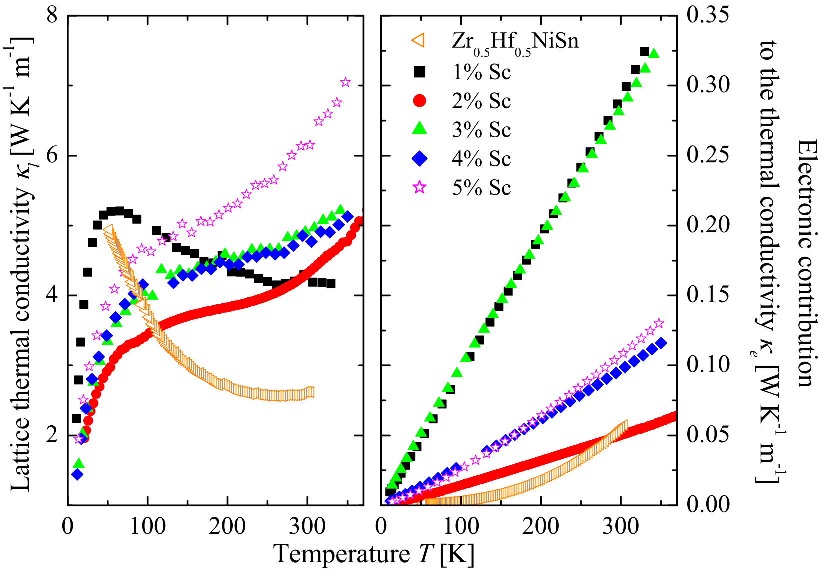

FIG. 42: Temperature dependence of the lattice thermal conductivity and the electronic contribution to the thermal conductivity of $(Zr_{0.5}Hf_{0.5})_{(1-x)}Z_xNiSn$ | $Z$: Sc ; x: 0.01-0.05 samples.

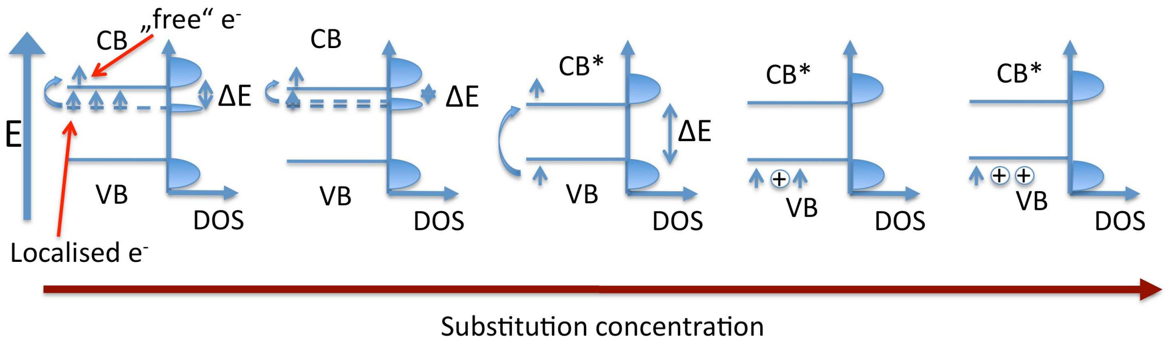

FIG. 43: Possible change in the electronic structure and density of states of the parent Heusler compound in dependence of the substitution concentration at 300 K.

All samples from the yttrium substituted series exhibit the $C1_b$ structure. In Figure 44, the measured electronic properties of the $(\mathrm{Zr}_{0.5}\mathrm{Hf}_{0.5})_{1-x}\mathrm{Y}_x\mathrm{NiSn}$ samples are compared to the unsubstituted $\mathrm{Zr}_{0.5}\mathrm{Hf}_{0.5}\mathrm{NiSn}$. The samples with 1% to 5% yttrium have a p-type conducting n-type conducting transition in the Seebeck coefficient values at different temperatures. The p-n transition temperatures rise with increasing yttrium concentration. Additionally, the gradient of the development decreases with increasing yttrium concentration, except within the 1% Y sample, which shows metallic behavior of the Seebeck coefficient values. All yttrium substituted samples therefore exhibit maxima, 1% at ≈ 200 K, 2% at ≈ 199 K, 3% at ≈ 271 K, 4% at ≈ 308 K and 5% at ≈ 281 K, which indicate bipolar conduction. The position of the maxima is shifted to higher temperatures with increasing yttrium concentration, except within the 5% Y sample. Also the values of the Seebeck coefficient show a dependence of the yttrium concentration. With increasing yttrium concentration the values increase, because more and more holes are created and hence the electrons need more energy to be activated to contribute to the conduction. In the parent sample n-type conducting is dominating, caused by states near the conduction band, which were produced by defects

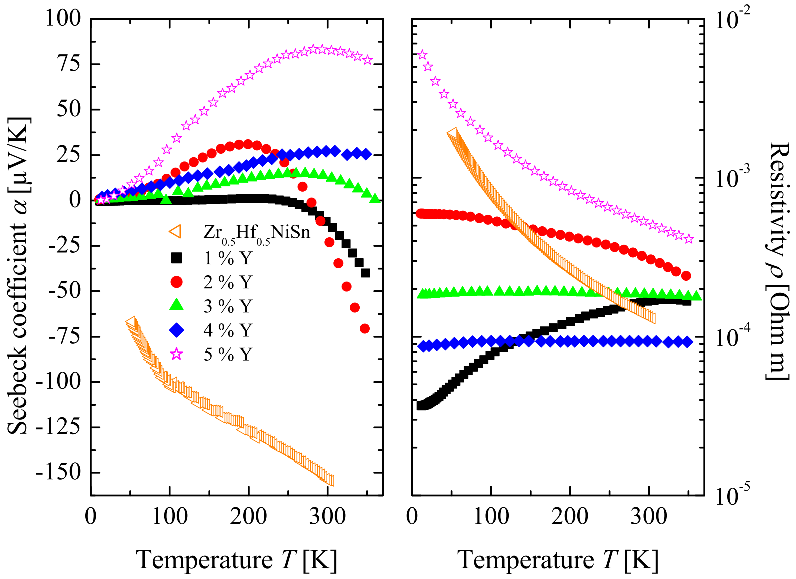

FIG. 44: Temperature dependence of the Seebeck coefficient and resistivity of $(\mathrm{Zr}_{0.5}\mathrm{Hf}_{0.5})_{(1-x)}Z_x\mathrm{NiSn}$ | $Z$: Y ; x: 0.01-0.05 samples.

and distortions [5, 31, 38, 58–62], are occupied by electrons, which can be excited into the conduction band causing n-type conduction. Due to the higher disorder caused by 1% Y substitution the states near the conduction band are probably increased, leading into lower values of the Seebeck coefficient and the resistivity shows a metallic behavior (see Figure 43). At 2% Y substitution an almost intrinsic semiconducting behavior is obtained, which can

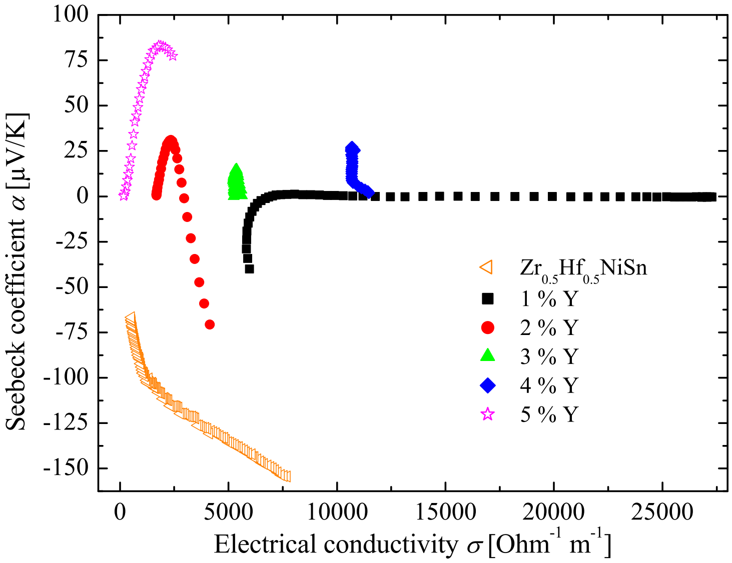

FIG. 45: Electrical conductivity dependence of the Seebeck coefficient of $(\mathrm{Zr}_{0.5}\mathrm{Hf}_{0.5})_{(1-x)}Z_x\mathrm{NiSn}$ | $Z$: Y ; x: 0.01-0.05 samples.

also be seen in the higher resistivity, due to the larger gap, in comparison to the other samples. Within 3% Y holes are produced in the valence band, causing p-type conduction behavior, meaning that the Fermi energy is shifted into the valence band. Above 3% Y more holes are created and hence possibly the carrier concentration and the mobility, which is probably increased by a change of the carrier effective mass and/or the scattering time (see Figure 45), are increased, leading to higher values for the Seebeck coefficient and a lower resistivity (4% Y). At 5% Y the valence band is probably almost empty, leading to a low carrier concentration. This increases the values of the Seebeck coefficient up to S= 82 $\frac{\mu V}{K}$ at 300 K and the resistivity is increased, too. Figure 45 shows again the dependence of the Seebeck coefficient on the electrical conductivity and the same behavior of the Sc substitution is recognizable. In Figure 46 the thermal conductivity of the $(\mathrm{Zr}_{0.5}\mathrm{Hf}_{0.5})_{1-x}\mathrm{Y}_x\mathrm{NiSn}$ samples is shown. The yttrium samples show no clear dependence of the lattice thermal conductivity

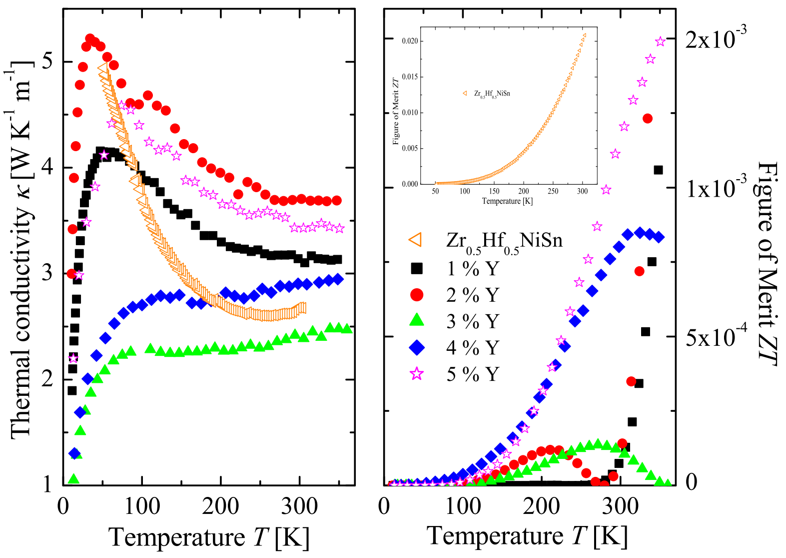

FIG. 46: Temperature dependence of the Figure of Merit and the thermal conductivity of $(\mathrm{Zr}_{0.5}\mathrm{Hf}_{0.5})_{(1-x)}Z_x\mathrm{NiSn}$ | $Z$: Y ; x: 0.01-0.05 samples.

on the yttrium concentration, possibly due to the different crystallinities.

The development of the parent, 1%, 2% and 5% Y substituted samples show a maximum in the lattice thermal conductivity at low temperatures due to the compensation of the increasing number of phonons contributing to the transport and increasing contribution of Umklapp processes causing scattering with increasing temperature (see Figure 47). The 3% Y and 4% Y substituted samples do not show a maximum at intermediate temperatures, which is a typical development of a compound with a complex unit cell in a quasicrystal or amorphous metal [63, 64], like in the scandium substituted samples. Interestingly, the two samples with the lowest resistivity, meaning the ones exhibiting the highest electronic contribution to the thermal conductivity $\kappa_e$, possess one of the lowest thermal conductivities. This implies that the lattice thermal conductivity $\kappa_l$ is very low, due to additional scattering caused by the distorted structure. In Figure 46 the Figure of Merit is also plotted (inset shows the parent sample). All physical properties combined result in a low Figure of Merit due to the low values of the Seebeck coefficient and the high resistivities values. The maximum of the Figure of Merit is achieved by the 5% Y sample with a value of ZT= 0.001 at 300 K.

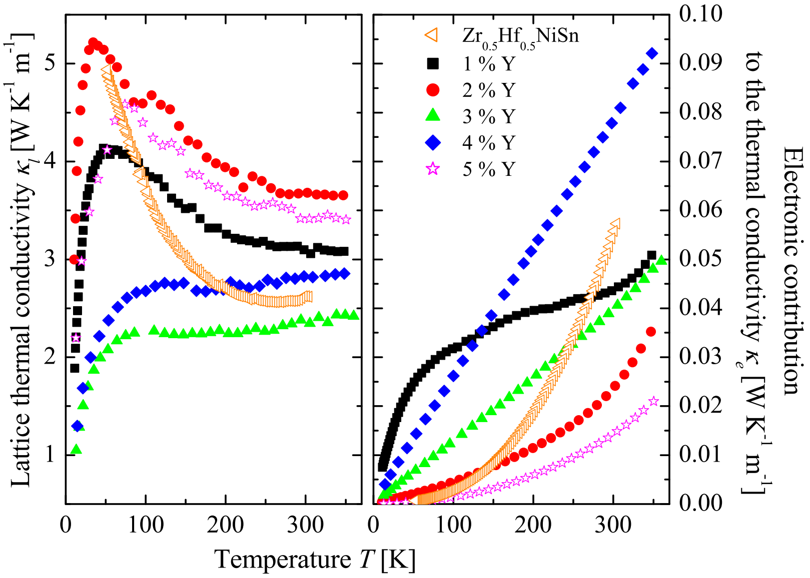

FIG. 47: Temperature dependence of the lattice thermal conductivity and the electronic contribution to the thermal conductivity of $(\mathrm{Zr}_{0.5}\mathrm{Hf}_{0.5})_{(1-x)}Z_x\mathrm{NiSn}$ | $Z$: Y ; x: 0.01-0.05 samples.

The advantage of aluminum is its low price in comparison to scandium and yttrium, what could be promising for industrial applications. The produced aluminum samples all exhibit the $C1_b$ structure. In Figure 48, the measured electronic properties of the $(\mathrm{Zr}_{0.5}\mathrm{Hf}_{0.5})_{1-x}\mathrm{Al}_x\mathrm{NiSn}$ samples are compared to the parent compound $\mathrm{Zr}_{0.5}\mathrm{Hf}_{0.5}\mathrm{NiSn}$.

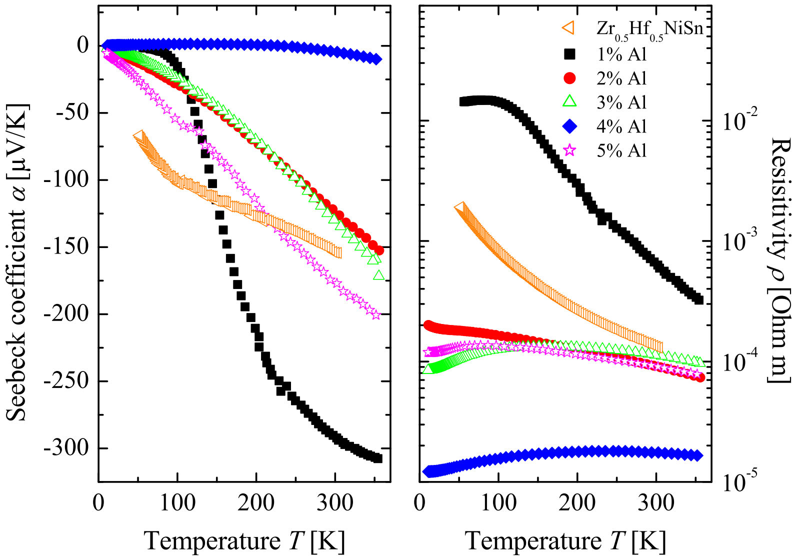

FIG. 48: Temperature dependence of the Seebeck coefficient and resistivity of $(\mathrm{Zr}_{0.5}\mathrm{Hf}_{0.5})_{(1-x)}Z_x\mathrm{NiSn}$ | $Z$: Al ; x: 0.01-0.05 samples.

The parent sample is a n-type semiconducting material, the disorder is increased by the substitution with aluminum causing the formation of localized states or resonant levels in the conduction band.[5, 28, 31, 38, 58–62] This is proved by the dependence of the Seebeck coefficients on the aluminum concentration. Small Al concentrations increase the values of the Seebeck coefficient (1% Al). The effective mass $m^*$ is possibly increased due to the sharp resonant levels, leading to higher values of the 1% Al substituted sample for the Seebeck coefficient (see Figure 26). Also the resistivity of the 1% Al sample is increased due to the higher effective mass $m^*$ (see Figure 50). A possible prove for this is shown in Figure 49. All samples exhibit a behavior of a changing mobility, meaning that the carrier effective mass and/or the scattering time must have changed. By increasing the aluminum concentration the values of the Seebeck coefficient decrease as well as the resistivity values. At an

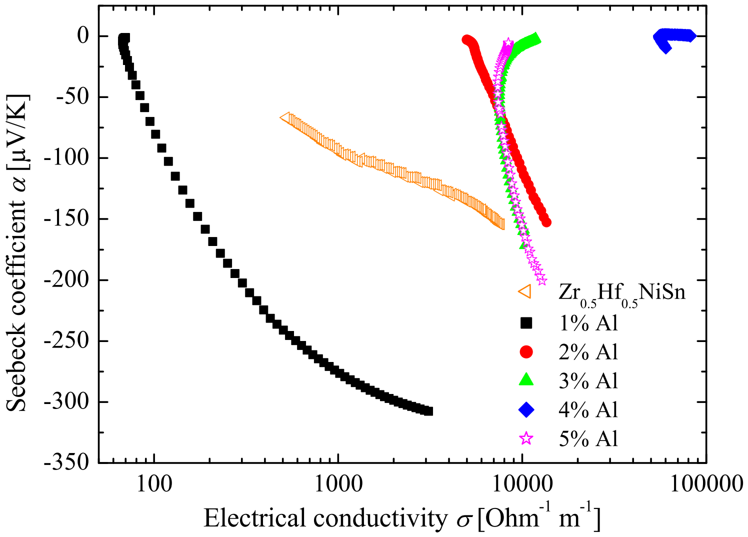

FIG. 49: Electrical conductivity dependence of the Seebeck coefficient $(\mathrm{Zr}_{0.5}\mathrm{Hf}_{0.5})_{(1-x)}Z_x\mathrm{NiSn}$ | $Z$: Al ; x: 0.01-0.05 samples.

aluminum concentration of 4% the Seebeck coefficient and the resistivity indicate metallic behavior. This again can be explained by the *in-gap states* or resonant levels, which are broadened at high substitution concentrations and therefore touch the conduction band, leading to a metallic behavior. The 5% Al substituted sample exhibits a higher value of the Seebeck coefficient, which can possibly be explained by Figure 26. At concentrations higher than 4% Al the localized states and the conduction band build up a new valence band (VB*). Meaning that between 4% Al and 5% Al an intrinsic semiconducting behavior should be obtained. At 5% Al probably new localized states are established between the new VB* and CB*, leading to higher values of the Seebeck coefficient and a lower resistivity. In Figure 50 the thermal conductivity of the $(\mathrm{Zr}_{0.5}\mathrm{Hf}_{0.5})_{(1-x)}\mathrm{Al}_x\mathrm{NiSn}$ samples is compared to the parent compound, which exhibits the lowest value of the thermal conductivity. The aluminum samples show a dependence of the lattice thermal conductivity on the aluminum concentration. With increasing aluminum concentration the lattice thermal conductivity is decreased until 4% Al (see Figure 51). After 4% Al $\kappa_l$ is increased, possibly due to the better crystallinity. The sample with 4% Al shows the typical development of a compound with a complex unit cell in a quasicrystal or amorphous metal.[63, 64] This trend is caused by the increasing strain and disorder in the sample with increasing aluminum concentration. At

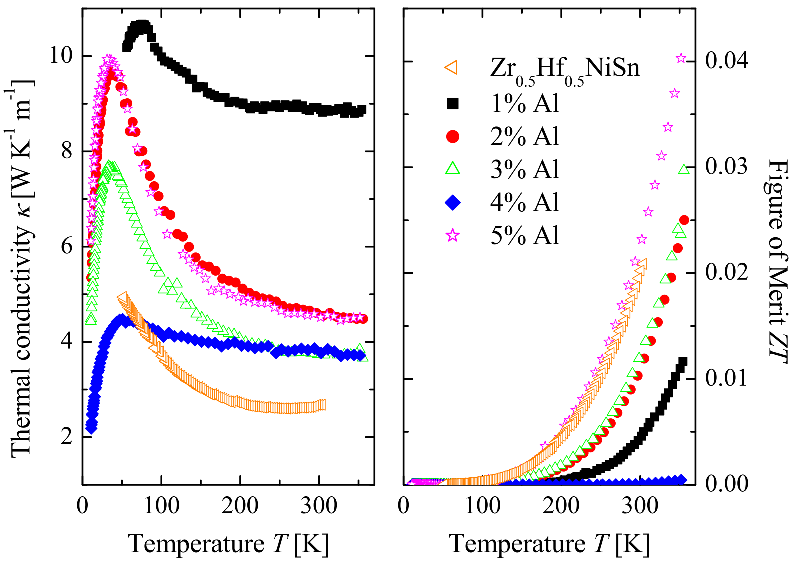

FIG. 50: Temperature dependence of the Figure of Merit and the thermal conductivity of $(\mathrm{Zr}_{0.5}\mathrm{Hf}_{0.5})_{(1-x)}Z_x\mathrm{NiSn}$ | $Z$: Al ; x: 0.01-0.05 samples.

5% Al the thermal conductivity increases and the development shows the typical maximum of a crystalline compound at low temperatures. The electronic contribution to the thermal conductivity is, except for the 4% Al sample, in the same order of magnitude due to comparable resistivity values. The 4% Al substituted sample shows a metallic behavior of the resistivity, causing a high $\kappa_e$. The resulting Figure of Merit is lower than for the parent compound and as mentioned above just n-type conducting samples were obtained. Hence the objective of a p-type conducting material with the low costing aluminum could not be reached.

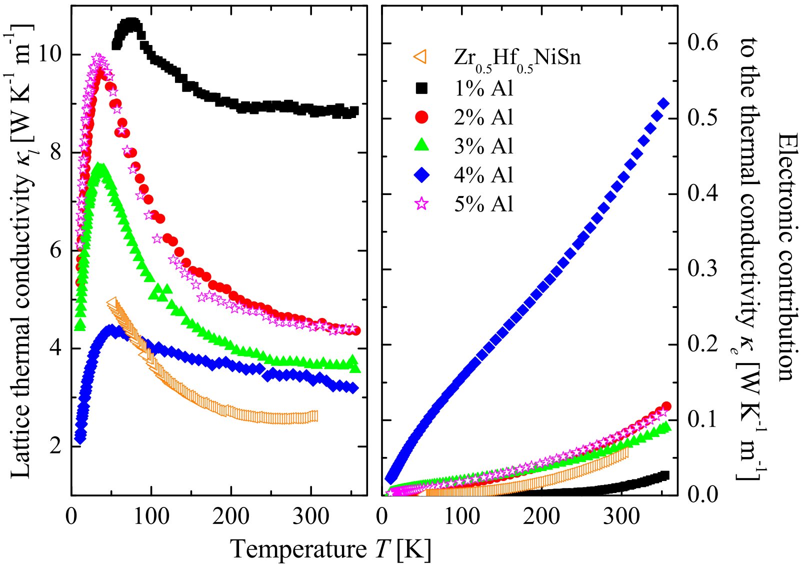

FIG. 51: Temperature dependence of the lattice thermal conductivity and the electronic contribution to the thermal conductivity of $(\mathrm{Zr}_{0.5}\mathrm{Hf}_{0.5})_{(1-x)}Z_x\mathrm{NiSn}$ | $Z$: Al ; x: 0.01-0.05 samples.

In summary, the substitutions can be divided into two parts, one part with the aim to improve the n-type material (V, Nb, Mn and Ag) and another to create a p-type material (Sc, Y and Al). The n-type substitutions can also be divided into substitutions on the Zr/Hf position (V, Nb and Mn) and on the Ni position (Ag). The vanadium substitution leads to an improvement of the Figure of Merit by a factor of 6, which is mainly explainable by to the lower resistivity values. Similar behavior is shown by the Nb substitution. By substituting Zr/Hf with Nb the $ZT$ value was improved by a factor of 5 also caused by a lower resistivity. The impact of the niobium on the parent compound seems to be higher in comparison to the vanadium substitution. The manganese substitution was not as effective for the improvement of the Figure of Merit, but the values of the Seebeck coefficients and hence the values of the resistivity were increased. This result was not expected because the manganese, which formally exhibits three valence electrons more than the parent sample, should increase the carrier concentration strongly. Instaed a possible change in the electronic structure next to the Fermi energy was obtained (Figure 26). The Ag substitution on the Ni position leads to an improvement of the Figure of Merit by a factor of 2 at low Ag concentrations. In comparison to the substitutions with V and Nb the impact on the transport properties is not as strong.

The substitution with scandium on the Zr/Hf position caused a n-p transition at 2% Sc. The obtained Figure of Merit (ZT= 0.0015) was still 10 times lower than the value of the parent sample. Similar results are obtained for the yttrium substitution, but with a weaker impact on the physical properties. The achieved Figure of Merit was 15 times lower than the value of the parent sample. The last substitution with aluminum showed no n-p transition. This substitution showed a similar behavior like the one found in the Mn substitution. High values of the Seebeck coefficient and the resistivity were obtained caused by a change of the electronic structure next to the Fermi energy (Figure 26).

### B. Phase separation

One characteristic of the Heusler compounds is their high electrical conductivity, which leads on the one hand to a high powerfactor and on the other hand to a large thermal conductivity according to the Wiedemann-Franz law (equation 26 ).[18, 65] The main obstacle for the use of Heusler compounds in thermoelectric applications is their high lattice thermal conductivity, which has to be reduced to achieve a large Figure of Merit. Several approaches to reduce the lattice thermal conductivity have been proposed. Hohl *et al.* reported that mass disorder in the X-site lattice causes additional phonon scattering and thereby reduces the thermal conductivity.[19, 20, 36] Another approach is the creation of a nano or micro structure in the sample, this increases the number of grain boundaries for example by sintering of nano particles or by a fine grained phase separation induced by rapid quenching.[66–69] The challenge of this approach is to preserve structural stability over a wide temperature range. In many inhomogeneous compounds the grains of the polycrystalline sample tend to grow at higher temperatures and with increasing time. This grain coarsening reduces the grain boundaries and increases the thermal conductivity [36]. The idea of this part of the thesis was to apply a temperature stable phase separation, a segregation or decomposition, on the system, which causes increasing grain boundary scattering and hence reduces the thermal conductivity.

Due to the previous work of Graf et al.[21, 67] it was the intention to apply a phase separation on the $Co_2X_{0.5}Z_{0.5}Sn$ | *X*: Mn, V, Ti ; *Z*: Y, V, Sc, Dy, Cr, Fe system. The compositions are:

- $Co_2Fe_{0.5}Ti_{0.5}Sn$,
- $Co_2Dy_{0.5}Mn_{0.5}Sn$,
- $Co_2Cr_{0.5}V_{0.5}Sn$,
- $Co_2Mn_{0.5}Sc_{0.5}Sn$,
- $Co_2Cr_{0.5}Mn_{0.5}Sn$,
- $Co_2Mn_{0.5}V_{0.5}Sn$,
- $Co_2Mn_{0.5}Y_{0.5}Sn$.

The result of the XRD and EDX measurements show that only the $Co_2Dy_{0.5}Mn_{0.5}Sn$ composition exhibits a temperature stable phase separation. In all the other composition the phase separation is vanished after the annealing step.[23]

### $\mathbf{Co_2Dy_{0.5}Mn_{0.5}Sn}$ [23]

In Fig. 52 the X-ray diffraction pattern of $Co_2Dy_{0.5}Mn_{0.5}Sn$ is shown. Almost all reflections of the XRD pattern can be indexed by the reflections of $Co_2MnSn$ (*225, $Fm\overline{3}m$*) and $Co_8Dy_3Sn_4$ (*186, $P6_3mc$*). The lattice parameter of the $Co_2MnSn$ phase is a= 5.950 Å and the lattice parameters of the $Co_8Dy_3Sn_4$ phase are a=b= 8.844 Å and c= 7.518 Å, fitting well with the literature data.[70]

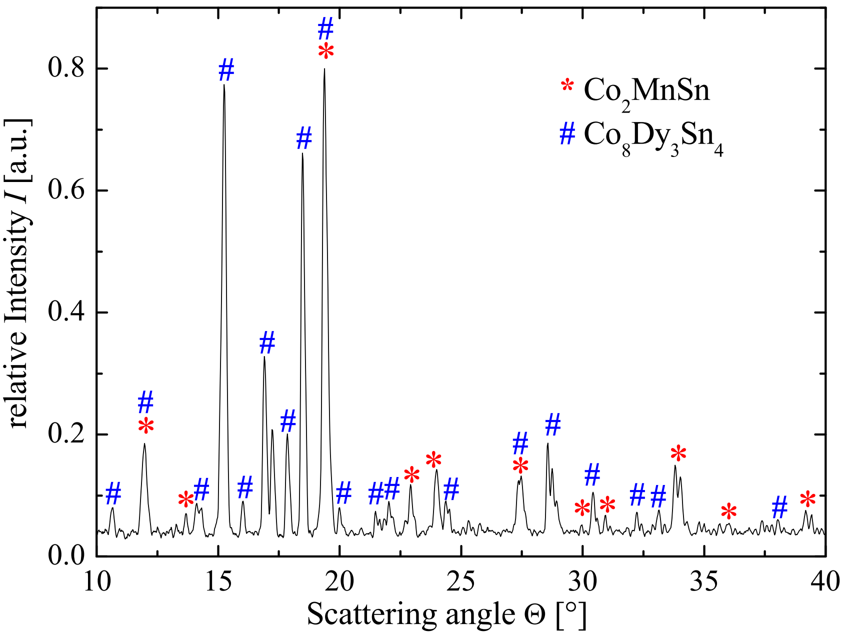

FIG. 52: XRD pattern of the phase-separated $Co_2Dy_{0.5}Mn_{0.5}Sn$ alloy.

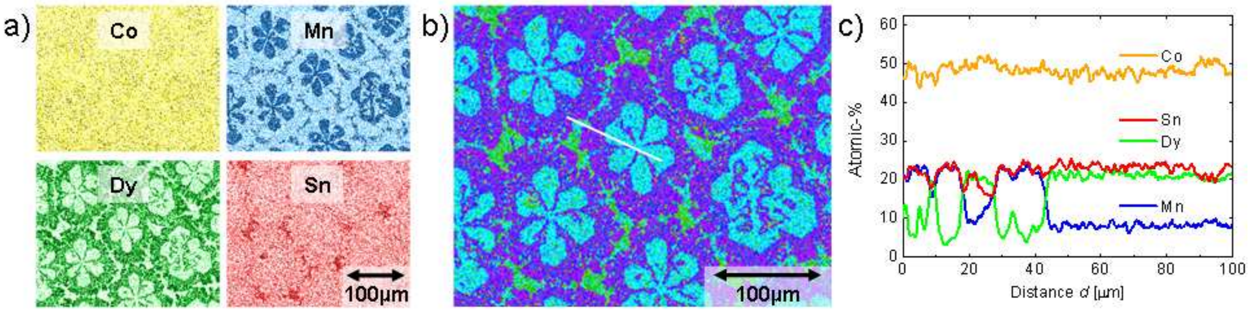

FIG. 53: a) Element-specific EDX mappings of the four constituents of the phase separated $Co_2Dy_{0.5}Mn_{0.5}Sn$ alloy with brightness proportional to the concentration. b) Linear combination of the EDX mapping shown in a) revealing three distinct regions with different compositions: region I (light blue), region II (violet), and region III (green). c) Line-scan along the path (white line) indicated in b).

Figure 53 (a) shows the distribution of elements in the phase separated $Co_2Dy_{0.5}Mn_{0.5}Sn$ compound, forming a sixfold symmetry pattern. While the Co concentration is equally distributed, the Dy forms a flower-like six-fold pattern. The Dy-rich regions have a small concentration of Mn and vice versa. Sn also shows a more or less homogeneous distribution except in small regions at the grain boundaries. A linear combination of the element-specific EDX mappings shown in Figure 53 (b), reveals three distinct phases. Region I (light blue) shows a sixfold flower pattern embedded in region II (violet). Region III (green) fills the interstitial space inbetween region II.

The EDX line-scan shown in Figure 53 (c) quantifies the stoichiometry of the three regions. Region I with composition $Co_{1.95}Dy_{0.84}Mn_{0.26}Sn_{0.95}$ has the lowest Mn concentration and forms the flower-like six-fold pattern surrounded by region II with a six-fold pattern $Co_{1.95}Dy_{0.14}Mn_{0.96}Sn_{0.95}$ structure. The compositions are formally close to the Heusler alloy $Co_xDy_xMn_{1-x}Sn$. Region III consists of an intermediate composition $Co_2Dy_{0.83}Mn_{0.45}Sn_{0.72}$. The structure in the lower left corner of Figure 53 (b) reveals an inner pattern, roughly repeating the six-fold flower-like pattern on a smaller scale. All three phases reveal inhomogeneities that could hardly be resolved by EDX. Taking into account the XRD analysis, which has identified cubic $L2_1$ ordered $Co_2MnSn$ and hexagonal $Co_8Dy_3Sn_4$ as pure constituent phases, the observed stoichiometry for region I and II may be interpreted in the following way: Region I is dominated by the $Co_8Dy_3Sn_4$ with additional inclusions of

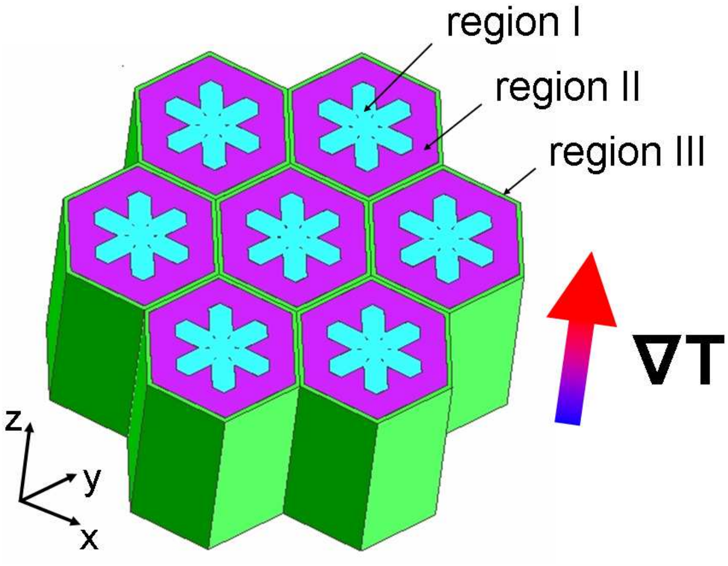

FIG. 54: Sketch of the 3-dimensional phase-separated $Co_2Dy_{0.5}Mn_{0.5}Sn$ alloy. The temperature gradient ∇T is pointing along the z direction.

$Co_2MnSn$ amounting to 20% volume fraction, and region II is dominated by $Co_2MnSn$ with an amount of 10%. The SEM and EDX measurements conducted on a surface cut parallel to the temperature gradient reveal parallel stripes of up to 1 mm length which can be clearly identified with region I, region II, and region III (see left hand side Figure 55). In contrast, EDX images of surfaces perpendicular to the temperature gradient show the flower-like structure (see Figure 53, see right hand side Figure 55). A sketch of the resulting 3-dimensional structure is shown in Figure 54.

The 3-dimensional cellular microstructure is formed by a dendritic crystal growth similar to observations for binary alloys, e.g. Pb-Sn.[71] The different melting points of $Co_2MnSn$ and $Co_8Dy_3Sn_4$ is most likely the origin of the observed cellular microstructure. $Co_8Dy_3Sn_4$, with the highest melting point, solidifies as the observed region I in the remaining liquid phase. The six-fold pattern formation in region I originates from the strong epitaxial strain imposed by the hexagonal $Co_8Dy_3Sn_4$ phase with the cubic $Co_2MnSn$ phase formed during the solidifying process.

A phase separation has also been observed for the Heusler alloys $Co_2Mn_{(1-x)}Ti_xSn$ and $CoTi_{(1-x)}Mn_xSb$.[17, 21] These alloys exhibit a separation into two Heusler phases, but they show a rather irregular structure. Moreover, the phase separation disappears after high

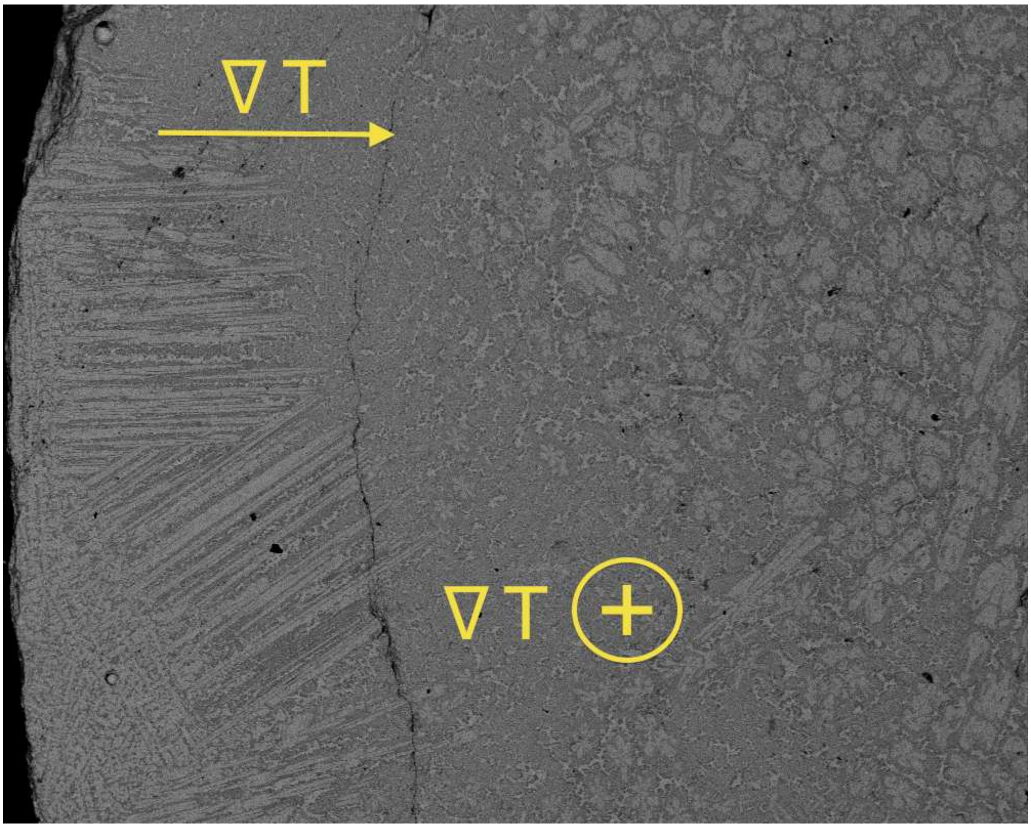

FIG. 55: SEM image of a slice of the $Co_2Dy_{0.5}Mn_{0.5}Sn$ ingot. The temperature gradient ∇T on the borders of the ingot determined the growth direction.

temperature annealing, in contrast to the compound discussed here.

Figure 56 (a) shows the magnetization as a function of the sample temperature. Two magnetic phase transitions occur at different Curie temperatures $T_{C,1}$= 95 ± 10 K and $T_{C,2}$= 830 ± 10 K. The $T_C$ values were determined by fitting the temperature dependent magnetization with $M(t) = M_0(1-T/T_C)^{1/2}$ as obtained from the mean field theory.[72] Previous measurements have shown that $Co_2MnSn$ has a Curie temperature of $T_C$= 830 K.[73] Therefore, the $T_{C,2}$ can be attributed to this phase. $T_{C,1}$ is likely the Curie temperature of $Co_8Dy_3Sn_4$. For pure $Co_8Dy_3Sn_4$ we found a Curie temperature of $T_C$= 70 ± 10 K in good agreement with $T_{C,1}$. Figure 56 (b) shows the field dependent magnetization above and below $T_{C,1}$ for the phase separated compound. At 5 K both phases are ferromagnetic, what explains the large saturation magnetization. At 300 K only $Co_2MnSn$ exhibits ferromagnetic behavior, resulting in a much smaller magnetization. The M(H) curve at 300 K reveals a coercive field of $H_{c,2}$= $9\times10^{-4}$ T. This comparatively small coercive field is within the

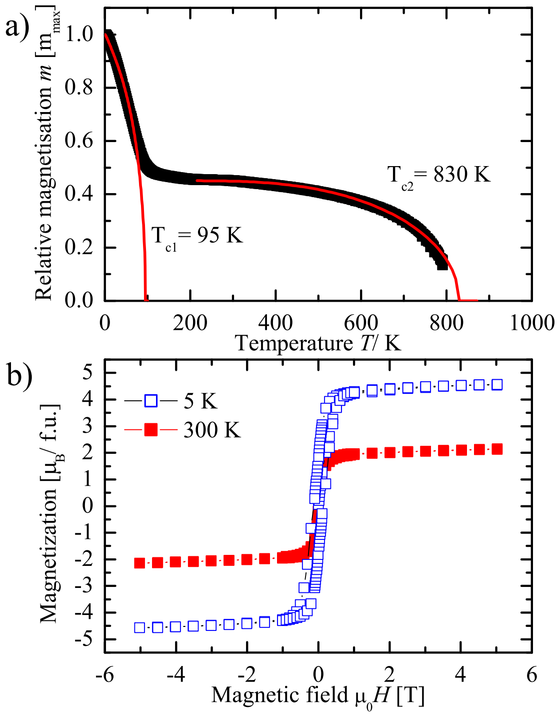

FIG. 56: a) Temperature dependent magnetization of phase separated $Co_2Dy_{0.5}Mn_{0.5}Sn$. The measurements were performed in an induction field of 1 T.

b) Field dependent magnetization at 5 K and 300 K in units of Bohr magnetons per formula unit ($\mu_B/f.u.$)

order of magnitude observed for other Co-based Heusler alloys and indicates soft magnetic behavior.[74] At 5 K, however, the coercive field $H_{c,1}$= 0.130 T is much larger due to the crystal anisotropy of the $Co_8Dy_3Sn_4$ alloy.

Figure 57 shows the thermal conductivity of the phase separated $Co_2Dy_{0.5}Mn_{0.5}Sn$ sample compared to the Heusler alloys $Co_2MnSn$ and $Co_8Dy_3Sn_4$. The electronic contribution to the thermal conductivity $\kappa_e$ was calculated using the Wiedemann-Franz Law [65] (see equation 26). With the relation from equation 25 the lattice contribution to the thermal conductivity was calculated. In comparison to $Co_2MnSn$ the electronic part of the thermal conductivity of $Co_2Dy_{0.5}Mn_{0.5}Sn$ is lower due to the slightly higher resistivity (Figure 58). The higher resistivity probably is an effect of the phase separation, because there are more grain and phase boundaries than in the $Co_2MnSn$ sample. Possibly electrons are scattered more often at these grain boundaries. The resistivity of $Co_8Dy_3Sn_4$ is slightly higher than in the mixed compound leading to a lower electronic contribution to the thermal conductivity.

The lattice thermal conductivity is about one third lower for $Co_2Dy_{0.5}Mn_{0.5}Sn$ than for $Co_2MnSn$. In comparison with $Co_8Dy_3Sn_4$ $\kappa_l$ is slightly lower than the mixed phase up to 250 K. Above 250 K the lattice thermal conductivity of $Co_8Dy_3Sn_4$ increases strongly and is about 40% higher than that of $Co_2Dy_{0.5}Mn_{0.5}Sn$. The lower $\kappa_l$ value can be explained by the phase separation, as well. The additional grain boundaries act as very efficient scattering centers for phonons and electrons, thus decreasing the thermal conductivity.

The lattice thermal conductivity is expected to show a maximum at intermediate temperatures due to a compensation of the increasing number of phonons contributing to the transport and increasing contribution from Umklapp processes causing scattering with increasing temperature. The additional scattering at grain boundaries cause a temperature independent decrease of $\kappa_l$, till the temperatures are as high that the mean free path of the phonons is shorter than the grain sizes. This expected temperature dependence of $\kappa_l(T)$ is observed at lower temperatures with the maximum located at T= 50 K. The slight increase of the lattice thermal conductivity near 300 K can be explain by a temperature dependent Lorenz number instead of a constant used in this case for the calculation of the electronic contribution to the thermal conductivity or by bipolar diffusion.[36] The lattice thermal conductivity of $Co_8Dy_3Sn_4$ shows a typical behavior of a compound with a complex unit cell in a quasicrystal or amorphous metal.[63, 64] $\kappa_i(T)$ can be divided into three intervals. In Interval I (0-75K) the thermal conductivity increases linearly. Interval II (75-150 K) covers an almost constant $\kappa_i(T)$. In Interval III (T > 150 K) $\kappa(T)$ increases with increasing temperature. Interval I is determined by an almost constant mean free path of the phonons, which is limited by grain boundaries or extrinsic defects like lattice distortions. In Interval II, the plateau, all available phonons are saturated in the Dulong-Petit limit.[64] Interval III can be explained by the interaction of high-energy critical modes with low-energy extended phonons similar to the phonon-assisted fraction hopping in glasses.[63, 64] Electrical resistivities show metallic behavior, i.e. resistivity increases with increasing temperature. The resistivity of $Co_2Dy_{0.5}Mn_{0.5}Sn$ is larger by a factor of two. As mentioned above, this probably is an effect of the phase separation. $Co_8Dy_3Sn_4$ shows a slightly higher resistivity than the mixed compound.

The Seebeck coefficient was also measured and the results show that the samples exhibit a negative Seebeck coefficient indicating n-type conduction. The Seebeck coefficient of $Co_2MnSn$ decreases above 250 K to a value of - 35 $\mu V K^{-1}$ at 400 K. The Seebeck coef-

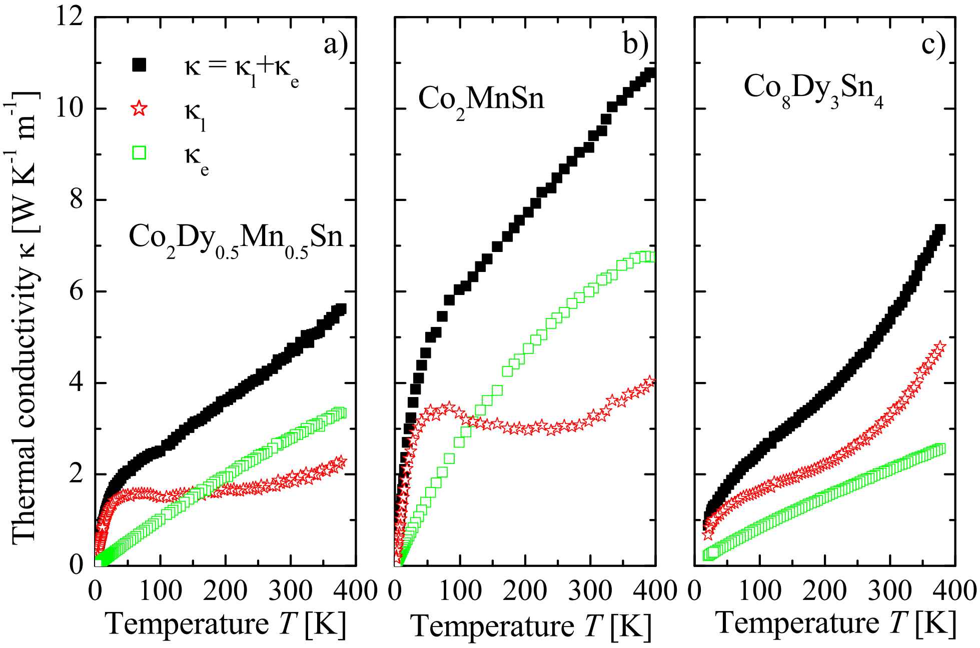

FIG. 57: Temperature dependent thermal conductivity of a) $Co_2Dy_{0.5}Mn_{0.5}Sn$, b) $Co_2MnSn$ and c) $Co_8Dy_3Sn_4$. Shown are the thermal conductivity, the lattice thermal conductivity and the electronic contribution to the thermal conductivity, calculated using the Wiedemann-Franz law.

ficient of $Co_2Dy_{0.5}Mn_{0.5}Sn$ decreases linearly with the temperature in the total measured temperature range between 2 K to 400 K. Similar behavior is seen for $Co_8Dy_3Sn_4$. The electronic properties of the mixed compound $Co_2Dy_{0.5}Mn_{0.5}Sn$ seem to be dominated by the electronic properties of $Co_8Dy_3Sn_4$.

In summary, it has been shown that grain boundaries between structurally different grains can reduce the lattice thermal conductivity $\kappa_l$ significantly. The lattice thermal conductivity of $Co_2Dy_{0.5}Mn_{0.5}Sn$ is lower than the mean value of the $\kappa_l$ of the constituent phases. This is a consequence of the phase separation, which is temperature-stable over a wide temperature range. The temperature dependence of the magnetization reflects the phase separation into two main phases. In contrast, the magnetization curve indicates a homogeneous magnetization rotation with a large coercive field dominated by the $Co_8Dy_3Sn_4$ phase at low temperature. The Seebeck effect and the electronic resistivity in the phase separated compound are dominated by the $Co_8Dy_3Sn_4$ phase. The results of this study show that the obstacle of a large lattice thermal conductivity commonly observed for Heusler compounds can be over-

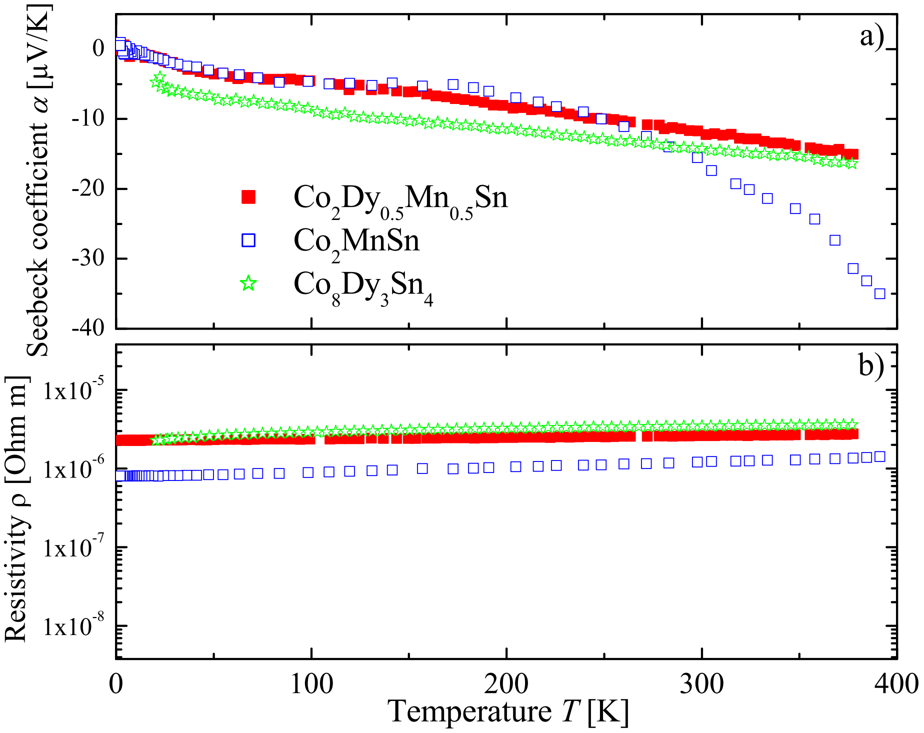

FIG. 58: Seebeck coefficient(a) and electrical resistivity (b) for $Co_2Dy_{0.5}Mn_{0.5}Sn$, $Co_2MnSn$ and $Co_8Dy_3Sn_4$.

come by a temperature-stable phase separation. Further improvements are expected from an increase of the Seebeck coefficient by optimization of the carrier concentration through hole or electron doping.

The best four reported Figure of Merits for Heusler compounds in the field of thermoelectricity derive from the $\mathrm{Ti}_x\mathrm{Zr}_y\mathrm{Hf}_z\mathrm{NiSn}$ system (see Figure 59). The idea of this work was to investigate why this $\mathrm{Ti}_x\mathrm{Zr}_y\mathrm{Hf}_z\mathrm{NiSn}$ system exhibits such promising properties and what could be possible reasons for this.
For a better readability the weighted samples are named as $\mathrm{Ti}_x\mathrm{Zr}_y\mathrm{Hf}_z\mathrm{NiSn}$ and the detected phases are named as $\mathrm{Ti}_x\mathrm{Zr}_y\mathrm{Hf}_z\mathrm{NiSn}$(*roman numerals*).

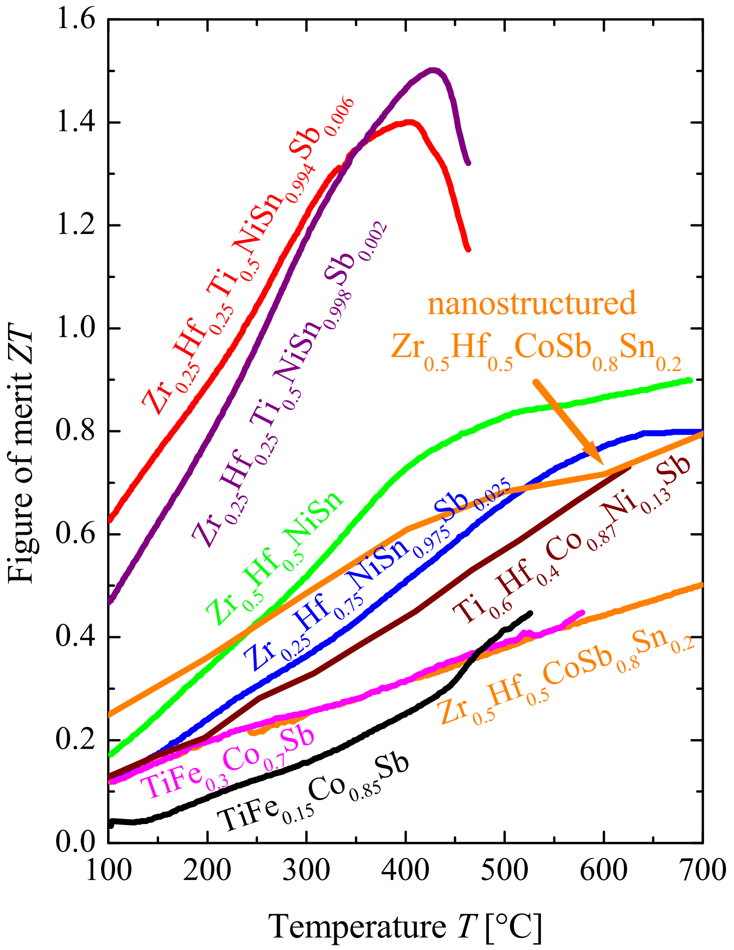

FIG. 59: State of the art of thermoelectric used Heusler compounds with $C1_b$ structure.[75–82]

### $\mathbf{Zr_{(1-x)}Hf_xNiSn}$

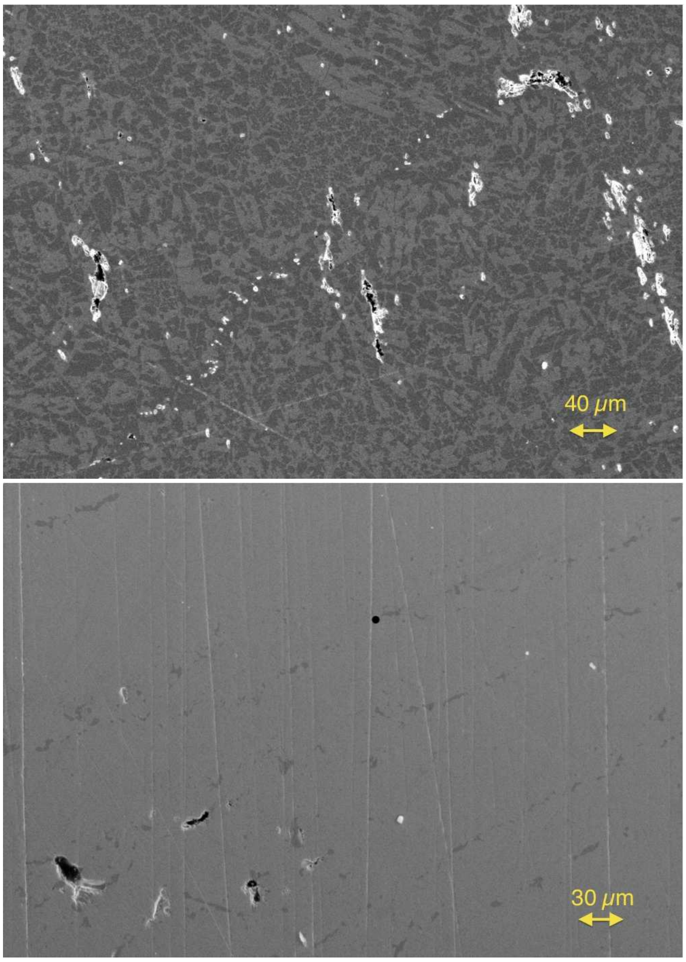

FIG. 60: Scanning electron microscope images of $Zr_{0.2}Hf_{0.8}NiSn$ (top) and $Zr_{0.05}Hf_{0.95}NiSn$ (bottom).

To reduce the number of parameters for the investigation the Ti was ignored and the $Zr_{(1-x)}Hf_xNiSn$ series was produced. The lattice parameters $a$ and the phase compositions are shown in Table II. The obtained lattice parameters, achieved by multiple phase fit, indicate a dependence on the Hf concentration, but through comparison of the detected phases by EDX, just five different $C1_b$ phases were found. Beside the parent phases ZrNiSn and HfNiSn, the phases with average compositions of $Zr_{0.78}Hf_{0.22}NiSn$(XII), $Zr_{0.55}Hf_{0.45}NiSn$(XIII) and $Zr_{0.37}Hf_{0.63}NiSn$(XIV) are detected. This indicates that the $Zr_{(1-x)}Hf_xNiSn$ series is not a solid solution and that just a few compositions of $Zr_{(1-x)}Hf_xNiSn$ are stable at the temperature of 950°C. Two examples of SEM images of a phase separated and an almost clean sample are shown in Figure 60. The contrast is produced due to the different work function of the electrons in the different phases. With EDX point and line scans it is possible to measure the composition of the phases. In Figure 61 the produced compositions (blue) and the detected phases (red) are indicated in the Gibbs triangle for the $Ti_xZr_yHf_zNiSn$ system. It is remarkable that the coexistence of two Heusler $C1_b$ phases in one compound were not able to be resolved by standard XRD measurements.

| Weighed composition $Zr_{(1-x)}Hf_xNiSn$ | Detected phases | Ratio | a [Å] |
|---|---|---|---|
| ZrNiSn | ZrNiSn, Sn | 97% ZrNiSn | 6.121(5) |
| $Zr_{0.95}Hf_{0.05}NiSn$ | ZrNiSn, Hf | inclusions | 6.114(5) |
| $Zr_{0.9}Hf_{0.1}NiSn$ | ZrNiSn, Hf | inclusions | 6.114(5) |
| $Zr_{0.8}Hf_{0.2}NiSn$ | $Zr_{0.85}Hf_{0.15}NiSn$(XII), $Sn_3Zr_5$, $Hf_2Ni_2Sn$ | 95% (XII) | 6.112(5) |
| $Zr_{0.7}Hf_{0.3}NiSn$ | $Zr_{0.6}Hf_{0.4}NiSn$(XIII), $Zr_{0.75}Hf_{0.25}NiSn$(XII) | $\frac{90\%(XIII)}{10\%(XII)}$ | 6.105(5) |
| $Zr_{0.6}Hf_{0.4}NiSn$ | $Zr_{0.58}Hf_{0.42}NiSn$(XIII), $ZrSn_2$ | 95% (XIII) | 6.101(5) |
| $Zr_{0.5}Hf_{0.5}NiSn$ | $Zr_{0.49}Hf_{0.51}NiSn$(XIII) | 95% (XIII) | 6.101(5) |
| $Zr_{0.4}Hf_{0.6}NiSn$ | $Zr_{0.36}Hf_{0.64}NiSn$(XIV), $Ni_3Sn_4$ | 50% (XIV) | 6.098(5) |
| $Zr_{0.3}Hf_{0.7}NiSn$ | $Zr_{0.29}Hf_{0.71}NiSn$(XIV), $ZrSn_2$ | 95% (XIV) | 6.094(5) |
| $Zr_{0.2}Hf_{0.8}NiSn$ | HfNiSn, $Zr_5Sn_3$ | 90% HfNiSn | 6.092(5) |
| $Zr_{0.1}Hf_{0.9}NiSn$ | HfNiSn, Zr | inclusions | 6.091(5) |
| $Zr_{0.05}Hf_{0.95}NiSn$ | HfNiSn, Zr | inclusions | 6.091(5) |
| HfNiSn | HfNiSn | 97% HfNiSn | 6.091(5) |

TABLE II: The phase compositions of the different $Zr_{(1-x)}Hf_xNiSn$ samples and the parent samples.

In Figures 62-65, the measured physical properties of the $Zr_{(1-x)}Hf_xNiSn$ series are compared with the parent ZrNiSn and HfNiSn. All obtained values of the Seebeck coefficient (see Figure 62) for the $Zr_{(1-x)}Hf_xNiSn$ series show a negative value, which indicates n-type conduction. The first impression of the different developments is that there is no dependence inbetween the measurements, but if the values of the Seebeck coefficient are set in relation to the detected stable phases (see Table II or Figure 61 ) a clear trend is recognizable. All samples which are consisting of only one phase, meaning that they exhibit almost

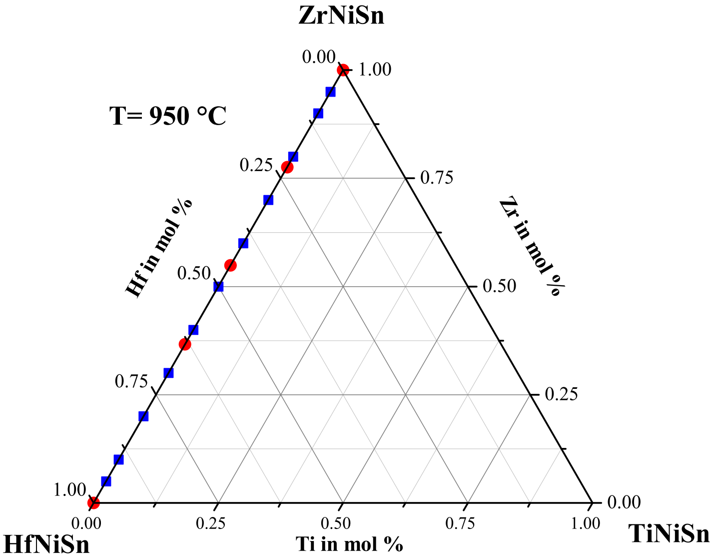

FIG. 61: The $Zr_{(1-x)}Hf_xNiSn$ series with the detected phases indicated in the Gibbs triangle.

| Stable compositions |
|---|
| ZrNiSn |
| $Zr_{0.85}Hf_{0.15}NiSn$(XII) |
| $Zr_{0.49}Hf_{0.51}NiSn$(XIII) |
| $Zr_{0.36}Hf_{0.64}NiSn$(XIV) |
| HfNiSn |

TABLE III: Compositions of the stable Heusler phases with an error range of 3%.

the stable composition, have high values for the Seebeck coefficient (ZrNiSn, $Zr_{0.1}Hf_{0.9}NiSn$, $Zr_{0.5}Hf_{0.5}NiSn$, $Zr_{0.9}Hf_{0.1}NiSn$, $Zr_{0.95}Hf_{0.05}NiSn$, HfNiSn). This is not unexpected because for high values of the Seebeck coefficient a good crystalline structure is needed, meaning that no shortcut by impurity phases exists. Structural stress, disorder or impurities would increase the number of states next to the conduction band and would decrease the gap to the conduction band by broadening of the localized states. This would decrease the values of the Seebeck coefficient and would decrease the resistivity. In Figure 63 this can be seen in the resistivity values. The resistivity of the different $Zr_{(1-x)}Hf_xNiSn$ samples follows the same trend as the values of the Seebeck coefficient. Except sample $Zr_{0.5}Hf_{0.5}NiSn$ all samples

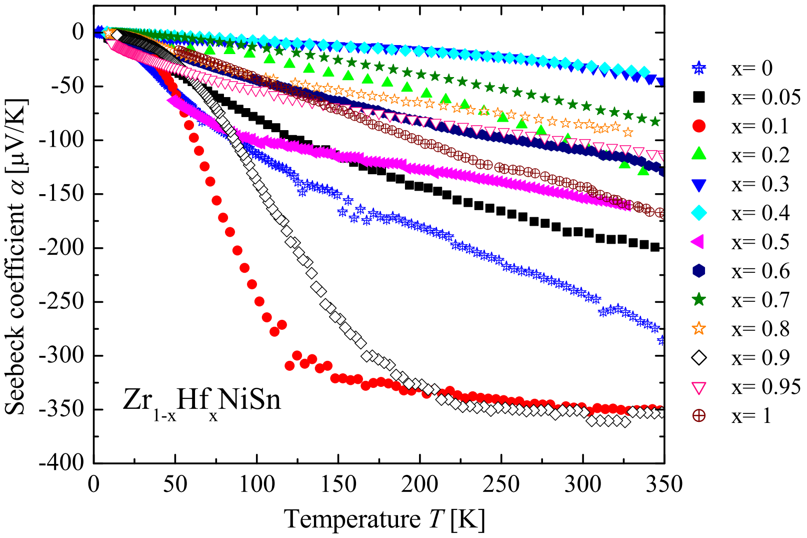

FIG. 62: Seebeck coefficient of the $Zr_{(1-x)}Hf_xNiSn$ series in comparison to the parent compounds.

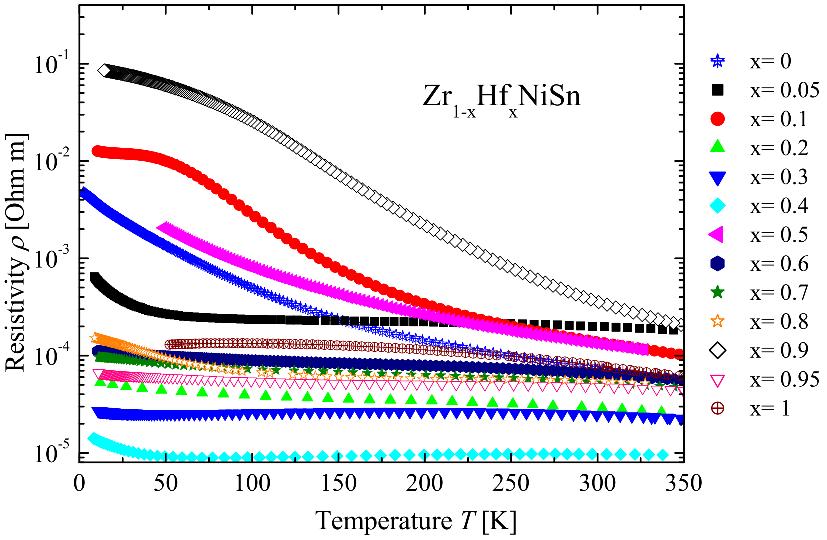

FIG. 63: Electrical resistivity of the $Zr_{(1-x)}Hf_xNiSn$ series in comparison to the parent compounds.

with high values of the Seebeck coefficient exhibit a high lattice thermal conductivity due to the good crystallinity and the low impurities (see Figure 67). Although the samples with more phases exhibit low values for the resistivity, meaning that the electronic contribution to the thermal conductivity $\kappa_e$ is high (see Figure 66), the thermal conductivity $\kappa$ is low. This is the effect of the phase separation, which causes additional phonon scattering at the

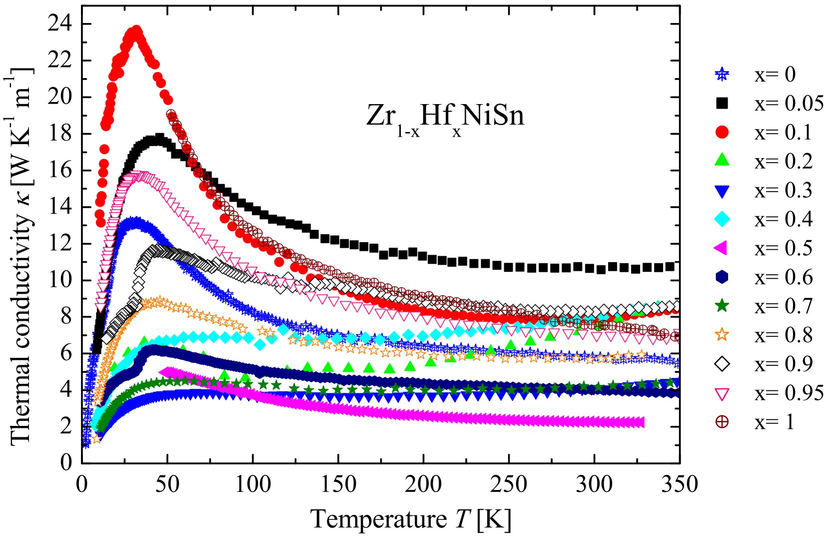

FIG. 64: Thermal conductivity of the $Zr_{(1-x)}Hf_xNiSn$ series in comparison to the parent compounds.

grain and phase boundaries. The lowest value is achieved by the stable phase $Zr_{0.5}Hf_{0.5}NiSn$ with a value of $\kappa = 2.2\frac{W}{Km}$. The sample with a phase decomposition $Zr_{0.7}Hf_{0.3}NiSn$ exhibits a low value for the thermal conductivity, too. The samples with a phase segregation, meaning with at least two phases with different crystal structures coexisting, also have low values for the thermal conductivity and they show the typical behavior of a compound with a complex unit cell in a quasicrystal or amorphous metal.[63, 64] In Figure 68 the dependence of the lattice thermal conductivity on the hafnium concentration is shown. For a solid solution the maximum values should be the parent phases and the minimum value should be exact at a concentration of 0.5 Hf.[36] The lowest values are achieved for phase separated samples and for the 0.5 Hf sample. The other values do not show a real trend, because this system is not a solid solution and samples with segregations are obtained. Figure 65 shows the temperature dependence of the Figure of Merit. Due to the high values of the Seebeck coefficient the samples with almost one phase and the parent phases show the highest values for the Figure of Merit (see Table IV and Table II).

| Composition<br>$Zr_{(1-x)}Hf_xNiSn$ | Seebeck coefficient<br>$\alpha$ $[\frac{\mu V}{K}]$ | Resistivity<br>$\rho$ [Ohm m] | Thermal conductivity<br>$\kappa$ $[\frac{W}{Km}]$ | Figure of Merit<br>$ZT$ |
|---|---|---|---|---|
| ZrNiSn | -241 | $7.4{\cdot}10^{-5}$ | 5.8 | 0.040 |
| $Zr_{0.95}Hf_{0.05}NiSn$ | -184 | $2.0{\cdot}10^{-4}$ | 10.7 | 0.005 |
| $Zr_{0.9}Hf_{0.1}NiSn$ | -347 | $1.4{\cdot}10^{-4}$ | 7.9 | 0.033 |
| $Zr_{0.8}Hf_{0.2}NiSn$ | -106 | $2.9{\cdot}10^{-5}$ | 7.5 | 0.016 |
| $Zr_{0.7}Hf_{0.3}NiSn$ | -31 | $2.5{\cdot}10^{-5}$ | 4.1 | 0.003 |
| $Zr_{0.6}Hf_{0.4}NiSn$ | -29 | $9.7{\cdot}10^{-6}$ | 7.9 | 0.004 |
| $Zr_{0.5}Hf_{0.5}NiSn$ | -154 | $1.3{\cdot}10^{-4}$ | 2.2 | 0.014 |
| $Zr_{0.4}Hf_{0.6}NiSn$ | -109 | $6.5{\cdot}10^{-5}$ | 4.1 | 0.014 |
| $Zr_{0.3}Hf_{0.7}NiSn$ | -68 | $5.3{\cdot}10^{-5}$ | 4.2 | 0.007 |
| $Zr_{0.2}Hf_{0.8}NiSn$ | -85 | $5.5{\cdot}10^{-5}$ | 5.7 | 0.007 |
| $Zr_{0.1}Hf_{0.9}NiSn$ | -352 | $3.6{\cdot}10^{-4}$ | 8.3 | 0.013 |
| $Zr_{0.05}Hf_{0.95}NiSn$ | -102 | $4.8{\cdot}10^{-5}$ | 7.0 | 0.009 |
| HfNiSn | -142 | $8.0{\cdot}10^{-5}$ | 7.6 | 0.010 |

TABLE IV: Physical properties of the $Zr_{(1-x)}Hf_xNiSn$ series in comparison to the parent compounds at 300 K.

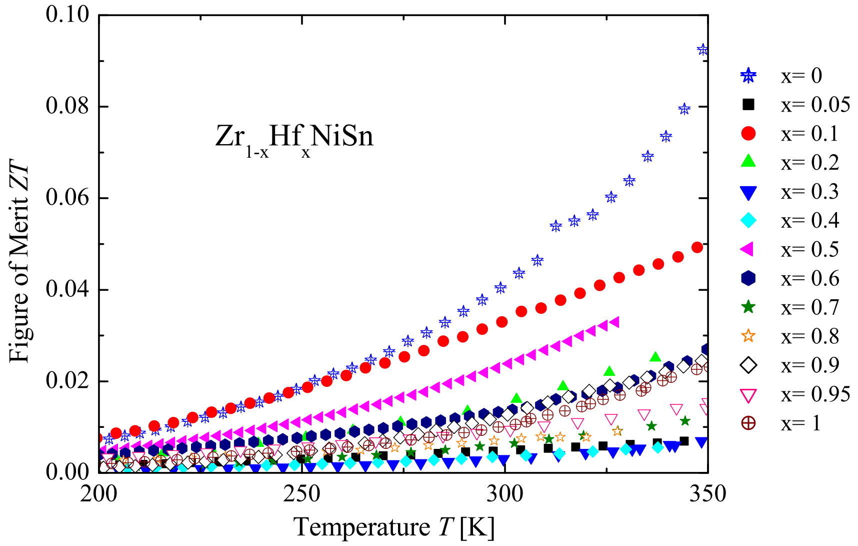

FIG. 65: Figure of Merit of the $Zr_{(1-x)}Hf_xNiSn$ series in comparison to the parent compounds.

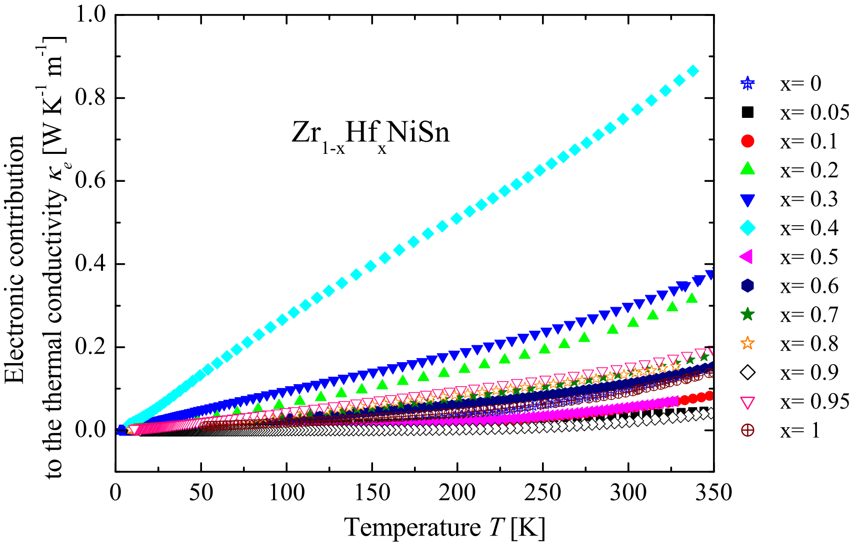

FIG. 66: Temperature dependence of the electronic contribution to the thermal conductivity of the $Zr_{(1-x)}Hf_xNiSn$ series in comparison to the parent compounds.

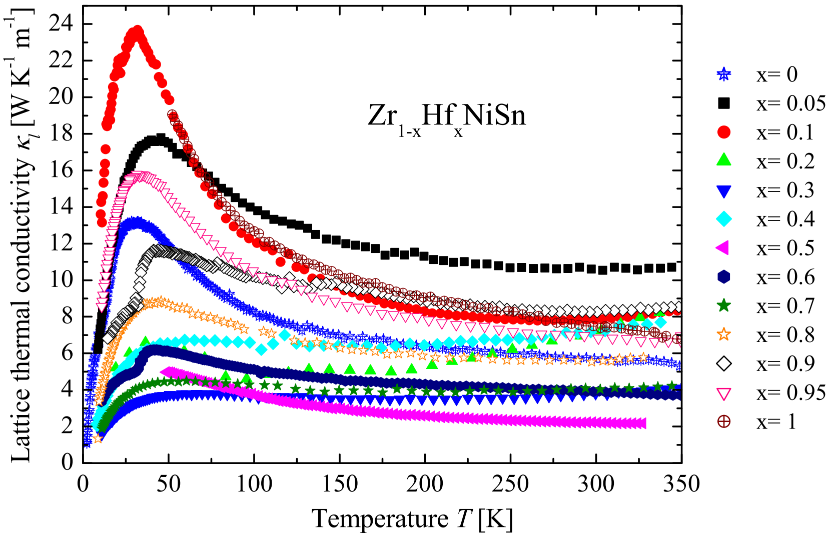

FIG. 67: Temperature dependence of the lattice thermal conductivity of the $Zr_{(1-x)}Hf_xNiSn$ series in comparison to the parent compounds.

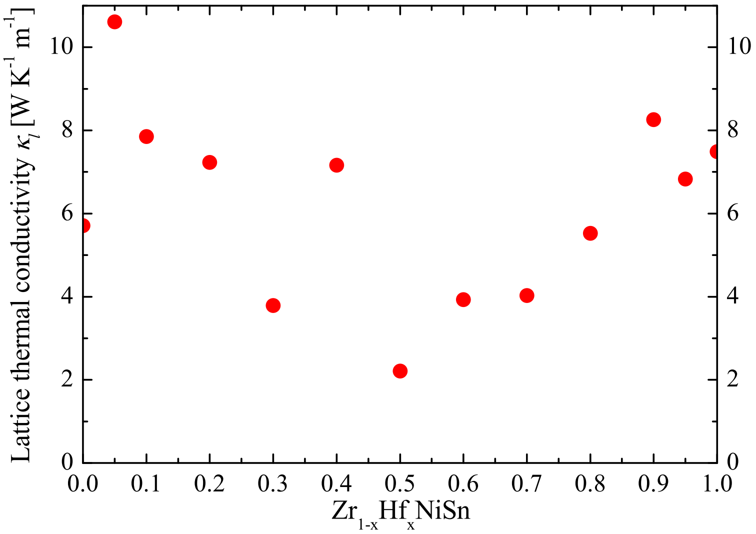

FIG. 68: Lattice thermal conductivity at 300 K of the Zr$_{(1-x)}$Hf$_x$NiSn series in dependence on the hafnium concentration $x$.

### $\mathbf{Ti_{(1-x)}Zr_xNiSn}$

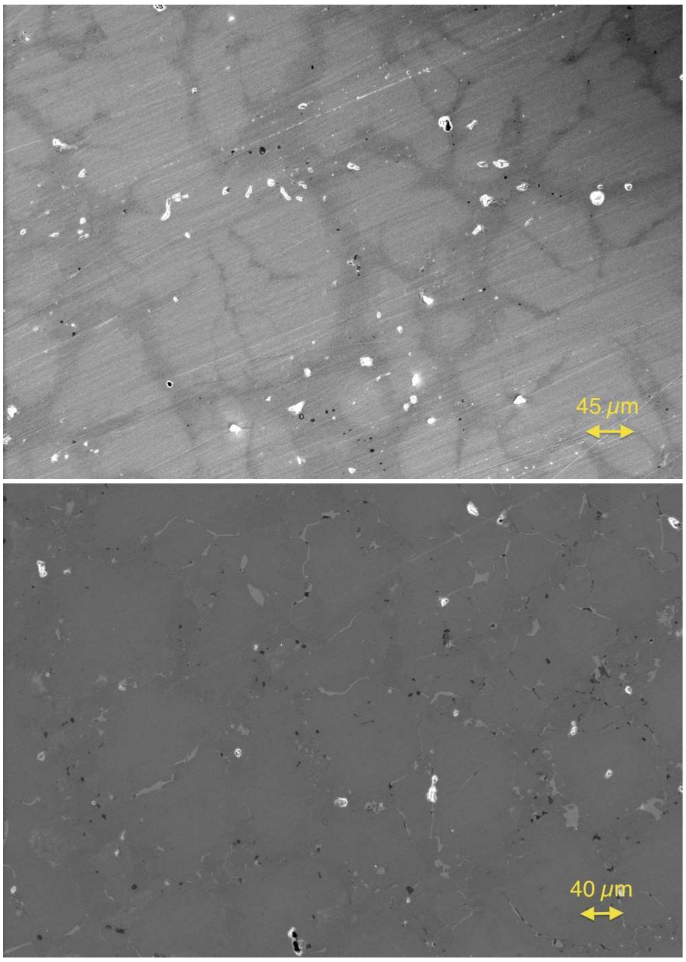

FIG. 69: Scanning electron microscope images of $Ti_{0.4}Zr_{0.6}NiSn$ (top) and $Ti_{0.6}Zr_{0.4}NiSn$ (bottom).

After the investigation of the Zr/Hf system the Hf was ignored and the $Ti_{(1-x)}Zr_xNiSn$ series was investigated to prove that this series is no solid solution, either. The lattice parameters $a$ and the phase compositions are shown in Figure V. A slight trend is recognizable in the obtained lattice parameters showing a dependence of the Zr concentration. The comparison of the detected phases again leads to just five different $C1_b$ phases. In addition to the parent phases ZrNiSn and TiNiSn, the phases $Ti_{0.82}Zr_{0.18}NiSn$(IX), $Ti_{0.65}Zr_{0.35}NiSn$(X) and $Ti_{0.31}Zr_{0.69}NiSn$(XI) were found. The analogy to the detected phases of the $Zr_{(1-x)}Hf_xNiSn$ series is remarkable and shows that the series are chemically related. This result is not unexpected because the properties of Ti, Zr and Hf are related. Two examples of SEM images of a phase separated and an almost clean sample are shown in Figure 69. In Figure 70 the produced compositions (dark blue) and the detected phases (red) are indicated in the Gibbs triangle for the $\mathrm{Ti}_x\mathrm{Zr}_y\mathrm{Hf}_z\mathrm{NiSn}$ system. These results also lead to the conclusion that the $\mathrm{Ti}_{(1-x)}\mathrm{Zr}_x\mathrm{NiSn}$ series is no solid solution, either.

| Weighed composition $\mathrm{Ti}_{(1-x)}\mathrm{Zr}_x\mathrm{NiSn}$ | Detected phases | Ratio | a [Å] |
|---|---|---|---|
| TiNiSn | TiNiSn, $\mathrm{Ni_2TiSn}$, $\mathrm{Ti_6Sn_5}$, Sn | 85% TiNiSn | 5.939(5) |
| $\mathrm{Ti_{0.95}Zr_{0.05}NiSn}$ | TiNiSn, $\mathrm{Ni_2TiSn}$, $\mathrm{Ti_6Sn_5}$, Zr | 85% TiNiSn | 5.961(5) |
| $\mathrm{Ti_{0.9}Zr_{0.1}NiSn}$ | TiNiSn, $\mathrm{Ni_2TiSn}$, Zr | 90% TiNiSn | 5.960(5) |
| $\mathrm{Ti_{0.8}Zr_{0.2}NiSn}$ | $\mathrm{Ti_{0.80}Zr_{0.19}NiSn}$(IX), $\mathrm{Ti_6Sn_5}$ | 95% (IX) | 5.966(5) |
| $\mathrm{Ti_{0.7}Zr_{0.3}NiSn}$ | $\mathrm{Ti_{0.78}Zr_{0.12}NiSn}$(IX), $\mathrm{Ni_3Sn_4}$ | 60%(IX) | 6.001(5) |
| $\mathrm{Ti_{0.6}Zr_{0.4}NiSn}$ | $\mathrm{Ti_{0.62}Zr_{0.38}NiSn}$(X), $\mathrm{ZrSn_2}$ | 90% (X) | 6.086(5) |
| $\mathrm{Ti_{0.5}Zr_{0.5}NiSn}$ | $\mathrm{Ti_{0.74}Zr_{0.26}NiSn}$(IX), $\mathrm{Ti_{0.36}Zr_{0.64}NiSn}$(XI) | $\frac{50\%(IX)}{50\%(XI)}$ | 6.005(5)/6.067(5) |
| $\mathrm{Ti_{0.4}Zr_{0.6}NiSn}$ | $\mathrm{Ti_{0.66}Zr_{0.34}NiSn}$(X), $\mathrm{Ti_{0.23}Zr_{0.77}NiSn}$(XI) | $\frac{40\%(X)}{60\%(XI)}$ | 6.075(5) |
| $\mathrm{Ti_{0.3}Zr_{0.7}NiSn}$ | $\mathrm{Ti_{0.29}Zr_{0.71}NiSn}$(XI) | 97% (XI) | 6.204(5) |
| $\mathrm{Ti_{0.2}Zr_{0.8}NiSn}$ | ZrNiSn, $\mathrm{Ti_6Sn_5}$, Zr | 90% ZrNiSn | 6.101(5) |
| $\mathrm{Ti_{0.1}Zr_{0.9}NiSn}$ | ZrNiSn,$\mathrm{Ti_6Sn_5}$ | 95% ZrNiSn | 6.101(5) |
| $\mathrm{Ti_{0.05}Zr_{0.95}NiSn}$ | ZrNiSn, Ti | 95% ZrNiSn | 6.108(5) |
| ZrNiSn | ZrNiSn, Sn | 97% ZrNiSn | 6.121(5) |

TABLE V: The phase compositions of the different $\mathrm{Ti}_{(1-x)}\mathrm{Zr}_x\mathrm{NiSn}$ samples and the parent samples.

| Stable compositions |
|---|
| TiNiSn |
| $\mathrm{Ti_{0.80}Zr_{0.19}NiSn}$(IX) |
| $\mathrm{Ti_{0.66}Zr_{0.34}NiSn}$(X) |
| $\mathrm{Ti_{0.29}Zr_{0.71}NiSn}$(XI) |
| ZrNiSn |

TABLE VI: Compositions of the stable Heusler phases with an error range of 3%.

In Figures 71-74, the measured physical properties of the $\mathrm{Ti}_{(1-x)}\mathrm{Zr}_x\mathrm{NiSn}$ series are compared.

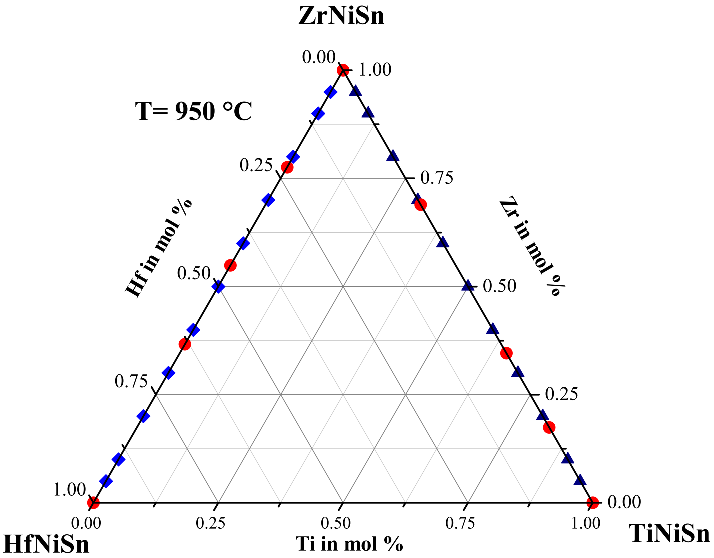

FIG. 70: The $Ti_{(1-x)}Zr_xNiSn$ series with the detected phases indicated in the Gibbs triangle.

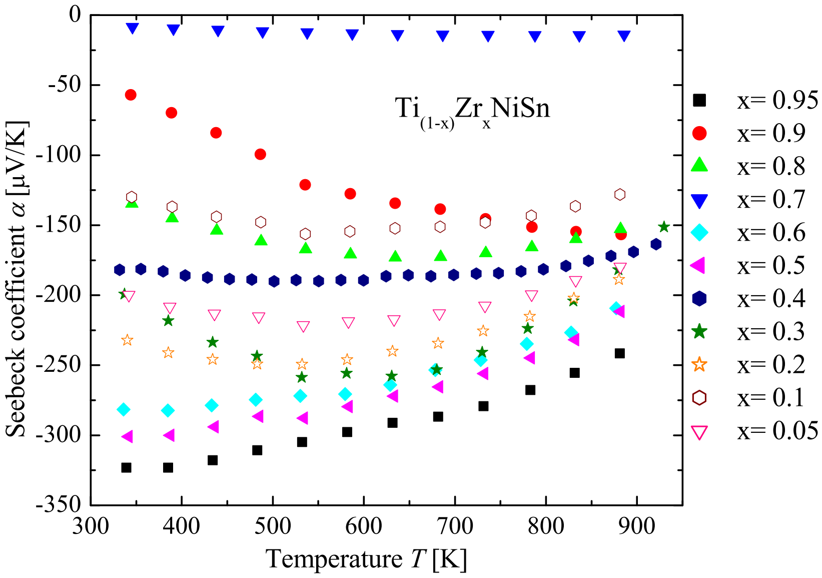

FIG. 71: Seebeck coefficient of the $Ti_{(1-x)}Zr_xNiSn$ series in comparison to the parent compounds.

All samples of the $Ti_{(1-x)}Zr_xNiSn$ series exhibit n-type conduction indicated by the negative values of the Seebeck coefficient (see Figure 71). Again the values of the Seebeck coefficient of the $Ti_{(1-x)}Zr_xNiSn$ series seem to show no dependence on the composition. High val-

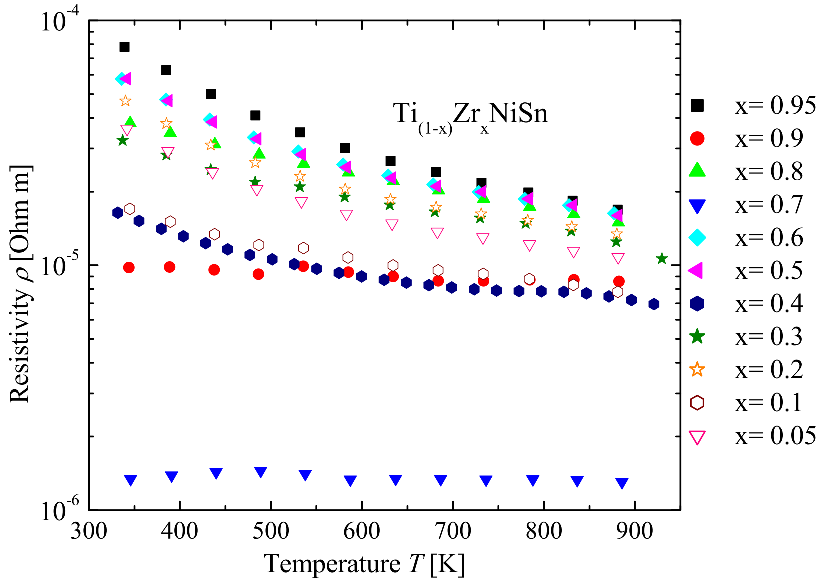

FIG. 72: Electrical resistivity of the $\mathrm{Ti}_{(1-x)}\mathrm{Zr}_x\mathrm{NiSn}$ series in comparison to the parent compounds.

ues of the Seebeck coefficient are obtained for $\mathrm{Ti}_{0.05}\mathrm{Zr}_{0.95}\mathrm{NiSn}$, $\mathrm{Ti}_{0.3}\mathrm{Zr}_{0.7}\mathrm{NiSn}$, $\mathrm{Ti}_{0.4}\mathrm{Zr}_{0.6}\mathrm{NiSn}$, $\mathrm{Ti}_{0.5}\mathrm{Zr}_{0.5}\mathrm{NiSn}$ and $\mathrm{Ti}_{0.8}\mathrm{Zr}_{0.2}\mathrm{NiSn}$. In comparison to the detected stable phases (see Table V or Figure 70) just samples with one Heusler phase with $C1_b$ structure or a decomposition of two Heusler phases with $C1_b$ structure exhibit the high values of the Seebeck coefficient. This shows that a good crystalline structure and low impurities are needed. But also decomposition of two clean Heusler phases with $C1_b$ structure can lead to high values of the Seebeck coefficient. The values of the resistivity support this observation (see Figure 72) and have the same dependence as the values of the Seebeck coefficient. In contrast to the results of the $\mathrm{Zr}_{(1-x)}\mathrm{Hf}_x\mathrm{NiSn}$ series, the $\mathrm{Ti}_{(1-x)}\mathrm{Zr}_x\mathrm{NiSn}$ samples with high values of the Seebeck coefficient show moderate values of the thermal conductivity. The lattice thermal conductivity (see Figure 76) of this samples is dominated by the crystallinity of the samples. This is recognizable in the values of the resistivity, which are high in the samples with clean $C1_b$ structure and leads to a low contribution to the electronic thermal conductivity $\kappa_e$ (see Figure 75) in comparison to the other samples of the $\mathrm{Ti}_{(1-x)}\mathrm{Zr}_x\mathrm{NiSn}$ series. In Figure 77 the dependence of the lattice thermal conductivity on the zirconium concentration is shown and no behavior of a solid solution is recognizable. The samples with one phase or a high crystallinity exhibit the highest values for the lattice thermal conductivity. This is explainable by the lower disorder, strain and impurities in these samples. The slight increase of the lattice thermal conductivity is due to bipolar contributions to the conduction.[36] In Figure 74 the temperature dependence of the Figure of Merit is shown. The samples with high values of the Seebeck coefficient show high values for the Figure of Merit (see Table VII). But also the samples with moderate values of the Seebeck coefficient and a lower resistivity in comparison to the samples with clean $C1_b$ structure show high values for the Figure of Merit. This is due to the high impact of the resistivity on the Figure of Merit.

| Composition<br>$Ti_{(1-x)}Zr_xNiSn$ | Seebeck coefficient<br>$\alpha$ [$\frac{\mu V}{K}$] | Resistivity<br>$\rho$ [Ohm m] | Thermal conductivity<br>$\kappa$ [$\frac{W}{Km}$] | Figure of Merit<br>$ZT$ |
|---|---|---|---|---|
| ZrNiSn | -286 | $5.6\cdot10^{-5}$ | 5.5 | 0.093 |
| $Ti_{0.05}Zr_{0.95}NiSn$ | -323 | $7.8\cdot10^{-5}$ | 4.9 | 0.092 |
| $Ti_{0.1}Zr_{0.9}NiSn$ | -57 | $9.8\cdot10^{-6}$ | 9.4 | 0.012 |
| $Ti_{0.2}Zr_{0.8}NiSn$ | -135 | $3.8\cdot10^{-5}$ | 7.1 | 0.023 |
| $Ti_{0.3}Zr_{0.7}NiSn$ | -8 | $1.3\cdot10^{-6}$ | 34.8 | 0.001 |
| $Ti_{0.4}Zr_{0.6}NiSn$ | -281 | $5.8\cdot10^{-5}$ | 5.8 | 0.080 |
| $Ti_{0.5}Zr_{0.5}NiSn$ | -301 | $5.8\cdot10^{-5}$ | 3.4 | 0.218 |
| $Ti_{0.6}Zr_{0.4}NiSn$ | -182 | $1.6\cdot10^{-5}$ | 2.5 | 0.271 |
| $Ti_{0.7}Zr_{0.3}NiSn$ | -199 | $3.2\cdot10^{-5}$ | 26.1 | 0.025 |
| $Ti_{0.8}Zr_{0.2}NiSn$ | -232 | $4.7\cdot10^{-5}$ | 15.1 | 0.039 |
| $Ti_{0.9}Zr_{0.1}NiSn$ | -130 | $1.7\cdot10^{-5}$ | 4.2 | 0.115 |
| $Ti_{0.95}Zr_{0.05}NiSn$ | -200 | $3.6\cdot10^{-5}$ | 4.8 | 0.079 |
| TiNiSn | -117 | $2.8\cdot10^{-5}$ | 8.4 | 0.014 |

TABLE VII: Physical properties of the $Ti_{(1-x)}Zr_xNiSn$ series in comparison to the parent compounds at 350 K.

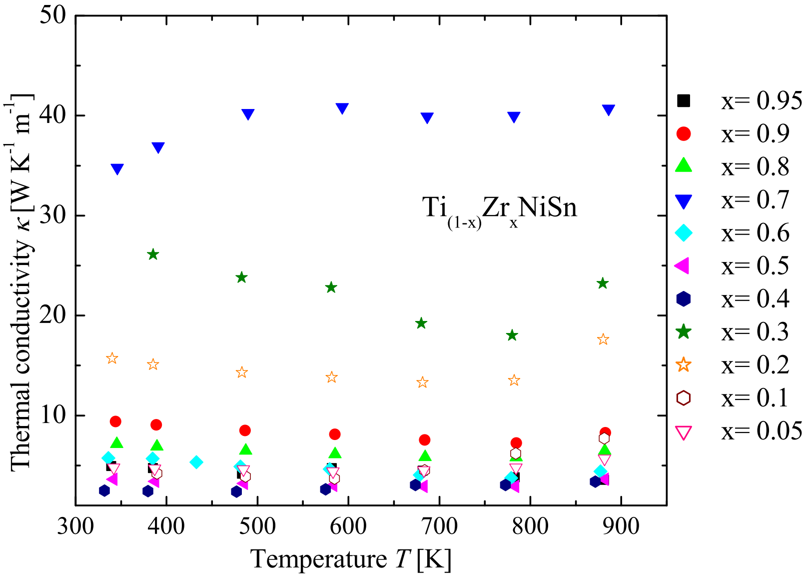

FIG. 73: Thermal conductivity of the $Ti_{(1-x)}Zr_xNiSn$ series in comparison to the parent compounds.

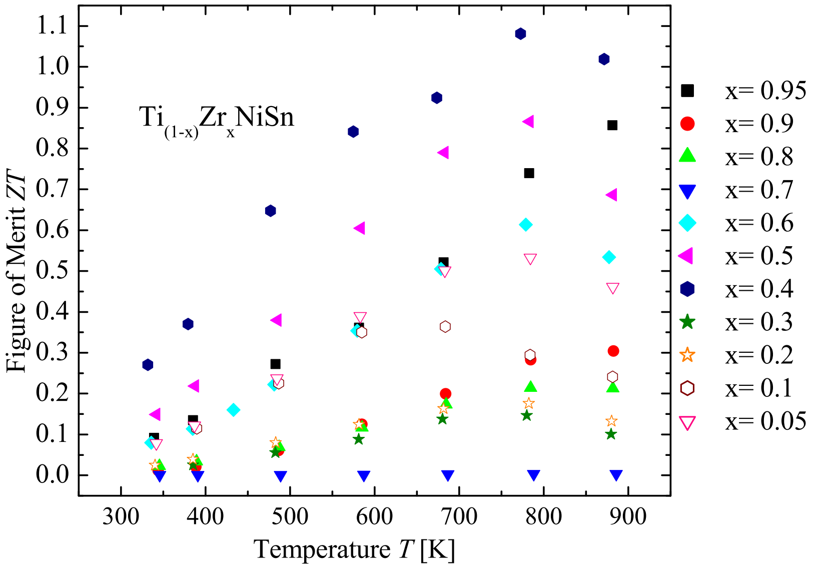

FIG. 74: Figure of Merit of the $Ti_{(1-x)}Zr_xNiSn$ series in comparison to the parent compounds.

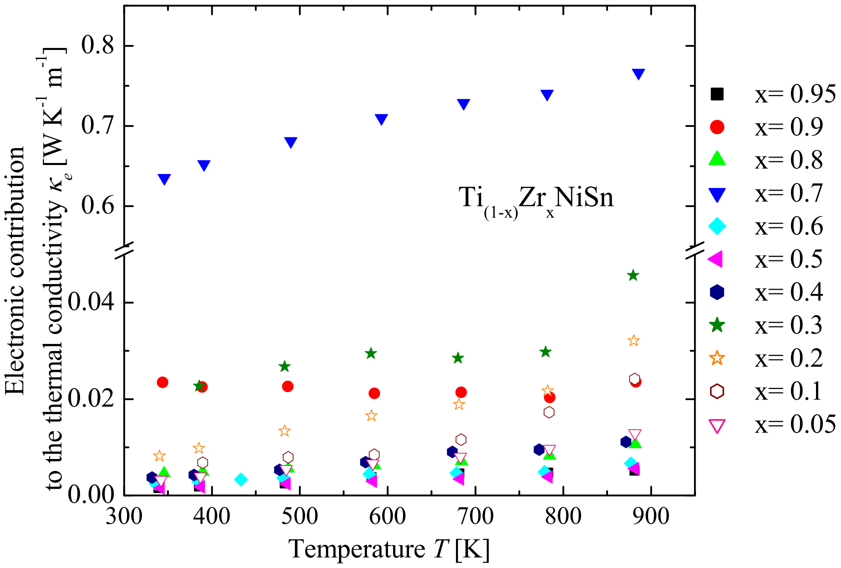

FIG. 75: Temperature dependence of the electronic contribution to the thermal conductivity of the Ti$_{(1-x)}$Zr$_x$NiSn series in comparison to the parent compounds.

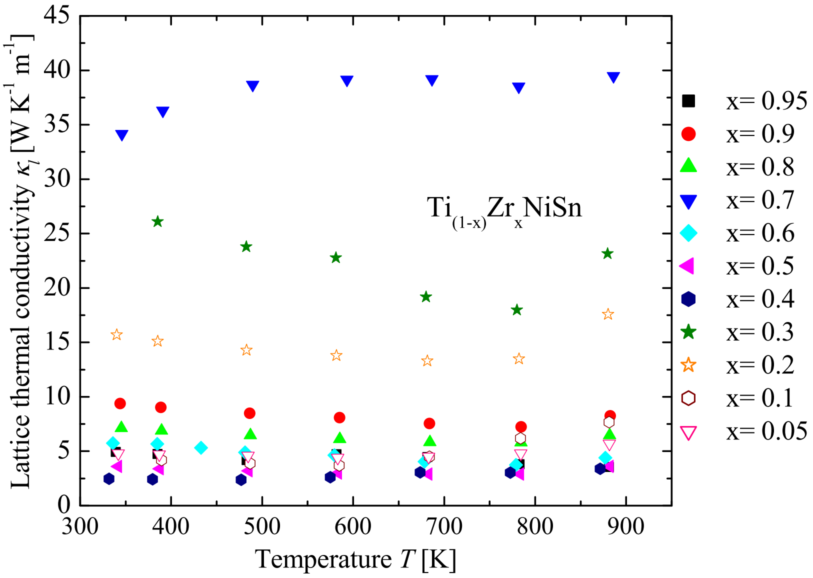

FIG. 76: Temperature dependence of the lattice thermal conductivity of the Ti$_{(1-x)}$Zr$_x$NiSn series in comparison to the parent compounds.

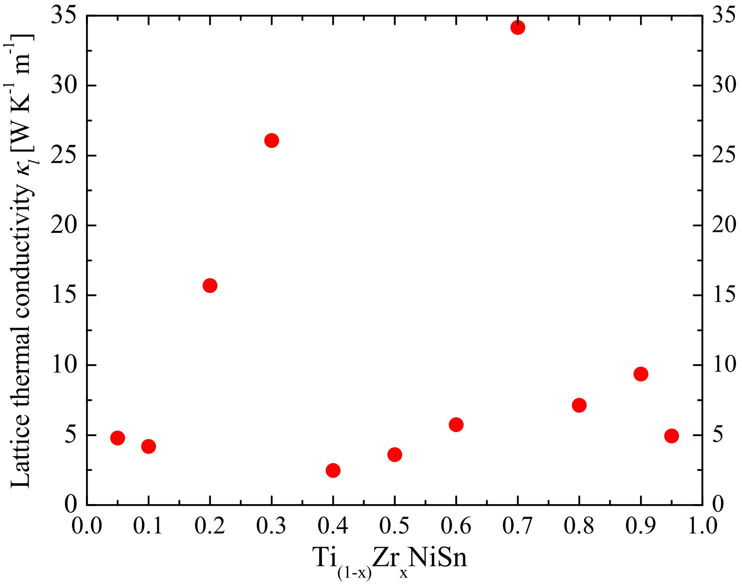

FIG. 77: Lattice thermal conductivity at 300 K of the $Ti_{(1-x)}Zr_xNiSn$ series in dependence on the zirconium concentration $x$.

### $\mathbf{Ti_{(1-x)}Hf_xNiSn}$

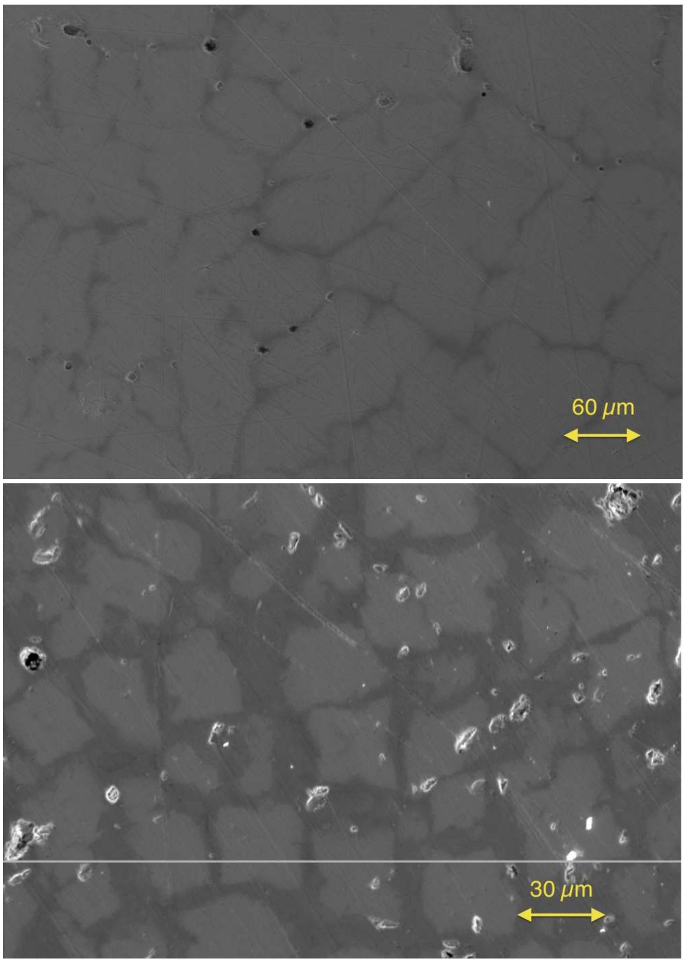

FIG. 78: Scanning electron microscope images of $Ti_{0.2}Hf_{0.8}NiSn$ (top) and $Ti_{0.7}Hf_{0.3}NiSn$ (bottom).

Also the $Ti_{(1-x)}Hf_xNiSn$ series was investigated to prove if this series is no solid solution. The values of the lattice parameters $a$ and the phase compositions are shown in Figure VIII. In this series a dependence of the lattice parameters on the Hf concentration is also recognizable. Analogous to the two series above the comparison of the detected phases lead to five different $C1_b$ phases. Together with the parent phases TiNiSn and HfNiSn, the phases $Ti_{0.83}Hf_{0.17}NiSn$(VII), $Ti_{0.61}Hf_{0.39}NiSn$(VI) and $Ti_{0.24}Zr_{0.76}NiSn$(V) were found. And again in comparison to the $Zr_{(1-x)}Hf_xNiSn$ and the $Ti_{(1-x)}Zr_xNiSn$ series the stable Heusler $C1_b$ phases found are almost the same. This result shows that the formation of stable Heusler $C1_b$ phases is dependent on the chemical character of the constructing elements and that the atom size has almost no influence of the formation of a stable $C1_b$ phase. What means that the covalent contribution to the bonding plays an important role for the formation of a

| Weighed composition $Ti_{(1-x)}Hf_xNiSn$ | Detected phases | Ratio | a [Å] |
|---|---|---|---|
| TiNiSn | TiNiSn, $Ni_2TiSn$, $Ti_6Sn_5$, Sn | 85% TiNiSn | 5.939(5) |
| $Ti_{0.95}Hf_{0.05}NiSn$ | TiNiSn, $Ni_2TiSn$, $Ti_6Sn_5$, Hf | 85% TiNiSn | 5.940(5) |
| $Ti_{0.9}Hf_{0.1}NiSn$ | $Ti_{0.87}Hf_{0.13}NiSn$(VII), $Ti_6Sn_5$ | 90% (VII) | 5.955(5) |
| $Ti_{0.8}Hf_{0.2}NiSn$ | $Ti_{0.83}Hf_{0.17}NiSn$(VII) | 97%(VII) | 5.971(5) |
| $Ti_{0.7}Hf_{0.3}NiSn$ | $Ti_{0.87}Hf_{0.13}NiSn$(VII), $Ti_{0.61}Hf_{0.39}NiSn$(VI) | $\frac{50\%(VII)}{50\%(VI)}$ | 5.954(5)/5.991(5) |
| $Ti_{0.6}Hf_{0.4}NiSn$ | $Ti_{0.64}Hf_{0.36}NiSn$(VI), $Ti_6Sn_5$ | 95% (VI) | 5.995(5) |
| $Ti_{0.5}Hf_{0.5}NiSn$ | $Ti_{0.59}Hf_{0.41}NiSn$(VI), $Ti_{0.26}Hf_{0.74}NiSn$(V) | $\frac{30\%(VI)}{70\%(V)}$ | 6.038(5) |
| $Ti_{0.4}Hf_{0.6}NiSn$ | $Ti_{0.79}Hf_{0.21}NiSn$(VII), $Ti_{0.27}Hf_{0.73}NiSn$(V) | $\frac{30\%(VII)}{70\%(V)}$ | 6.043(5) |
| $Ti_{0.3}Hf_{0.7}NiSn$ | $Ti_{0.19}Hf_{0.81}NiSn$(V), $Ti_6Sn_5$ | 85% (V) | 6.045(5) |
| $Ti_{0.2}Hf_{0.8}NiSn$ | $Ti_{0.19}Hf_{0.81}NiSn$(V), $Ti_6Sn_5$ | 95% (V) | 6.071(5) |
| $Ti_{0.1}Hf_{0.9}NiSn$ | HfNiSn,$Ti_6Sn_5$ | 90% HfNiSn | 6.090(5) |
| $Ti_{0.05}Hf_{0.95}NiSn$ | HfNiSn, $Ti_6Sn_5$ | 95% HfNiSn | 6.089(5) |
| HfNiSn | HfNiSn, Sn | 97% HfNiSn | 6.091(5) |

TABLE VIII: The phase compositions of the different $Ti_{(1-x)}Hf_xNiSn$ samples and the parent samples.

| Stable compositions |
|---|
| TiNiSn |
| $Ti_{0.87}Hf_{0.13}NiSn$(VII) |
| $Ti_{0.64}Hf_{0.36}NiSn$(VI) |
| $Ti_{0.19}Hf_{0.81}NiSn$(V) |
| HfNiSn |

TABLE IX: Compositions of the stable Heusler phases with an error range of 3%.

stable composition. Two examples of SEM images of a phase separated and an almost clean sample are shown in Figure 78. In Figure 79 the produced compositions (light blue) and the detected phases (red) are indicated in the Gibbs triangle for the $Ti_{(1-x)}Hf_xNiSn$ system. In the Figures 80-83, the measured physical properties of the $Ti_{(1-x)}Hf_xNiSn$ series are com-

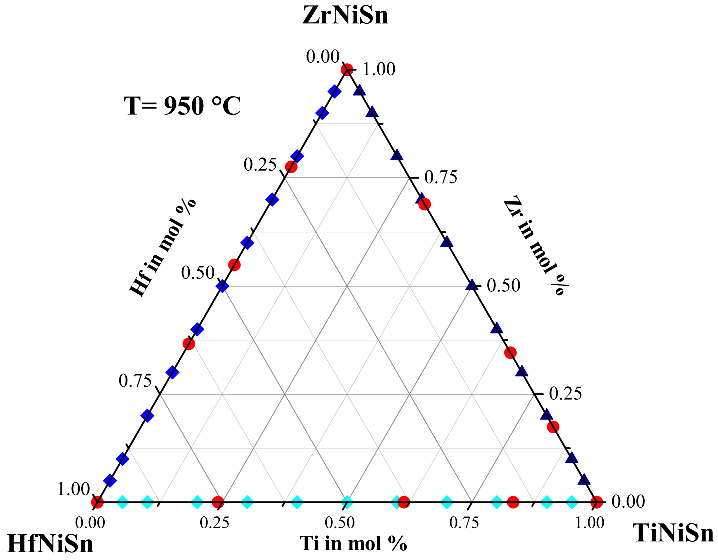

FIG. 79: The $Ti_{(1-x)}Hf_xNiSn$ series with the detected phases indicated in the Gibbs triangle.

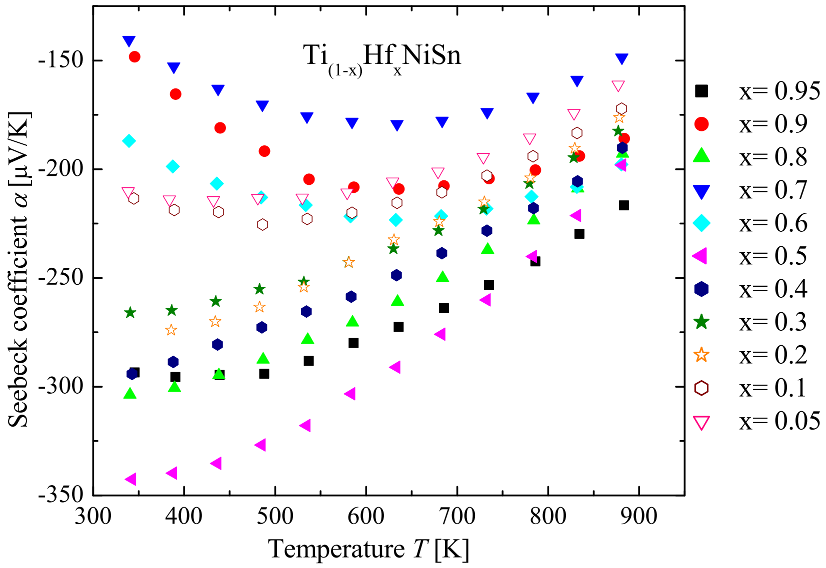

FIG. 80: Seebeck coefficient of the $Ti_{(1-x)}Hf_xNiSn$ series in comparison to the parent compounds.

pared. All samples of the $Ti_{(1-x)}Hf_xNiSn$ series are n-type semiconductors, indicated by the negative values of the Seebeck coefficient (see Figure 80). Similar to the results in the two series above the samples with one Heusler phase with $C1_b$ structure or a decomposition of two

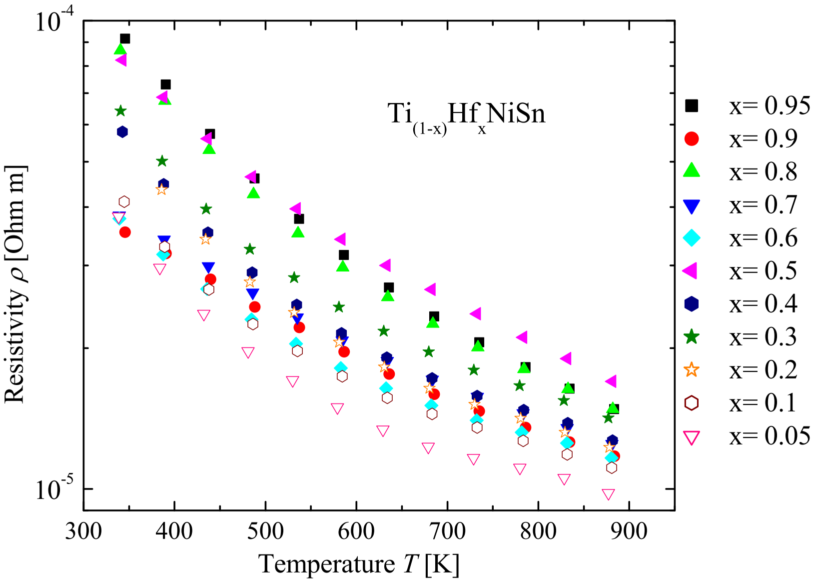

FIG. 81: Electrical resistivity of the $Ti_{(1-x)}Hf_xNiSn$ series in comparison to the parent compounds.

Heusler phases with $C1_b$ structure exhibit high values of the Seebeck coefficient. The compositions are $Ti_{0.05}Hf_{0.95}NiSn$, $Ti_{0.2}Hf_{0.8}NiSn$, $Ti_{0.5}Hf_{0.5}NiSn$, $Ti_{0.6}Hf_{0.4}NiSn$, $Ti_{0.7}Hf_{0.3}NiSn$ and $Ti_{0.8}Hf_{0.2}NiSn$. Additionally, the results are in a good agreement with the stable phases (see Table VIII or Figure 79). Also the values of the resistivity follow the same trend as the values of the Seebeck coefficient (Figure 81). Analogous to the $Zr_{(1-x)}Hf_xNiSn$ series the $Ti_{(1-x)}Hf_xNiSn$ samples with show high values of the Seebeck coefficient high values of the thermal conductivity. The thermal conductivity of these samples seem to be dominated by the crystallinity of the samples, except the sample $Ti_{0.6}Hf_{0.4}NiSn$, which exhibits a very low conductivity. This can be seen in Figure 85, showing the values of lattice thermal conductivity, which is almost the total thermal conductivity, because of the low impurities and disorder. The electronic contribution to the thermal conductivity shows very small values, because of the high resistivity values. The dependence of the lattice thermal conductivity on the hafnium concentration (see Figure 86) shows that the $Ti_{(1-x)}Hf_xNiSn$ series is no solid solution. As mentioned above the samples with high Seebeck coefficient, high crystallinity and low impurities, exhibit high thermal conductivity. The lattice thermal conductivity shows a slight increase at high temperatures, what happens due to bipolar contribution to the conduction.[36] In Figure 83 the temperature dependence of the Figure of Merit is shown.

Similar to the $Zr_{(1-x)}Hf_xNiSn$ seriesvthe Figure of Merit is dominated by the high values of the Seebeck coefficient (see Table X). This is not unexpected because the resistivity values are in the same order of magnitude and hence the impact on the Figure of Merit by the Seebeck coefficient is high.

| Composition $Ti_{(1-x)}Hf_xNiSn$ | Seebeck coefficient $\alpha$ [$\frac{\mu V}{K}$] | Resistivity $\rho$ [Ohm m] | Thermal conductivity $\kappa$ [$\frac{W}{Km}$] | Figure of Merit $ZT$ |
|---|---|---|---|---|
| HfNiSn | -167 | $6.2\cdot10^{-5}$ | 6.9 | 0.023 |
| $Ti_{0.05}Hf_{0.95}NiSn$ | -293 | $9.2\cdot10^{-5}$ | 8.1 | 0.040 |
| $Ti_{0.1}Hf_{0.9}NiSn$ | -148 | $3.5\cdot10^{-5}$ | 5.6 | 0.038 |
| $Ti_{0.2}Hf_{0.8}NiSn$ | -304 | $8.6\cdot10^{-5}$ | 5.4 | 0.097 |
| $Ti_{0.3}Hf_{0.7}NiSn$ | -141 | $3.8\cdot10^{-5}$ | 12.3 | 0.022 |
| $Ti_{0.4}Hf_{0.6}NiSn$ | -199 | $3.2\cdot10^{-5}$ | 14.3 | 0.034 |
| $Ti_{0.5}Hf_{0.5}NiSn$ | -343 | $8.2\cdot10^{-5}$ | 6.5 | 0.100 |
| $Ti_{0.6}Hf_{0.4}NiSn$ | -294 | $5.8\cdot10^{-5}$ | 1.9 | 0.272 |
| $Ti_{0.7}Hf_{0.3}NiSn$ | -266 | $6.4\cdot10^{-5}$ | 4.0 | 0.135 |
| $Ti_{0.8}Hf_{0.2}NiSn$ | -274 | $4.4\cdot10^{-5}$ | 11.8 | 0.056 |
| $Ti_{0.9}Hf_{0.1}NiSn$ | -213 | $4.1\cdot10^{-5}$ | 4.6 | 0.123 |
| $Ti_{0.95}Hf_{0.05}NiSn$ | -210 | $3.8\cdot10^{-5}$ | 6.1 | 0.097 |
| TiNiSn | -117 | $2.8\cdot10^{-5}$ | 8.4 | 0.014 |

TABLE X: Physical properties of the $Ti_{(1-x)}Hf_xNiSn$ series in comparison to the parent compounds at 350 K.

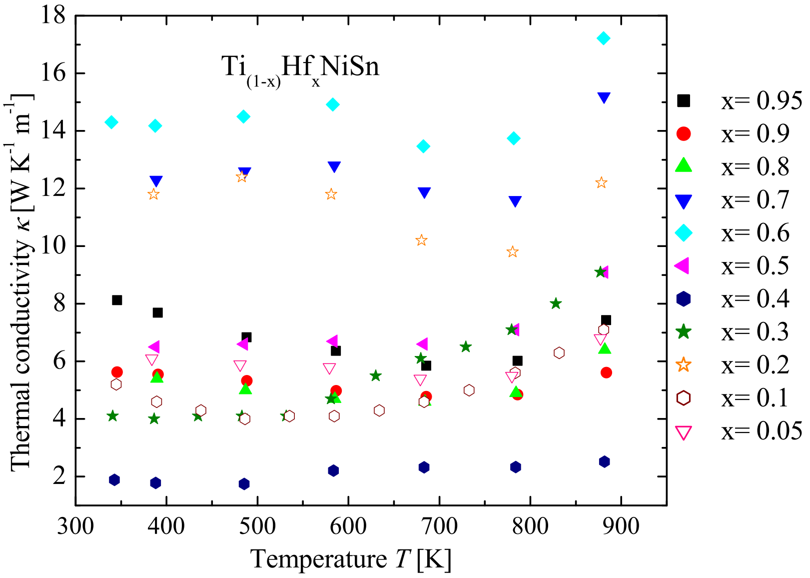

FIG. 82: Thermal conductivity of the Ti$_{(1-x)}$Hf$_x$NiSn series in comparison to the parent compounds.

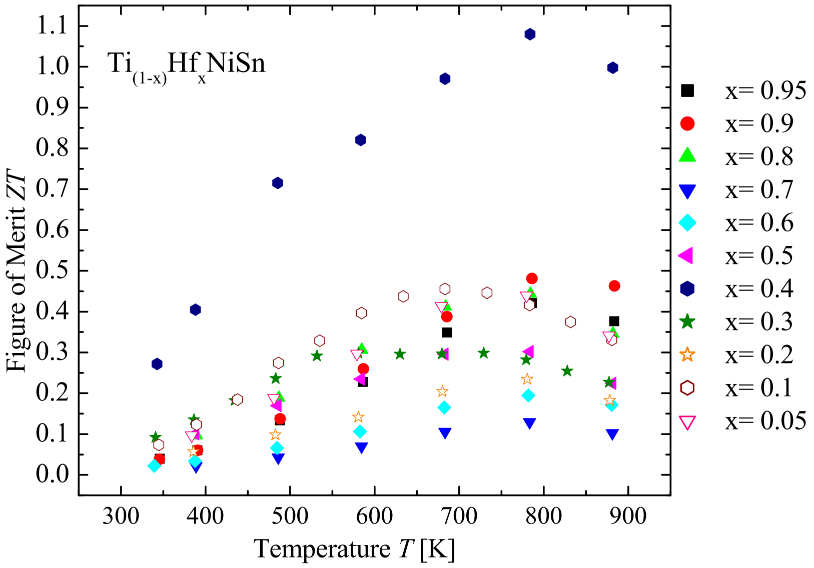

FIG. 83: Figure of Merit of the Ti$_{(1-x)}$Hf$_x$NiSn series in comparison to the parent compounds.

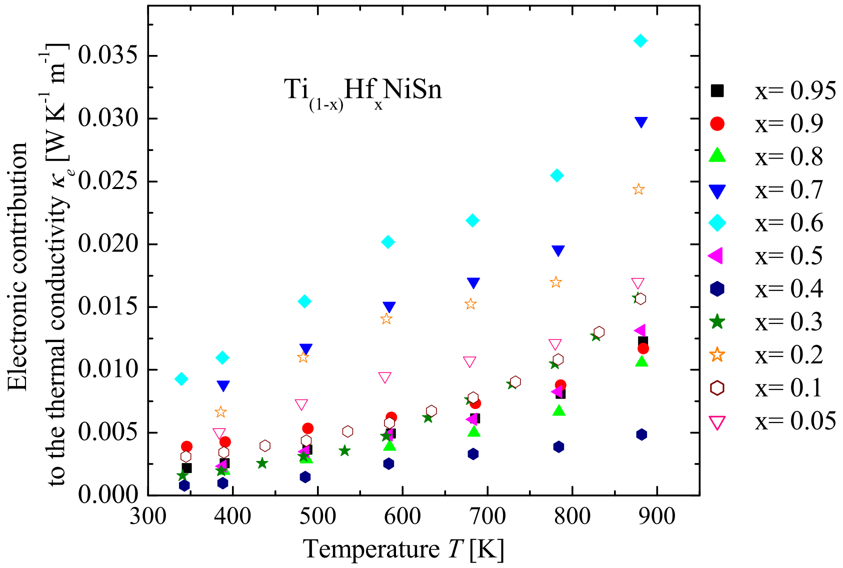

FIG. 84: Temperature dependence of the electronic contribution to the thermal conductivity of the Ti$_{(1-x)}$Hf$_x$NiSn series in comparison to the parent compounds.

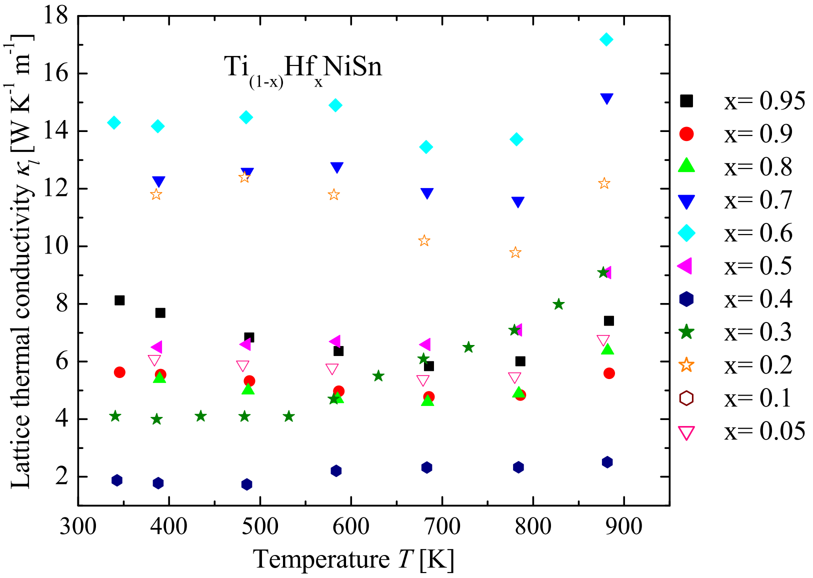

FIG. 85: Temperature dependence of the lattice thermal conductivity of the Ti$_{(1-x)}$Hf$_x$NiSn series in comparison to the parent compounds.

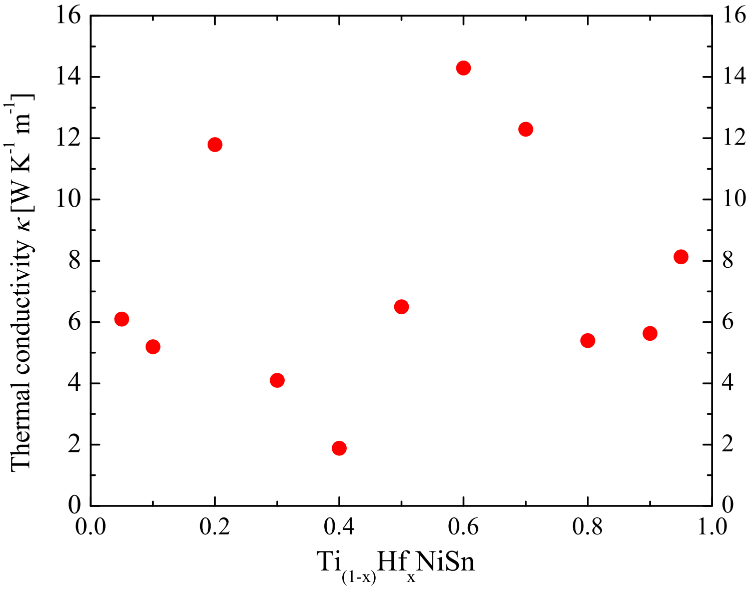

FIG. 86: Lattice thermal conductivity at 300 K of the $Ti_{(1-x)}Hf_xNiSn$ series in dependence on the hafnium concentration $x$.

### $\mathbf{Ti_{(1-x)}(Zr_{0.5}Hf_{0.5})_xNiSn}$

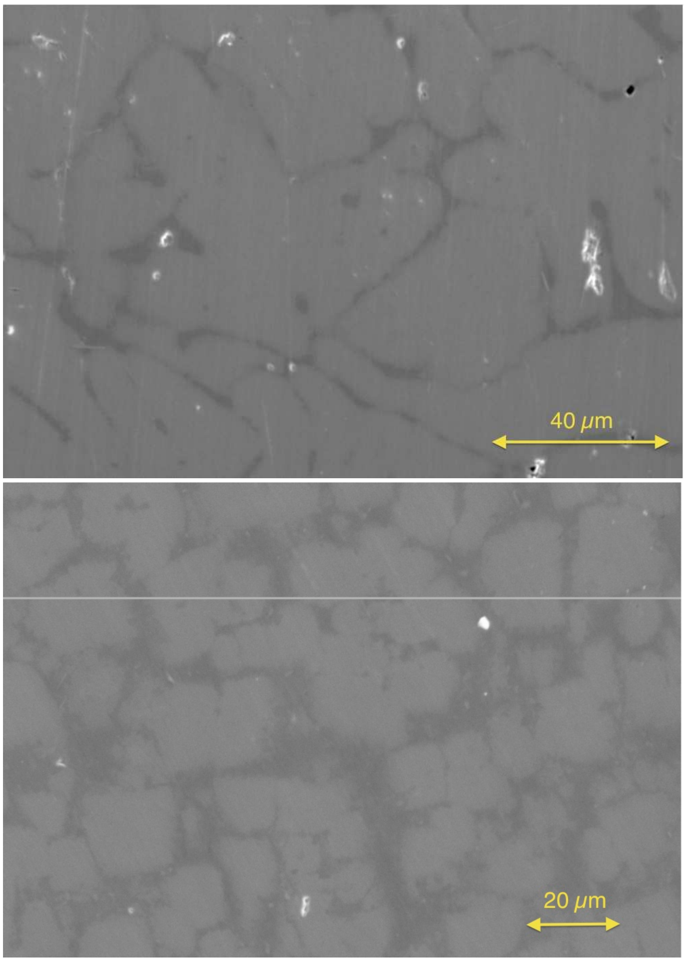

FIG. 87: Scanning electron microscope images of $Ti_{0.2}(Zr_{0.5}Hf_{0.5})_{0.8}NiSn$ (top) and $Ti_{0.4}(Zr_{0.5}Hf_{0.5})_{0.6}NiSn$ (bottom).

To combine the three series above, but to avoid the complexity of three different parameters, one parameter was fixed. With respect to that the $Ti_{(1-x)}(Zr_{0.5}Hf_{0.5})_xNiSn$ series was investigated. Except the samples with low Ti or $(Zr_{0.5}Hf_{0.5})$ concentrations all samples are phase separated (see Table XI). The XRD measurements show three samples with phase separations, but the other XRD measurements of the series exhibit just a broadening of the reflections, what can indicate that a sample consists of an additional phase with similar lattice parameter. The fitted lattice parameters $a$ and the phase compositions are shown in Table XI. The obtained lattice parameters indicate a slight dependence of the Ti concentration, but the phases detected by EDX show that just seven different

Heusler $C1_b$ phases were found. Beside the parent phase, TiNiSn and $Zr_{0.55}Hf_{0.45}NiSn$(XIII), $Ti_{0.82}Zr_{0.18}NiSn$(IX), $Ti_{0.83}Hf_{0.17}NiSn$(VII) found in the series above, only three phases were obtained: $Ti_{0.68}Zr_{0.18}Hf_{0.13}NiSn$(I), $Ti_{0.43}Zr_{0.28}Hf_{0.29}NiSn$(III) and $Ti_{21}Zr_{0.40}Hf_{0.39}NiSn$(IV). Two examples of SEM images of a phase separated and an almost clean sample are shown in Figure 87. The results are similar to the results of the other series. It is remarkable that stable $C1_b$ phases are found from the other series above, hence these results are consistent with the results from the other series. A slight relation seems to exist between the "binary" ($Zr_{(1-x)}Hf_xNiSn$, $Ti_{(1-x)}Zr_xNiSn$,$Ti_{(1-x)}Hf_xNiSn$) series and this "ternary" series (see Figure 88).

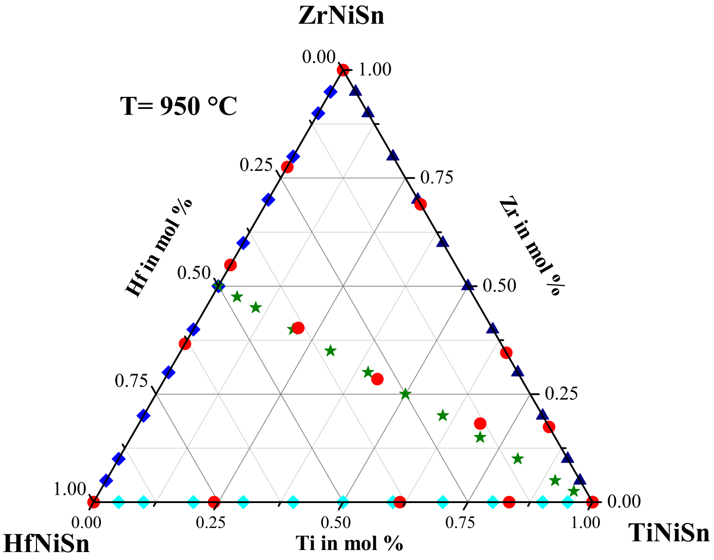

FIG. 88: The $Ti_{(1-x)}(Zr_{0.5}Hf_{0.5})_xNiSn$ series with the detected phases indicated in the Gibbs triangle.

| Weighed composition $Ti_{(1-x)}(Zr_{0.5}Hf_{0.5})_xNiSn$ | Detected phases | Ratio | a [Å] |
|---|---|---|---|
| $Zr_{0.5}Hf_{0.5}NiSn$ | $Zr_{0.49}Hf_{0.51}NiSn$(XIII) | 95% (XIII) | 6.101(5) |
| $Ti_{0.05}(Zr_{0.5}Hf_{0.5})_{0.95}NiSn$ | $Zr_{0.53}Hf_{0.47}NiSn$(XIII), $Ti_6Sn_5$ | 90% (XIII) | 6.109(5) |
| $Ti_{0.1}(Zr_{0.5}Hf_{0.5})_{0.9}NiSn$ | $Zr_{0.53}Hf_{0.47}NiSn$(XIII), $Ti_6Sn_5$ | 70% (XIII) | 6.117(5) |
| $Ti_{0.2}(Zr_{0.5}Hf_{0.5})_{0.8}NiSn$ | $Ti_{0.18}Zr_{0.42}Hf_{0.40}NiSn$(IV), $Ti_{0.44}Zr_{0.26}Hf_{0.28}NiSn$(III) | $\frac{95\%(IV)}{5\%(III)}$ | 6.090(5) |
| $Ti_{0.3}(Zr_{0.5}Hf_{0.5})_{0.7}NiSn$ | $Ti_{0.24}Zr_{0.39}Hf_{0.37}NiSn$(IV), $Ti_{0.44}Zr_{0.27}Hf_{0.29}NiSn$(III), $Ti_6Sn_5$, Sn | $\frac{80\%(IV)}{20\%(III)}$ | 6.092(5)/6.013(5) |
| $Ti_{0.4}(Zr_{0.5}Hf_{0.5})_{0.6}NiSn$ | $Ti_{0.30}Zr_{0.35}Hf_{0.35}NiSn$(III), $Ti_{0.65}Zr_{0.22}Hf_{0.13}NiSn$(I) | $\frac{60\%(III)}{40\%(I)}$ | 6.020(5) |
| $Ti_{0.5}(Zr_{0.5}Hf_{0.5})_{0.5}NiSn$ | $Ti_{0.39}Zr_{0.28}Hf_{0.34}NiSn$(III), $Ti_{0.76}Zr_{0.15}Hf_{0.09}NiSn$(I) | $\frac{50\%(III)}{50\%(I)}$ | 6.050(5)/5.986(5) |
| $Ti_{0.6}(Zr_{0.5}Hf_{0.5})_{0.4}NiSn$ | $Ti_{0.46}Zr_{0.26}Hf_{0.27}NiSn$(III), $Ti_{0.78}Zr_{0.14}Hf_{0.08}NiSn$(I) | $\frac{50\%(III)}{50\%(I)}$ | 6.045(5)/5.983(5) |
| $Ti_{0.7}(Zr_{0.5}Hf_{0.5})_{0.3}NiSn$ | $Ti_{0.54}Zr_{0.21}Hf_{0.26}NiSn$(III), $Ti_{0.74}Zr_{0.14}Hf_{0.11}NiSn$(I) | $\frac{30\%(III)}{70\%(I)}$ | 6.001(5) |
| $Ti_{0.8}(Zr_{0.5}Hf_{0.5})_{0.2}NiSn$ | $Ti_{0.89}Zr_{0.11}NiSn$(IX), $Ti_{0.69}Zr_{0.13}Hf_{0.19}NiSn$(I) | $\frac{60\%(IX)}{40\%(I)}$ | 5.973(5) |
| $Ti_{0.9}(Zr_{0.5}Hf_{0.5})_{0.1}NiSn$ | $Ti_{0.87}Hf_{0.13}NiSn$(VII), $Ti_6Sn_5$, $ZrSn_2$ | 70% (VII) | 5.957(5) |
| TiNiSn | TiNiSn, $Ni_2TiSn$, $Ti_6Sn_5$, Sn | 85% TiNiSn | 5.939(5) |

TABLE XI: The phase compositions of the different $Ti_{(1-x)}(Zr_{0.5}Hf_{0.5})_xNiSn$ samples and the parent samples.

| Stable compositions |
|---|
| $Zr_{0.49}Hf_{0.51}NiSn$(XIII) |
| $Ti_{0.18}Zr_{0.42}Hf_{0.40}NiSn$(IV) |
| $Ti_{0.30}Zr_{0.35}Hf_{0.35}NiSn$(III) |
| $Ti_{0.78}Zr_{0.14}Hf_{0.08}NiSn$(I) |
| $Ti_{0.89}Zr_{0.11}NiSn$(IX) |
| TiNiSn |

TABLE XII: Compositions of the stable Heusler phases in an error range of 3%.

In Figures 89-92, the measured physical properties of the $Ti_{(1-x)}(Zr_{0.5}Hf_{0.5})_xNiSn$ series are compared to the parent TiNiSn and $Zr_{0.5}Hf_{0.5}NiSn$ (also see Table XIII). All measured values of the Seebeck coefficient (see Figure 89) for the $Ti_{(1-x)}(Zr_{0.5}Hf_{0.5})_xNiSn$ series are negative, indicating n-type conduction. Analogue to the other series the samples, which almost possess the composition of the detected stable phases, exhibit high values of the Seebeck coefficient. It is also remarkable that samples with very similar phase compositions have the same values of the Seebeck coefficient and resistivity ($Ti_{0.4}(Zr_{0.5}Hf_{0.5})_{0.6}NiSn$,

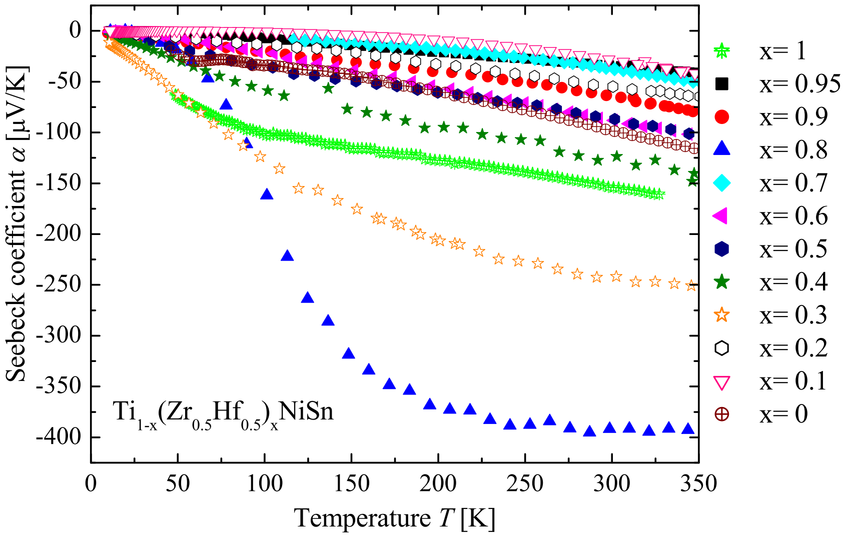

FIG. 89: Seebeck coefficient of the $Ti_{(1-x)}(Zr_{0.5}Hf_{0.5})_xNiSn$ series in comparison to the parent compounds.

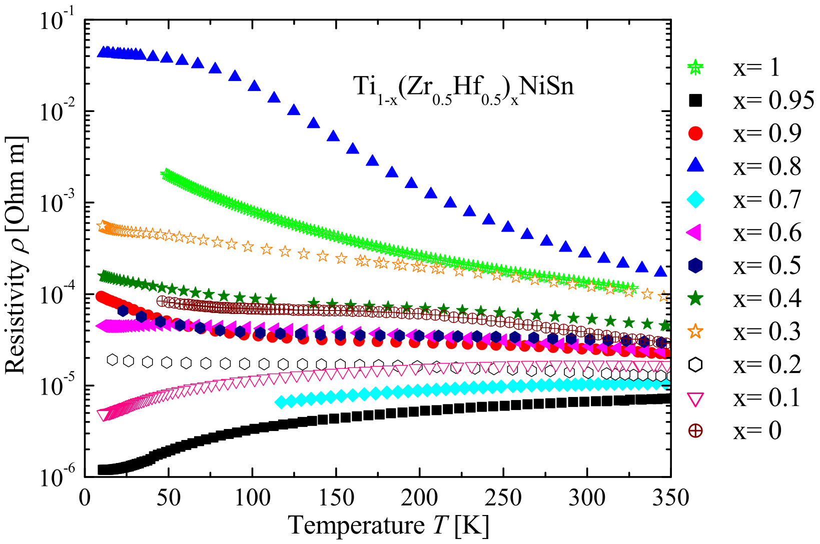

FIG. 90: Electrical resistivity of the $Ti_{(1-x)}(Zr_{0.5}Hf_{0.5})_xNiSn$ series in comparison to the parent compounds.

$Ti_{0.5}(Zr_{0.5}Hf_{0.5})_{0.5}NiSn$). This shows that the measurements are consistent and that the phase composition determines the transport properties. The resistivity values support the results of the Seebeck coefficient values (Figure 90). In the measurements of the thermal conductivity (Figure 91) the impact of the phase decomposition can be seen. All samples with a decomposition of two Heusler $C1_b$ phases exhibit a visible low lattice thermal conductivity due to the additional scattering at the grain and phase boundaries (see Figure 94). The electronic thermal conductivity $\kappa_e$ (see Figure 93) exhibits low values for the samples with a phase separation, except the samples $Ti_{0.3}(Zr_{0.5}Hf_{0.5})_{0.7}NiSn$ and $Ti_{0.8}(Zr_{0.5}Hf_{0.5})_{0.2}NiSn$. This can be explained by impurities in sample $Ti_{0.3}(Zr_{0.5}Hf_{0.5})_{0.7}NiSn$ and by the presence of the $Ti_{0.89}Zr_{0.11}NiSn$(IX) phase, which exhibits a low resistivity (see Figure 71) in sample $Ti_{0.8}(Zr_{0.5}Hf_{0.5})_{0.2}NiSn$ (see Table XI). Figure 95 shows the dependence of the lattice thermal conductivity on the Zr/Hf concentration. No solid solution is obtained. The samples with phase separation exhibit low values due to the increased grain boundary scattering. The samples with segregations, e.g. Zr/Hf 0.3, show higher thermal conductivities, because of the mixture of Heusler phases, with low lattice thermal conductivities and binary alloys which usually exhibit high lattice thermal conductivities in comparison to these Heusler compounds. Figure 92 shows the temperature dependence of the Figure of Merit. The values of the Figure of Merit are dominated by the high values of the Seebeck coefficient and the mentioned low thermal conductivity.

| Composition | Seebeck coefficient | Resistivity | Thermal conductivity | Figure of Merit |
|---|---|---|---|---|
| $Ti_{(1-x)}(Zr_{0.5}Hf_{0.5})_xNiSn$ | $\alpha$ [$\frac{\mu V}{K}$] | $\rho$ [Ohm m] | $\kappa$ [$\frac{W}{Km}$] | $ZT$ |
| $Zr_{0.5}Hf_{0.5}NiSn$ | -154 | $1.3 \cdot 10^{-4}$ | 2.3 | 0.024 |
| $Ti_{0.05}(Zr_{0.5}Hf_{0.5})_{0.95}NiSn$ | -34 | $6.7 \cdot 10^{-6}$ | 8.0 | 0.007 |
| $Ti_{0.1}(Zr_{0.5}Hf_{0.5})_{0.9}NiSn$ | -63 | $2.5 \cdot 10^{-5}$ | 9.5 | 0.005 |
| $Ti_{0.2}(Zr_{0.5}Hf_{0.5})_{0.8}NiSn$ | -392 | $2.8 \cdot 10^{-4}$ | 4.6 | 0.036 |
| $Ti_{0.3}(Zr_{0.5}Hf_{0.5})_{0.7}NiSn$ | -38 | $1 \cdot 10^{-5}$ | 10.1 | 0.004 |
| $Ti_{0.4}(Zr_{0.5}Hf_{0.5})_{0.6}NiSn$ | -88 | $2.7 \cdot 10^{-5}$ | 4.5 | 0.019 |
| $Ti_{0.5}(Zr_{0.5}Hf_{0.5})_{0.5}NiSn$ | -87 | $3.2 \cdot 10^{-5}$ | 4.6 | 0.016 |
| $Ti_{0.6}(Zr_{0.5}Hf_{0.5})_{0.4}NiSn$ | -127 | $5.5 \cdot 10^{-5}$ | 6.1 | $3 \cdot 10^{-4}$ |
| $Ti_{0.7}(Zr_{0.5}Hf_{0.5})_{0.3}NiSn$ | -242 | $1.3 \cdot 10^{-4}$ | 2.5 | 0.060 |
| $Ti_{0.8}(Zr_{0.5}Hf_{0.5})_{0.2}NiSn$ | -55 | $1.4 \cdot 10^{-5}$ | 5.7 | 0.011 |
| $Ti_{0.9}(Zr_{0.5}Hf_{0.5})_{0.1}NiSn$ | -28 | $1.7 \cdot 10^{-5}$ | 6.0 | 0.002 |
| TiNiSn | -99 | $3.7 \cdot 10^{-5}$ | 8.4 | 0.007 |

TABLE XIII: Physical properties of the $Ti_{(1-x)}(Zr_{0.5}Hf_{0.5})_xNiSn$ series in comparison to the parent compounds at 300 K.

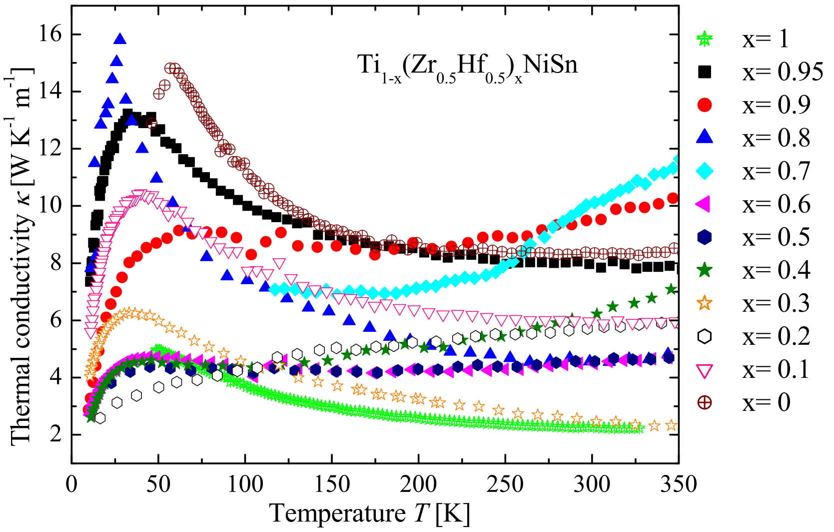

FIG. 91: Thermal conductivity of the $\mathrm{Ti}_{(1-x)}(\mathrm{Zr}_{0.5}\mathrm{Hf}_{0.5})_x\mathrm{NiSn}$ series in comparison to the parent compounds.

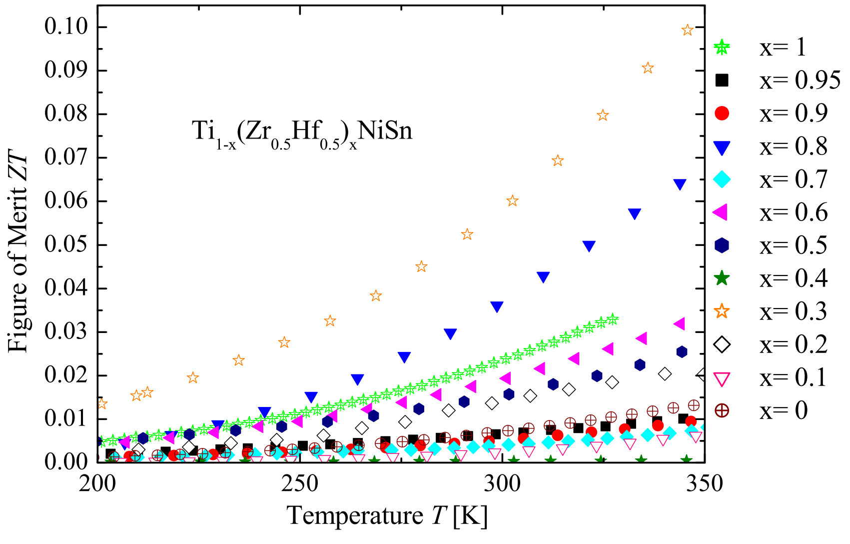

FIG. 92: Figure of Merit of the $\mathrm{Ti}_{(1-x)}(\mathrm{Zr}_{0.5}\mathrm{Hf}_{0.5})_x\mathrm{NiSn}$ series in comparison to the parent compounds.

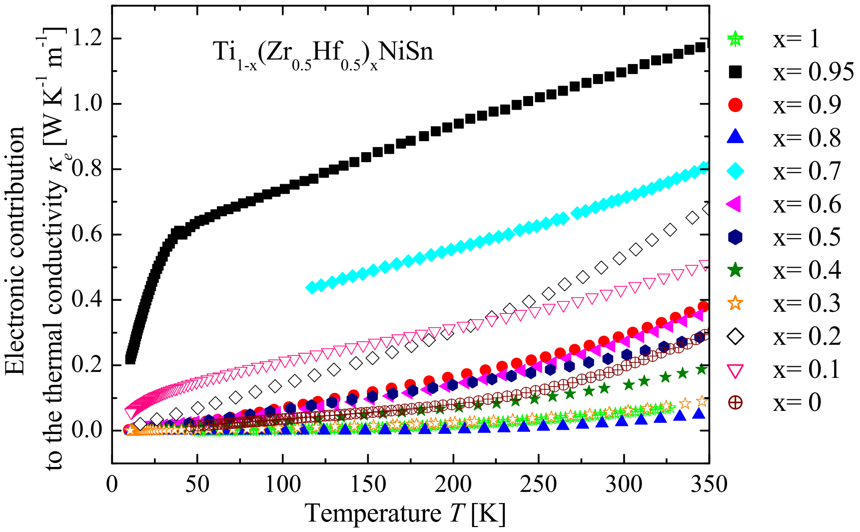

FIG. 93: Temperature dependence of the electronic contribution to the thermal conductivity of the Ti$_{(1-x)}$(Zr$_{0.5}$Hf$_{0.5}$)$_x$NiSn series in comparison to the parent compounds.

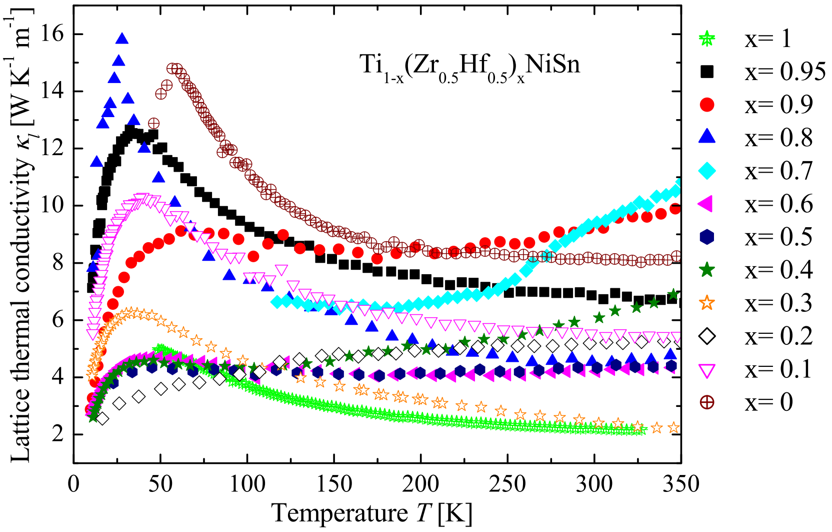

FIG. 94: Temperature dependence of the lattice thermal conductivity of the Ti$_{(1-x)}$(Zr$_{0.5}$Hf$_{0.5}$)$_x$NiSn series in comparison to the parent compounds.

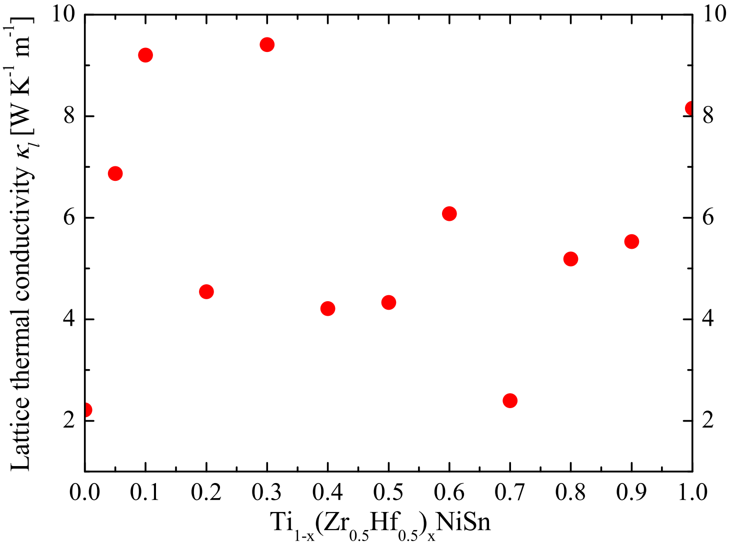

FIG. 95: Lattice thermal conductivity at 300 K of the $\mathrm{Ti}_{(1-x)}(\mathrm{Zr}_{0.5}\mathrm{Hf}_{0.5})_x\mathrm{NiSn}$ series in dependence on the hafnium concentration $x$.

### $\mathbf{Ti_xZr_yHf_zNiSn}$

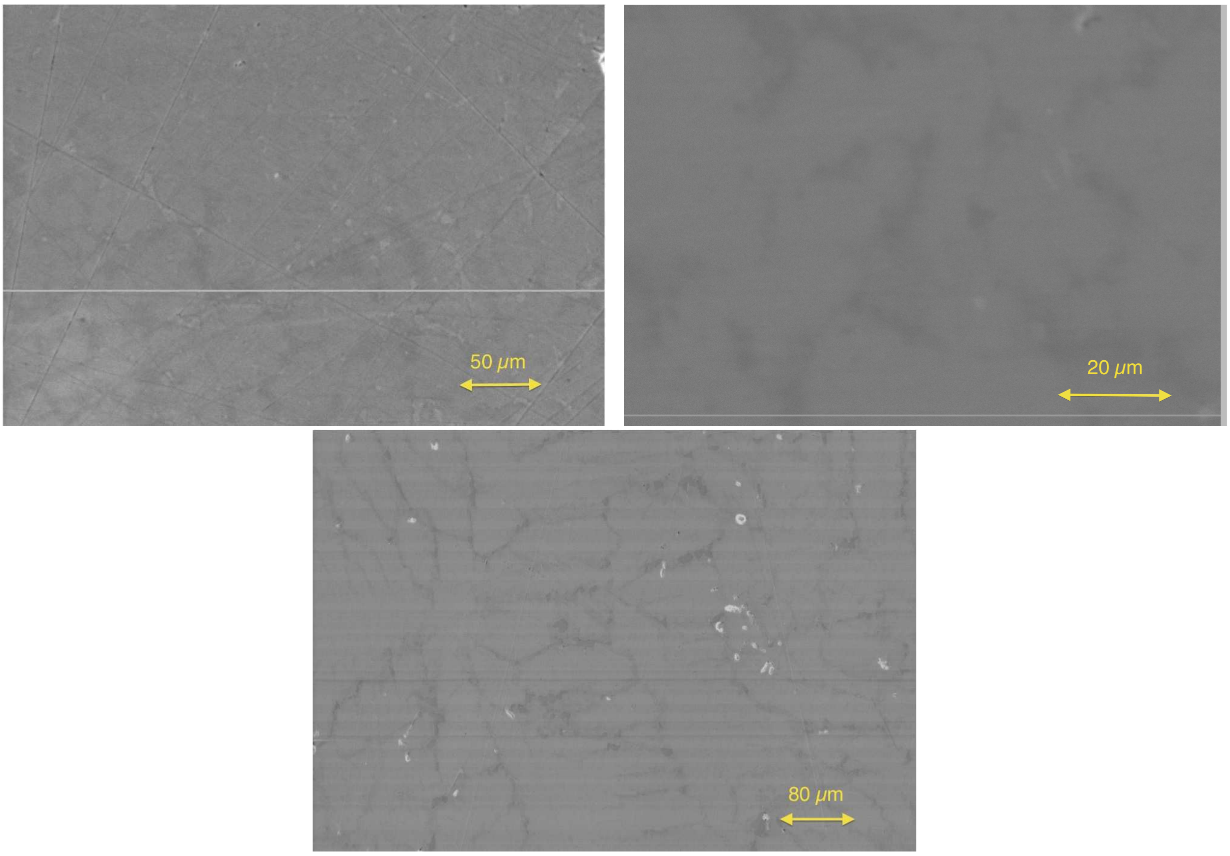

FIG. 96: Scanning electron microscope images of $Ti_{0.68}Zr_{0.17}Hf_{0.15}NiSn$ (top) , $Ti_{0.43}Zr_{0.28}Hf_{0.29}NiSn$ (middle) and $Ti_{0.21}Zr_{0.40}Hf_{0.39}NiSn$ (bottom).

To prove the results from the series above, three stable Heulser phases with different $Ti_xZr_yHf_zNiSn$ ratios were produced and characterized. Additionally, samples with varied Ti:Zr:Hf ratio were produced to see if the constructed Gibbs triangle works (Figure 97). The compositions of the produced and the detected phases are shown in Table XIV. All detected phases are in a good agreement with the results from the series above. The constructed Gibbs triangle seems to work. After several optimization steps the stable Heusler phases with $C1_b$ structure $Ti_{0.21}Zr_{0.40}Hf_{0.39}NiSn$(IV), $Ti_{0.43}Zr_{0.28}Hf_{0.29}NiSn$(III) and $Ti_{0.68}Zr_{0.17}Hf_{0.15}NiSn$(I) could be synthesized as single phase also. The SEM images are shown in Figure 96.

The physical properties of the stable phases are shown in Figures 98-102. The high values of the Seebeck coefficient show that the crystallinity is high and that impurities and strain do not influence the physical properties much. The resistivity values diverge between the sam-

| Weighed composition $\mathrm{Ti}_x\mathrm{Zr}_y\mathrm{Hf}_z\mathrm{NiSn}$ | Detected phases | Ratio |
|---|---|---|
| $\mathrm{Ti_{0.4}Zr_{0.48}Hf_{0.12}NiSn}$ | $\mathrm{Ti_{0.64}Zr_{0.36}NiSn(X)}$, $\mathrm{Ti_{0.29}Zr_{0.71}NiSn(XI)}$, Hf | $\frac{20\%(X)}{80\%(XI)}$ |
| $\mathrm{Ti_{0.5}Zr_{0.4}Hf_{0.1}NiSn}$ | $\mathrm{Ti_{0.70}Zr_{0.30}NiSn(X)}$, $\mathrm{Ti_{0.29}Zr_{0.71}NiSn(XI)}$, Hf | $\frac{30\%(X)}{70\%(XI)}$ |
| $\mathrm{Ti_{0.6}Zr_{0.32}Hf_{0.08}NiSn}$ | $\mathrm{Ti_{0.77}Zr_{0.23}NiSn(IX)}$, $\mathrm{Ti_{0.39}Zr_{0.61}NiSn(XI)}$, Hf | $\frac{40\%(IX)}{60\%(XI)}$ |
| $\mathrm{Ti_{0.7}Zr_{0.24}Hf_{0.06}NiSn}$ | $\mathrm{Ti_{0.83}Zr_{0.16}NiSn(IX)}$, $\mathrm{Ti_{0.65}Zr_{0.35}NiSn(X)}$, Hf | $\frac{50\%(IX)}{50\%(X)}$ |
| $\mathrm{Ti_{0.4}Zr_{0.24}Hf_{0.36}NiSn}$ | $\mathrm{Ti_{0.70}Zr_{0.16}Hf_{0.14}NiSn(I)}$, $\mathrm{Zr_{0.39}Hf_{0.61}NiSn(XIV)}$ | $\frac{30\%(I)}{70\%(XIV)}$ |
| $\mathrm{Ti_{0.5}Zr_{0.2}Hf_{0.3}NiSn}$ | TiNiSn, $\mathrm{Zr_{0.38}Hf_{0.62}NiSn(XIV)}$ | 70%(XIV) |
| $\mathrm{Ti_{0.6}Zr_{0.16}Hf_{0.24}NiSn}$ | TiNiSn, $\mathrm{Zr_{0.40}Hf_{0.60}NiSn(XIV)}$ | 80%(XIV) |
| $\mathrm{Ti_{0.7}Zr_{0.12}Hf_{0.18}NiSn}$ | TiNiSn, $\mathrm{Ti_{0.66}Hf_{0.34}NiSn(VI)}$, Zr | 70%(VI) |
| $\mathrm{Ti_{0.21}Zr_{0.40}Hf_{0.39}NiSn}$ | $\mathrm{Ti_{0.21}Zr_{0.40}Hf_{0.39}NiSn(IV)}$ | 97%(IV) |
| $\mathrm{Ti_{0.43}Zr_{0.28}Hf_{0.29}NiSn}$ | $\mathrm{Ti_{0.43}Zr_{0.28}Hf_{0.29}NiSn(III)}$ | 95%(III) |
| $\mathrm{Ti_{0.68}Zr_{0.17}Hf_{0.15}NiSn}$ | $\mathrm{Ti_{0.68}Zr_{0.17}Hf_{0.15}NiSn(I)}$ | 95%(I) |

TABLE XIV: The phase compositions of the different $\mathrm{Ti}_x\mathrm{Zr}_y\mathrm{Hf}_z\mathrm{NiSn}$ samples.

ple $\mathrm{Ti_{0.18}Zr_{0.42}Hf_{0.40}NiSn(IV)}$, $\mathrm{Ti_{0.78}Zr_{0.14}Hf_{0.08}NiSn(I)}$ and $\mathrm{Ti_{0.30}Zr_{0.35}Hf_{0.35}NiSn(III)}$. The sample $\mathrm{Ti_{0.30}Zr_{0.35}Hf_{0.35}NiSn(III)}$ and $\mathrm{Ti_{0.78}Zr_{0.14}Hf_{0.08}NiSn(I)}$ show a comparable resistivity and comparable values of the Seebeck coefficient, in contrast to this a higher value of the Seebeck coefficient and a higher resistivity are obtained in sample $\mathrm{Ti_{0.18}Zr_{0.42}Hf_{0.40}NiSn(IV)}$. The lattice thermal conductivity shows a remarkable low thermal conductivity for sample $\mathrm{Ti_{0.78}Zr_{0.14}Hf_{0.08}NiSn(I)}$, which also exhibits the highest electronic contribution to the thermal conductivity. The trend of the lattice thermal conductivity is inverse to the trend of the electronic contribution. The sample $\mathrm{Ti_{0.18}Zr_{0.42}Hf_{0.40}NiSn(IV)}$, which exhibits the largest values of the Seebeck coefficient, shows the highest lattice thermal conductivity possibly due to the high crystallinity. The high contributions to the electronic thermal conductivity of sample $\mathrm{Ti_{0.78}Zr_{0.14}Hf_{0.08}NiSn(I)}$ and $\mathrm{Ti_{0.30}Zr_{0.35}Hf_{0.35}NiSn(III)}$ is caused by the low electrical resistivity. The slight increase of the lattice thermal conductivity at high temperatures is due to bipolar contributions to the conduction.[36] The calculated Figure of Merit shows a high value of ZT= 0.8 for the sample $\mathrm{Ti_{0.78}Zr_{0.14}Hf_{0.08}NiSn(I)}$ due to the moderate value of the Seebeck coefficient, the low resistivity and the low thermal conductivity.

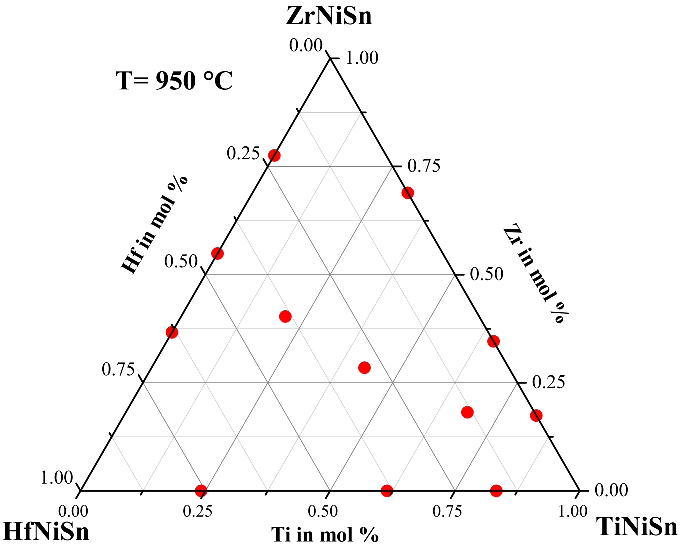

FIG. 97: The detected stable phases at 950°C indicated in the Gibbs triangle.

The values of sample $Ti_{0.18}Zr_{0.42}Hf_{0.40}NiSn$(IV) are dominated by high resistivity and the high thermal conductivity, caused by the high crystallinity. This shows that not only a high Seebeck coefficient leads to a high Figure of Merit, also a moderate value of the Seebeck coefficient and a low resistivity can lead to high value of the Figure of Merit. Sample $Ti_{0.30}Zr_{0.35}Hf_{0.35}NiSn$(III) exhibits a Figure of Merit of ZT= 0.5, because of the still high thermal conductivity.

| Stable compositions |
|---|
| TiNiSn |
| ZrNiSn |
| HfNiSn |
| $Zr_{0.85}Hf_{0.15}NiSn$(XII) |
| $Zr_{0.49}Hf_{0.51}NiSn$(XIII) |
| $Zr_{0.36}Hf_{0.64}NiSn$(XIV) |
| $Ti_{0.80}Zr_{0.19}NiSn$(IX) |
| $Ti_{0.66}Zr_{0.34}NiSn$(X) |
| $Ti_{0.29}Zr_{0.71}NiSn$(XI) |
| $Zr_{0.49}Hf_{0.51}NiSn$(XIII) |
| $Ti_{0.87}Hf_{0.13}NiSn$(VII) |
| $Ti_{0.64}Hf_{0.36}NiSn$(VI) |
| $Ti_{0.19}Hf_{0.81}NiSn$(V) |
| $Ti_{0.18}Zr_{0.42}Hf_{0.40}NiSn$(IV) |
| $Ti_{0.30}Zr_{0.35}Hf_{0.35}NiSn$(III) |
| $Ti_{0.78}Zr_{0.14}Hf_{0.08}NiSn$(I) |

TABLE XV: Compositions of the stable Heusler phases with an error range of 3%.

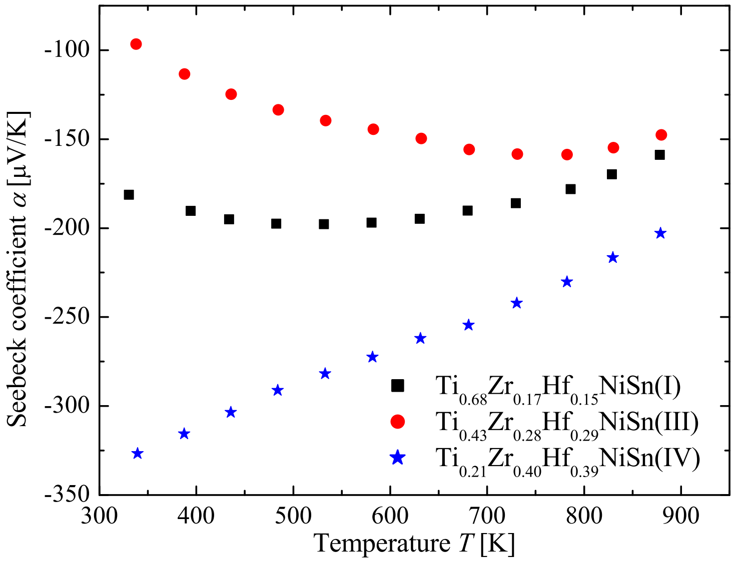

FIG. 98: Seebeck coefficient of the three stable phases with different $\mathrm{Ti}_x\mathrm{Zr}_y\mathrm{Hf}_z\mathrm{NiSn}$ ratios.

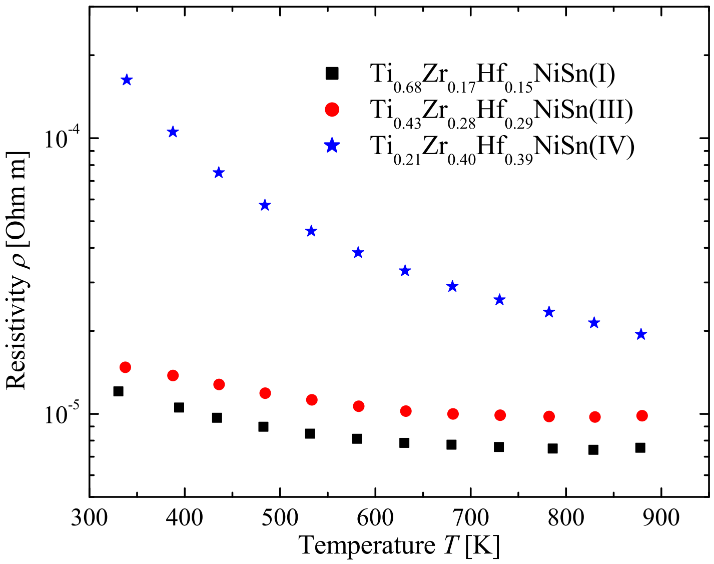

FIG. 99: Electrical resistivity of the three stable phases with different $\mathrm{Ti}_x\mathrm{Zr}_y\mathrm{Hf}_z\mathrm{NiSn}$ ratios.

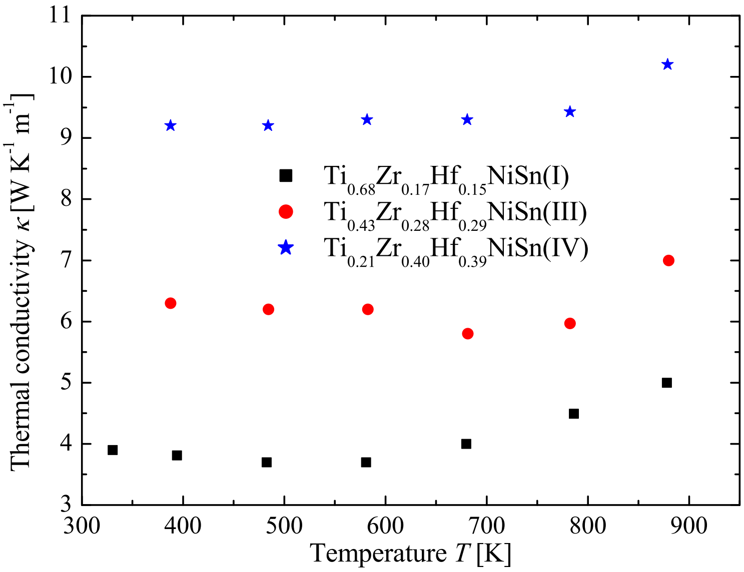

FIG. 100: Thermal conductivity of the three stable phases with different $Ti_xZr_yHf_zNiSn$ ratios

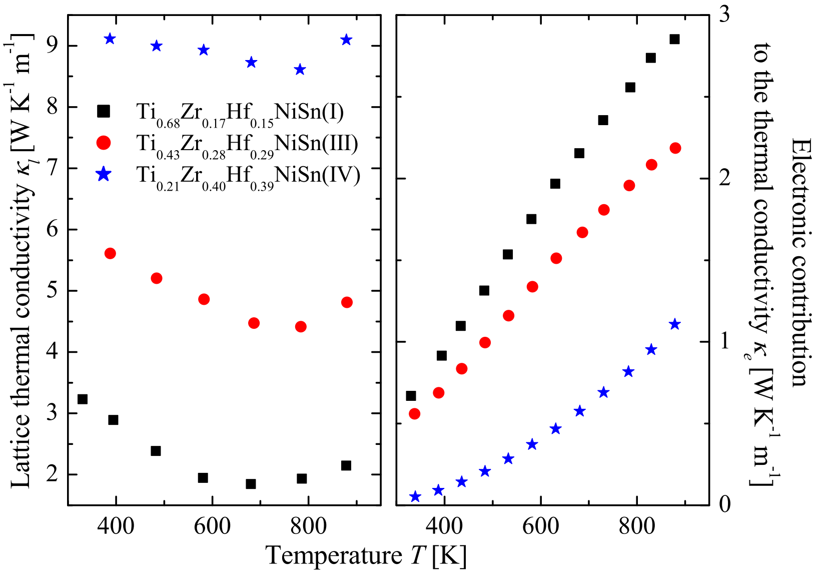

FIG. 101: Temperature dependence of the lattice thermal conductivity and the electronic contribution to the thermal conductivity of the three stable phases with different $Ti_xZr_yHf_zNiSn$ ratios.

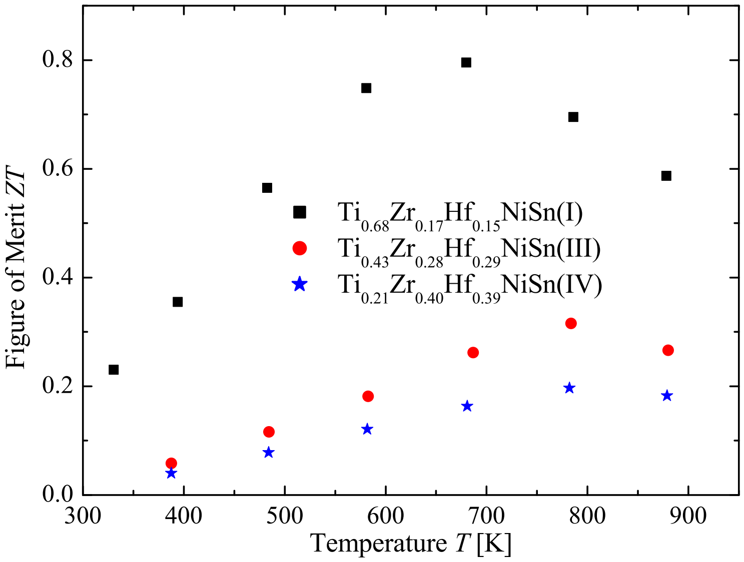

FIG. 102: Figure of Merit of the three stable phases with different $\mathrm{Ti}_x\mathrm{Zr}_y\mathrm{Hf}_z\mathrm{NiSn}$ ratios.

### $\mathbf{Ti_xZr_yHf_zNiSn}$ conclusion

In summary, in the quasi binary $Zr_{(1-x)}Hf_xNiSn$ system only three stable phases were determined, except the parent compounds. The thermal conductivity of the samples with almost one phase is in comparison to the parent compounds remarkably low, but the electronic properties are not adequate for the thermoelectric use. This is due to the fact that not the pure stable compounds were synthesized. The sample $Zr_{0.5}Hf_{0.5}NiSn$ accidentally meets the stable composition and therefore shows the best thermoelectric properties in this series.

The $Ti_{(1-x)}Zr_xNiSn$ system also exhibits three stable phases. Two stable compositions were accidentally synthesized and exhibit the highest values for the thermal conductivity, what can be explained by the better crystallinity. One interesting result in this system is the metallic behavior of the $Ti_{0.3}Zr_{0.7}NiSn$ sample, which is one of the stable compositions. Another result is that the two samples containing two Heusler phases exhibit low values for the thermal conductivity and hence the best thermoelectric properties. The sample $Ti_{0.6}Zr_{0.4}NiSn$, which consists of one Heusler phase and the binary phase $ZrSn_2$, shows the maximum value for the thermoelectric Figure of Merit $ZT = 1.1$ due to the especially low thermal conductivity.

The $Ti_{(1-x)}Hf_xNiSn$ system as well shows three stable Heusler phases. The samples, which almost consist of one Heusler phase, show the highest values for the Seebeck coefficient and the highest thermal conductivity due to the higher crystallinity. The samples with two Heusler phases again exhibit low values for the thermal conductivity, but the $Ti_{0.4}Hf_{0.6}NiSn$ sample, which consists of two Heusler phases, has an unusual high thermal conductivity, showing that not every phase decomposition leads to an improvement of the thermal conductivity.

In the $Ti_{(1-x)}(Zr_{0.5}Hf_{0.5})_xNiSn$ system also three stable Heusler phases were obtained. Except one sample, all samples with two Heusler phases exhibit low values for the thermal conductivity. The samples, which consist of almost one Heusler phase, exhibit the highest values of the Seebeck coefficient and the highest values of the resistivity. This characterizes the stable Heusler phases, what can be seen in the values of the transport properties of the stable phases (see Figures 98-102). In addition to the determination of the transport properties, hard x-ray photoelectron spectroscopy was applied to one of the stable compositions (see Figure 103). A high intensity next to the Fermi energy was observed and explains the high values for the Seebeck coefficients. The valence band in the *HAXPES* is indicated in Figure 103 and exhibits a high intensity, which is related to a high density of states. Also the localized states (*in-gap states*) of the n-type semiconductor can be seen and are indicated. The gap between the valence band and the localized states, which are located at the edge of the conduction band can be determined as $E_{gap}$= 0.46 eV.

It was shown that the $Ti_xZr_yHf_zNiSn$ system is not a solid solution. The analogy of the composition of the stable phases is remarkable, but this can be explained by possible eutectics or peritectics in the quasi binary systems. Additionally, the analogy is not as surprisingly by taking the chemical relationship of titanium, zirconium and hafnium into account.

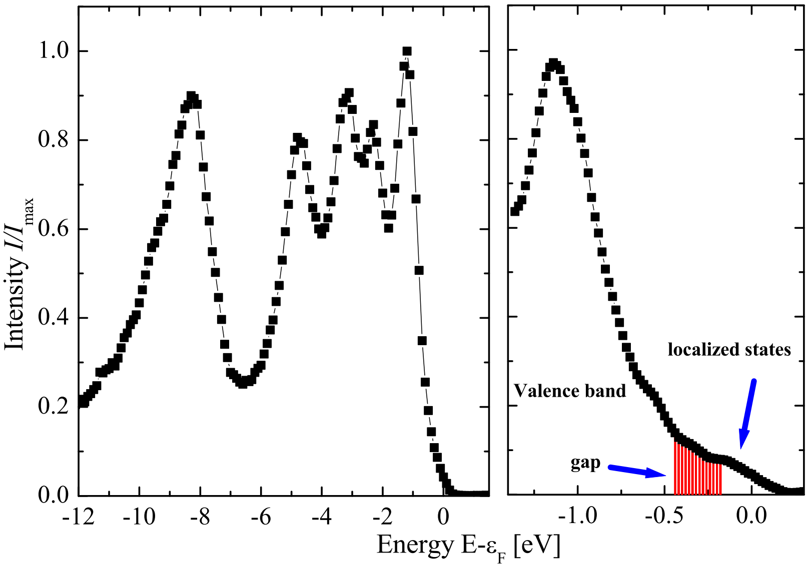

FIG. 103: Valence band (left) and Fermi energy (right) of $Ti_{0.21}Zr_{0.40}Hf_{0.39}NiSn$ measured by hard x-ray photoelectron spectroscopy.

### C. Element substitutions in the phase separated system $Ti_{0.5}Zr_{0.25}Hf_{0.25}NiSn$

The X-ray diffraction pattern (Fig.104) of the samples could be fitted by three Heusler phases with $C1_b$ structure (*216 ,F$\bar{4}$3m*), which exhibit very similar lattice parameters. The determined lattice parameter of the three phases are $a_1$= 5.989 Å, $a_2$= 6.029 Å and $a_3$=6.075 Å. In comparison to the lattice parameter of the ternary compounds TiNiSn a= 5.939 Å, ZrNiSn a= 6.121 Å and HfNiSn a= 6.091 Å it is possible to estimate the composition of the three phases qualitatively. The phase with the smallest lattice parameter $a_1$= 5.989 Å is very similar to the TiNiSn lattice parameter, what indicates a Ti-rich phase. The phase with the largest lattice parameter $a_3$= 6.075 Å seems to be a Hf-rich phase because of the very similar lattice parameter in comparison to the HfNiSn lattice parameter.

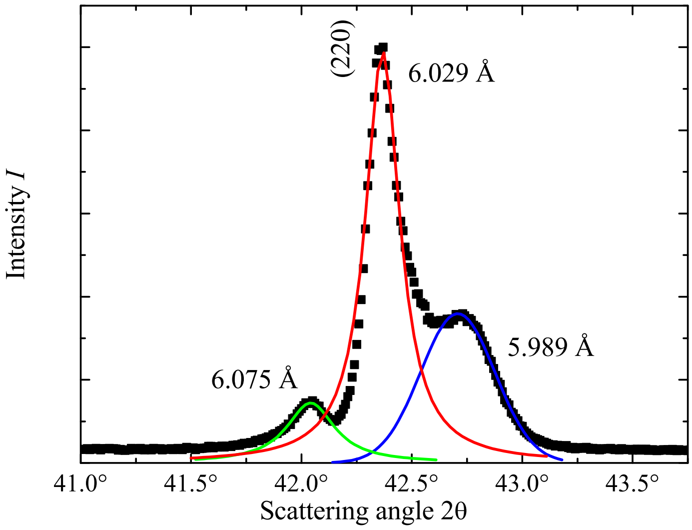

FIG. 104: (220) reflection measured by synchrotron radiation.

Figure 105 shows the element-specific EDX mappings of the $Ti_{0.5}Zr_{0.25}Hf_{0.25}NiSn$ compound. Brightness indicates high concentration of the respective constituent. These mappings are exemplary for all $Ti_{0.5}Zr_{0.25}Hf_{0.25}NiSn_{(1-x)}Z_x$ | Z: Sb, Bi, Te; x: 0-0.006 compounds. The elements-specific EDX mappings show that Zr, Sn and Ni is almost homogeneous distributed over the whole measurement area. In comparison to this, the Ti and Hf mappings behave complementary, forming a homogeneous decomposition. The shape of the precipitates indicates semicoherent interfaces, which fit well to the X-ray diffraction results showing

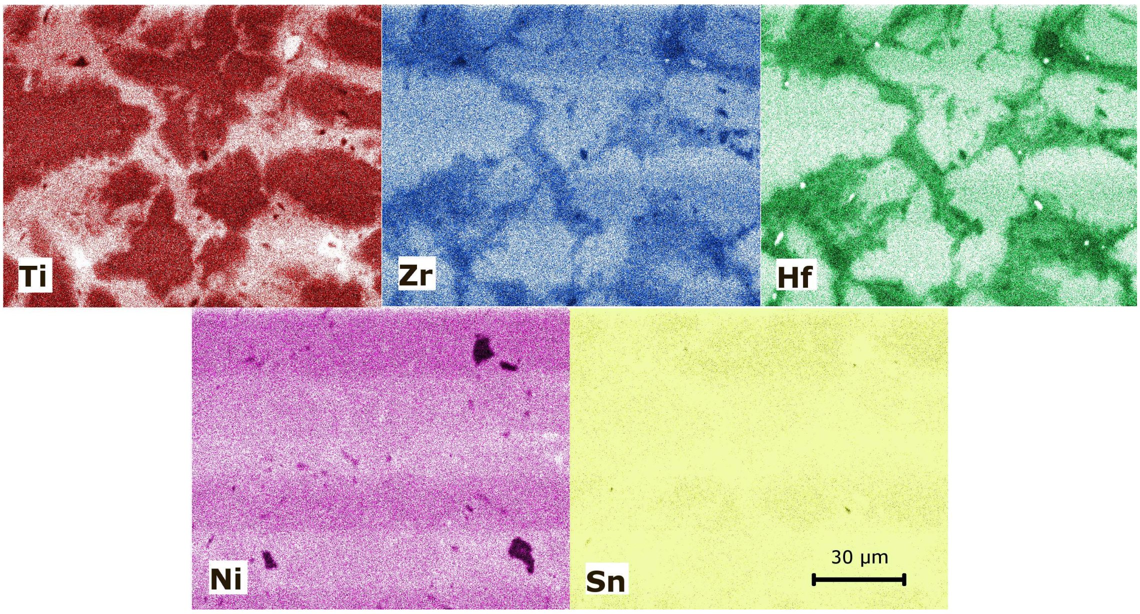

FIG. 105: Element-specific EDX mappings of the five constituents of the phase separated $\mathrm{Ti}_{0.5}\mathrm{Zr}_{0.25}\mathrm{Hf}_{0.25}\mathrm{NiSn}$ compound with brightness proportional to the concentration.

that at least three phases with the same crystal structure and similar lattice parameters are coexisting. Additionally, small bright spots are recognizable in the Hf mapping, which could be explained by small pure Hf inclusions. These Hf inclusions can act as possible nucleation seeds, which were formed first of all during the cooling process due to the high melting point of Hafnium. Above 1740°C Hafnium exhibits a bcc crystal structure (*229, $Im\bar{3}m$*, a= 3.615 Å[83]), what is convenient for the forming of the Heusler phases (lattice mismatch in Hf [111] direction ≈ 3 %).

In Figure 106 the temperature dependence of the resistivity measurements of the $\mathrm{Ti}_{0.5}\mathrm{Zr}_{0.25}\mathrm{Hf}_{0.25}\mathrm{NiSn}_{(1-x)}Z_x \mid Z=$ Sb, Bi, Te; $x=$ 0-0,006 samples is shown. The slightly discontinuous behavior at 400 K is a result of different contacting methods (PPMS: firmly bonded contacts, LSR: force-fitted contacts). The electrical resistivities of the parent phase, the 1‰ Sb sample and the 2‰ Bi sample show semiconducting behavior, i.e. resistivity decreases with increasing temperature. The resistivities of the 2‰ Sb and 2‰ Te doped samples show an almost temperature independent behavior and the 6‰ Sb sample clearly shows metallic behavior. With increasing antimony concentration the resistivity decreases due to the increasing carrier concentration - antimony exhibits one valence electron more then the substituted tin. In Figure 107 the dependence of the Seebeck coefficient on the electrical conductivity is shown. Except the 6‰ Sb sample, all antimony substituted samples exhibit the same development, what probably indicates the same electronic structure and that the changes in the electronic properties are only due to the increasing carrier concentration. To prove the influence of other elements on the carrier concentration, we substituted the antimony with bismuth, which is isoelectronic in comparison to antimony, but slightly bigger, and with tellurium, which exhibits one valence electron more and is smaller than the antimony atom. The 2‰ Bi sample shows semiconducting behavior, but a slightly higher resistivity than the 2‰ Sb sample. If the values of the Seebeck coefficients of the 2‰ Sb sample and the values of the 2‰ Bi sample are compared, there is almost no difference. That is because antimony and bismuth are isoelectronic and hence bismuth does not increase the carrier concentration. Thus the values of the Seebeck coefficient, which are sensitive to the carrier concentration, do not change. This can also be seen in Figure 107, the developing of the Seebeck coefficient in dependence on the electrical conductivity for both samples is almost the same, meaning that the mobility does not change and hence the electronic structure is almost the same. The development of the parent compound and the sample with 1‰ Sb are also almost the same, meaning that the electronic structure is the same and thus the change of the electronic properties is only dependent on the carrier concentration. The 2‰ Te substitution should increase the carrier concentration in comparison to the 2‰ Sb substitution, because tellurium exhibits one valence electron more than antimony. The influence of the higher carrier concentration in the 2‰ Te sample can be seen in the measurement of the Seebeck coefficient (see Figure 106), which drops down due to the higher carrier concentration. However, the development of the Te substituted sample in Figure 107 shows that the electronic structure is different to the Sb substituted sample, what can be seen by the different development. All resistivity measurements converge to the value of $\rho \approx 1\cdot 10^{-5}$Ohm·m at high temperatures. The difference between the highest and the lowest resistivity value of the antimony substituted samples is at 2 K three orders of magnitude, showing the huge impact of the Sb doping. The results of the Seebeck coefficient measurements show that all samples exhibit a negative Seebeck coefficient indicating $n$-type conduction (see Fig.106). The Seebeck coefficient of all antimony samples except the 6‰ Sb sample decrease until approximately 400 K. The 6‰ Sb sample shows a minimum in the Seebeck coefficient at 800 K. The minimum value of - 290 $\frac{\mu V}{K}$ at 400 K is exhibited by the sample with 1‰ Sb. Above a Sb value of 1‰ all values of the Seebeck

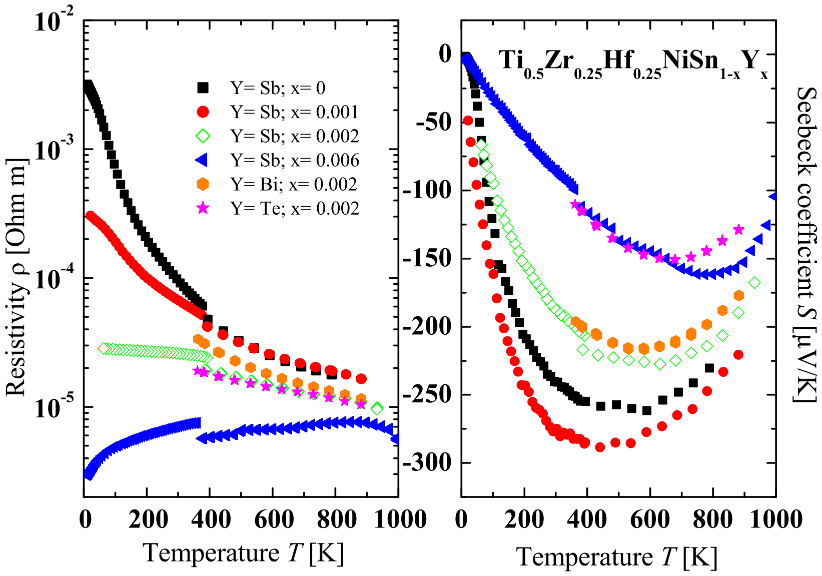

FIG. 106: Temperature dependence of the resistivity and Seebeck coefficient of the $Ti_{0.5}Zr_{0.25}Hf_{0.25}NiSn_{(1-x)}Y_x$ compounds.

coefficient increase with increasing Sb concentration. This can be explained by the creation of sharp states very close to the Fermi energy due to the distortion of the lattice of the parent phase.[5, 31, 38, 58–62] These sharp states lead to a high Seebeck coefficient, because the Seebeck coefficient depends on the density of states close to the Fermi energy and on the developing of the band near the Fermi energy.[24] The values of the Seebeck coefficient of all antimony samples increase above 500 K, due to the increasing electrical conductivity. The Seebeck coefficient of the tellurium sample decreases until 650 K and exhibit a value in the same order of magnitude like the 6‰ Sb sample. The Seebeck coefficient of the 2‰ bismuth substituted sample shows almost the same behavior as the 2‰ Sb sample. As mentioned above the influence of the higher carrier concentration in the tellurium substituted sample is obvious in the measurements of the Seebeck coefficient, recognizable by the higher value of the Seebeck coefficients in comparison with the 2‰ Sb sample.

Figure 108 shows the temperature dependence of the thermal conductivity. The decreasing thermal conductivity at high temperatures shows the for Umklapp process typical 1/T behavior until approximately 700 K. At temperatures above 700 K the thermal conductivity of all sample increases due to higher contributions of the electronic thermal conductivity (see

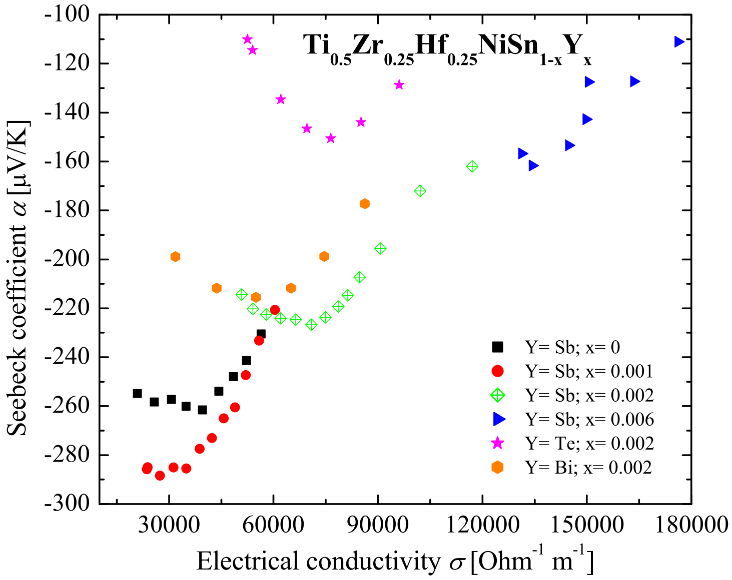

FIG. 107: Electrical conductivity dependence of the Seebeck coefficient of the $Ti_{0.5}Zr_{0.25}Hf_{0.25}NiSn_{(1-x)}Y_x$ compounds.

Figure 109) . The samples with 6‰ Sb and 2‰ Te exhibit higher thermal conductivities at room temperature in comparison to all the other samples which exhibit almost the same value at room temperature. This result for the 6‰ Sb sample can be explained by a higher resistivity and thereby the higher electronic contribution to the thermal conductivity. Concerning the 2‰ Te sample the results are explainable by the higher lattice thermal conductivity. The lattice thermal conductivity of the parent compound exhibits the highest value in comparison to the Sb substituted samples, because the structure is not disturbed by the Sb substitution. The especially low thermal conductivity of the 2‰ Sb substituted samples is the consequence of the phase separation combined with a structural disorder due to the substitution, which produces additional phonon scattering, and the moderate resistivity. The lattice thermal conductivity of the Te and Bi substituted sample are in the same order of magnitude of the parent sample. The Te substituted sample exhibits the highest lattice thermal conductivity of all samples possibly due to the small atomic size, leading to lower distortion. The increase of the lattice thermal conductivity of the 1‰ Sb, 2‰ Te and 2‰ Bi are due to the bipolar diffusion.[36] The combined results of the Seebeck coefficients, the resistivities and the thermal conductivities lead to high values for the Figure of Merit

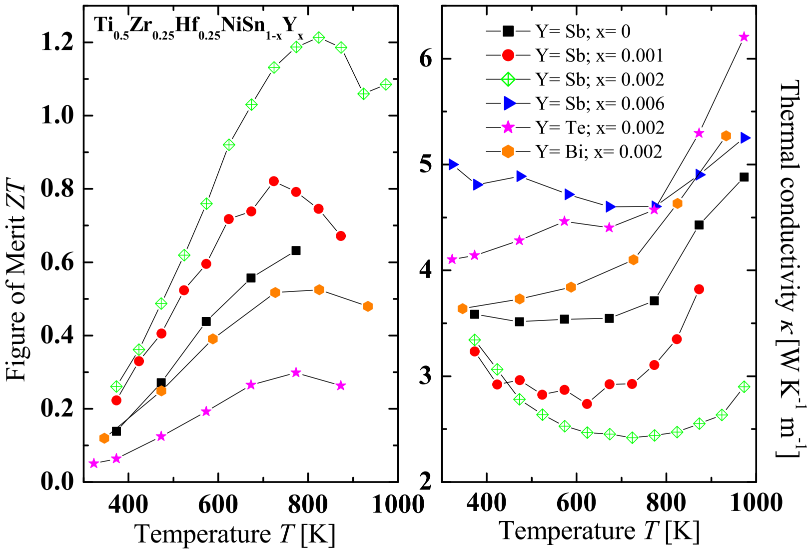

FIG. 108: Temperature dependence of the Figure of Merit and the thermal conductivity of the $\mathrm{Ti_{0.5}Zr_{0.25}Hf_{0.25}NiSn_{(1-x)}}Y_x$ compounds.

(see Figure 108). The maximum value is exhibited by the sample with 2‰ Sb with ZT = 1.2 at 830 K.

In summary, it has been shown that the high Figure of Merit values reported by Shutoh et al.[76] could almost be reproduced. The origin of the exceptional low thermal conductivity is the decomposition in the compounds, which does not influence the electrical conductivity significantly because of semi-coherent interfaces between the three coexisting Heusler phases. These intrinsic properties of the $\mathrm{Ti_{0.5}Zr_{0.25}Hf_{0.25}NiSn_{(1-x)}}Z_x \mid Z=$ Sb, Bi, Te; $x=$ 0-0.006 system show that Heusler compounds are competitive in matters of the transport properties and exhibit mechanical properties, which exceed the once of the most common thermoelectric materials (hardness ≈ 900VH1 [15]). Additionally, it has been shown that the Heusler compounds are tunable by doping with several elements, what allows designing the material for a suggested application.

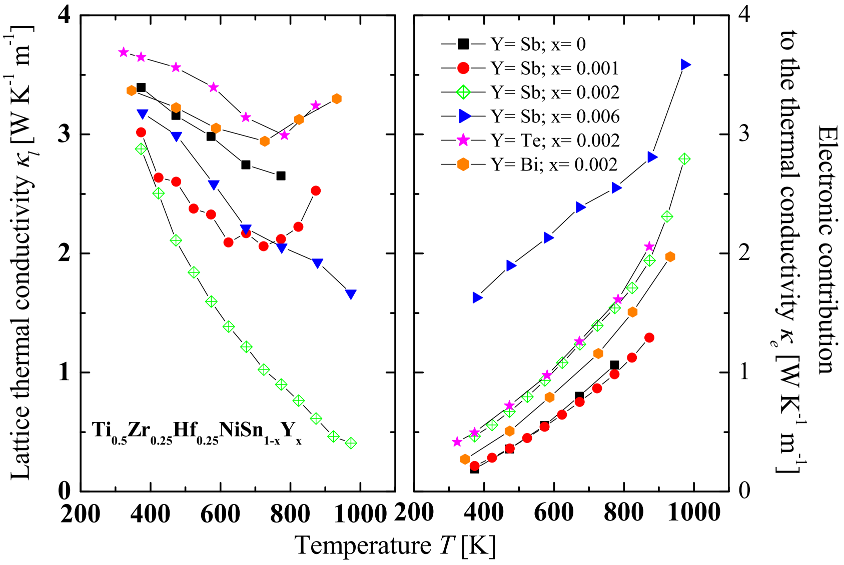

FIG. 109: Temperature dependence of the lattice thermal conductivity and the electronic contribution to the thermal conductivity of the phase separated $\mathrm{Ti}_{0.5}\mathrm{Zr}_{0.25}\mathrm{Hf}_{0.25}\mathrm{NiSn}_{(1-x)}Y_x$ compounds.

# V. CONCLUSION

In the first part (chapter A) of this work the influence of element substitutions on the system $Zr_{0.5}Hf_{0.5}NiSn$ was investigated. The Zr/Hf position was substituted with V, Nb, Mn and the Ni position with Ag to improve the n-type thermoelectric behavior. The Sc, Y and Al substitutions were done to produce a p-type thermoelectric material. This was supposed to show the benefit that the thermoelectric pair (n-type and p-type material) exhibits the same mechanical properties, e.g. thermal expansion coefficient or hardness, which simplifies the implementation of the Heusler materials in a thermoelectric module. Additionally, the industrial up-scaling would be easier, because of the same process parameter, e.g. heat treatment or melting point. The substitutions on the Zr/Hf position lead to improvements of the thermoelectric properties, e.g. the vanadium substitution increased the values for the Figure of Merit by a factor of 4 and the niobium substitutions by a factor of 5. The substitutions with scandium and yttrium caused p-type semiconducting behavior, as expected the Figure of Merit was still not comparable with the values for the n-type materials. In all samples, except the p-type conducting samples, high values for the Seebeck coefficient are obtained at low substitution concentrations, what can be explained by the creation of resonant levels or *in-gap states* in the conduction band next to the Fermi energy.[58, 59] These states produce a high density of states next to the Fermi energy, which lead into high values of the Seebeck coefficient. This phenomenon is reported in several publications [16, 84, 85] and is easy to apply to other Heusler compounds. Altogether, the substitution is an effective method to optimize the electronic properties of Heulser compounds.

In chapter B the $Ti_xZr_yHf_zNiSn$ system was investigated. After the reproduction of several samples from the literature consisting of $Ti_xZr_yHf_zNiSn$, it was recognized that these samples show a phase separation.[76, 77] The intention was to determine the origin of these phase separations and to use this knowledge afterwards for a controlled reduction of the thermal conductivity. The results of this investigation are very interesting. In every quasi binary system, e.g. $Ti_{(1-x)}Hf_xNiSn$, three different compositions are stable Heusler phases. Altogether twelve stable phases plus the three parent phases were obtained in the $Ti_xZr_yHf_zNiSn$ system and a Gibbs triangle for 950°C was constructed (see Figure 97). The transport properties of all synthesized samples were determined and they show that the pure Heusler phases exhibit high values of the Seebeck coefficient and semiconducting behavior of the resistivity.

Additionally, hard x-ray photoelectron spectroscopy measurements show high crystallinity recognizable by the high density of states next to the Fermi energy, which causes the high values of the Seebeck coefficient, and the missing *in-gap states* or resonant levels, which were produced by impurities, structural stress or disorder (see Figure 103). A second remarkable result of the transport properties is that the phase decomposition of two Heusler phases can significantly reduce the thermal conductivity without destructing the electronic properties. It was also shown that phase separations with one Heusler phase and another binary phase destroy the thermoelectric properties. Overall, the stable Heusler phases in the $Ti_xZr_yHf_zNiSn$ system can be synthesized and exhibit transport properties, which are expected for samples with high crystallinity and low disorder, what is also indicated by the relative high thermal conductivity (see Figure 102).

In chapter C the phase separated compound $Ti_{0.5}Zr_{0.25}Hf_{0.25}NiSn$ was optimized by substitutions on the tin position, which exhibit an improved thermal conductivity. The dependency of the electronic properties on the substitution is recognizable and improves the thermoelectric properties. A maximum value of the Figure of Merit $ZT = 1.2$ at 830 K was achieved at a substitution of 2‰ Sb on the tin position. This is up to now the highest reported and reproduced ZT value of a Heusler compound in the literature.

## VI. OUTLOOK

The main disadvantage of Heusler compounds still is the high lattice thermal conductivity. Heusler compounds with $C1_b$ structure usually exhibit high electrical conductivities in comparison to other thermoelectric materials and moderate values for the Seebeck coefficient. One suggestion to reduce the thermal conductivity is to apply a phase decomposition on the thermoelectric system, which causes additional phonon scattering at the grain boundaries. In the most cases the size of the decomposition is hard to control and it is not temperature stable. Another thought is to implement a nanostructure by powdering the thermoelectric material followed by a sintering step via spark plasma sintering or hot-pressing. The drawback of this method is that in almost all cases the nanostructure vanishes during heat treatment or one thermoelectric cycle. This is caused by grain coarsening, which is a typical phenomenon [9], but decreases the thermoelectric efficiency with every thermoelectric cycle. The results from this work enable to combine the advantages of both methods described above. The idea is to produce two of the thermodynamic stable Heusler phases with adequate electronic properties separately. The next step is to pulverize the samples with a determined particle size, e.g. nano particles via high energy mechanical alloying. After the pulverization the two stable phases are mixed in a certain ratio and sintered by the spark plasma sintering process. The advantage of this method is that the phase decomposition can be controlled by the particle size of the synthesized Heusler phases and the ratio of the two Heusler phases. Another advantage is that due to the fact that two thermodynamic stable Heusler phases are present in the new composite sample, the grain coarsening is reduced or vanishes completely. The third advantage is that this method could easily be up scaled for industrial processes. The idea to produce a Heusler composite material consisting of the determined stable Heusler phases allows to synthesize composite Heusler materials with demanded properties. It is possible to mix two or more different Heusler phases to produce the determined micro or nano structure, which leads to designated transport properties for industrial applications. This is not constricted to thermoelectric materials, in principle this method can also be used for other applications.

## Acknowledgments

---

## Appendix A: Curriculum vitae

# *Curriculum Vitae*

Michael Schwall
Schillstraße 74
55131 Mainz

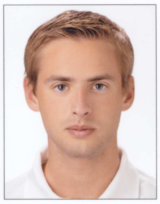

## Personal data

**Date of birth:** 14.08.1986

**Place of birth:** Mayen

**Nationality:** German

**Phone:** 01713285622

**E-mail:** schwall@uni-mainz.de

## Experience

Since 05/2010

**Scientific assistant** (Johannes-Gutenberg University, Mainz)

- Ph.D student in solid state chemistry (Group of Prof. Dr. Felser)
- Main topic: Heusler compounds with $C1_b$ structure for thermoelectric applications
- Person in charge for the "thermoHeusler" Project of the German Federal Ministry of Economics and Technology (BMWi)
- Two research stays at Spring-8 in Japan in line with the research unit ASPIMATT (2010/2012)

- Research stay at the Nanyang Technological University in Singapore (Prof. Dr. Ramanujan)

## Education

| | |
|---|---|
| 05/2010 –<br>approx. 10/2012 | **Ph.D. study in chemistry** (Johannes-Gutenberg University, Mainz)<br>• Member of the graduate school „Materials in science in Mainz“ (MAINZ) |
| 10/2005 - 04/2010 | **Diploma study in chemistry** (Johannes-Gutenberg University, Mainz)<br>▪ Diploma thesis in inorganic chemistry: "Heusler Verbindungen mit $C1_b$-Struktur als thermoelektrische Materialien" |
| 05/2009 – 10/2009 | **Student assistant** (Johannes-Gutenberg University, Mainz)<br>▪ Inorganic chemistry, Group Prof. Dr. Felser |
| 11/2008 – 04/2009 | **Student assistant** (Institut für Mikrotechnik Mainz (IMM), Mainz)<br>▪ Catalyse technique |
| 04/2005 – 09/2006 | **Military service** (Bad Segeberg, Mainz)<br>▪ First part: 04/2005 – 10/2005 at the Panzergrenadierbatallion 182 in Bad Segeberg<br>▪ Second part: 02/2006 – 04/2006 at the Panzergrenadierbatallion 182 in Bad Segeberg<br>▪ Third part: 08/2006 – 09/2006 at the Feldjägerbatallion 251 in Mainz |
| 08/1996 – 03/2005 | **General qualification for university entrance** (Megina-Gymnasium, Mayen) |

# *Curriculum Vitae*

## Skills

### Languages

German native speaker
Fluent in English

### Computer skills

Comprehensive knowlege of  MS Office and MS Windows
Basic Knowlege of Mac OS and Linux

## Activities

Sports (Sailing), Music

## Publications

- M.Schwall, J.M. Stahlhofen, and B.Balke, Exploring resonant levels in the Half-Heusler $Zr_{0.5}Hf_{0.5}NiSn$ system, Phys. Rev. B, submitted

- S. Ouardi, G. H. Fecher, C. Felser, M. Schwall, S. S. Naghavi, A. Gloskovskii, B. Balke, J. Hamrle, K. Postava, J. Pistora, et al., Electronic structure and optical, mechanical, and transport properties of the pure, electron-doped, and hole-doped Heusler compound CoTiSb, Phys. Rev. B **86**, 045116 (2012).

- M. Schwall, L. M. Schoop, S. Ouardi, B. Balke, C. Felser, P. Klaer, and H. J. Elmers, Thermomagnetic properties improved by self-organized flower-like phase separation of ferromagnetic $Co_2Dy_{0.5}Mn_{0.5}Sn$, Adv. Funct. Mater. 2012, **22**, 1822–1826.

- T. Jaeger, C. Mix, M. Schwall, X. Kozina, J. Barth, B. Balke, M. Finsterbusch, Y. U. Idzerda, C. Felser, and G. Jakob, Epitaxial growth and thermoelectric properties of TiNiSn and $Zr_{0.5}Hf_{0.5}NiSn$ thin films, Thin Solid Films **520** (2011) 1010–1014.

- M. Schwall, and B. Balke, Niobium substitution in $Zr_{0.5}Hf_{0.5}NiSn$ based Heusler compounds for high power factors, Appl. Phys. Lett. **98**, 042106 (2011).

- B. Balke, J. Barth, M. Schwall, G. H. Fecher, and C. Felser, An Alternative Approach to Improve the Thermoelectric

Properties of Half-Heusler Compounds, J. Electron. Mater. **40**, 702 (2011).

- S. Ouardi, G. H. Fecher, B. Balke, M. Schwall, X. Kozina, G. Stryganyuk, C. Felser, E. Ikenaga, Y. Yamashita, S. Ueda, and K. Kobayashi, Thermoelectric properties and electronic structure of substituted Heusler compounds: $\mathrm{NiTi}_{0.3-x}\mathrm{Sc}x\mathrm{Zr}_{0.35}\mathrm{Hf}_{0.35}\mathrm{Sn}$, Appl. Phys. Lett. **97**, 252113 (2010).

**Conference contributions**

- International conference on thermoelectrics (ICT) 2010, Shanghai, China, poster presentation
- European conference on thermoelectrics (ECT) 2010, Como, Italy, oral presentation
- Annual spring meeting of the german physical assosication (DPG) 2011, Dresden, Germany, oral presentation
- Spring meeting of the european material research society (EMRS) 2011, Nice, France, oral and poster presentation
- International conference on thermoelecetrics (ICT) 2011, Traverse City, MI, USA, oral presentation
- HAXPES meeting 2011, Hamburg, Germany, poster presentation
- Annual spring meeting of the german physical assosication (DPG) 2012, Berlin, Germany, oral and poster presentation
- International and european conference on thermoelecetrics (ICT/ECT) 2012, Aalborg, Denmark, poster presentation
- 16th Meeting of the professional group of solid state chemistry and material science of the assosiaction of german chemists (GdCh) 2012, Darmstadt, Germany, poster presentation

Mainz, 26.09.2012

APPLIED PHYSICS LETTERS **98**, 042106 (2011)

# Niobium substitution in $Zr_{0.5}Hf_{0.5}NiSn$ based Heusler compounds for high power factors

Michael Schwall and Benjamin Balke[a)]
*Institut für Anorganische und Analytische Chemie, Johannes Gutenberg-Universität, 55099 Mainz, Germany*

(Received 23 December 2010; accepted 6 January 2011; published online 26 January 2011)

This work reports on the structural and physical properties of the Heusler alloy $(Zr_{0.5}Hf_{0.5})_{1-x}Nb_xNiSn$ with varying Nb concentrations. The structure of the $(Zr_{0.5}Hf_{0.5})_{1-x}Nb_xNiSn$ solid solution was investigated by means of X-ray diffraction. It is found that the alloys exhibit the $C1_b$ structure for all Nb concentrations. The physical properties were studied using the physical properties measurement system from low temperature to room temperature. It was shown that the thermoelectric properties like the dimensionless Figure of Merit are increased five times by substituting $(Zr_{0.5}Hf_{0.5})$ with Nb to 0.09 at 300 K and the Powerfactor is increased 10 times to 1.8 mW/K$^2$ m at 300 K. © *2011 American Institute of Physics*. [doi:10.1063/1.3548867]

Heusler compounds[1] with a $C1_b$ structure, frequently referred to as the half-Heusler compounds, have received much attention as potential materials for thermoelectric applications.[2–6] Because of their mechanical and thermal stability, these compounds exhibit more advantages compared to the common thermoelectric materials like $Bi_2Te_3$, SiGe, clathrates, and filled skutterudites. Another advantage is that these compounds with the general formula $XYZ$ ($X,Y$ =transition metal, $Z$=main group element) are tunable, which means that expensive and toxic elements can be avoided to use. The usually high electrical conductivity $\sigma$ of the half-Heusler compounds yields into a high Powerfactor. The main problem of the half-Heusler compounds is the high lattice thermal conductivity. Hohl *et al.* reported that mass disorder in the $X$-site lattice causes additional phonon scattering, and thereby reduces the thermal conductivity.[7,8] The aim of this work was to improve the thermoelectric properties of $Zr_{0.5}Hf_{0.5}NiSn$, especially the Powerfactor. The half-Heusler compounds exhibit high Powerfactors in comparison with other thermoelectric materials like Co-349 compounds (0.3 mW/K$^2$ m),[9,10] $Zn_4Sb_3$(0.6 mW/K$^2$ m),[11] skutterudites $CeFeCo_3Sb_{12}$(0.1 mW/K$^2$ m),[12] and $Ag_{1-x}Pb_{10}Sb(Bi)Te_{12}$ (1.7 mW/K$^2$ m).[13] Only $Bi_2Te_3$ (4 mW/K$^2$ m),[14] which is toxic and exhibits a low melting point (≈750 K),[15] and $NaCo_2O_4$ (5 mW/K$^2$ m),[16] which exhibits a highly anisotropic between in- and out-of-plane direction in the resistivity, have better Powerfactors at room temperature. We tried to improve the resistivity of the $Zr_{0.5}Hf_{0.5}NiSn$ half-Heusler compound by substituting the $X$-site lattice with Nb. The reason for this was to increase the carrier concentration $n$ to find the optimal carrier concentration.[17]

The $(Zr_{0.5}Hf_{0.5})_{1-x}Nb_xNiSn$ samples with varying $x$ in steps of 0.01 were prepared by arc melting of stoichiometric amounts of the constituents in an argon atmosphere of $10^{-4}$ mbars. The resulting polycrystalline ingots were annealed at about 1100 K in an evacuated quartz tube for 7 days afterwards. This procedure resulted in samples exhibiting the $C1_b$ structure.

The crystalline structure was determined by X-ray powder diffraction (XRD) using excitation by Cu K$_\alpha$ radiation. Typical powder diffraction patterns are shown in Fig. 1. All samples from this series exhibit the $C1_b$ structure. The lattice parameter $a$ found from the Rietveld refinements are: For the unsubstituted, $a$=6.1082 Å; for 1% Nb, $a$=6.094 Å; for 2% Nb, $a$=6.099 Å; for 3% Nb, $a$=6.099 Å; for 4% Nb, $a$ =6.097 Å; and for 5% Nb, $a$=6.095 Å. From these results, it is possible to recognize a dependence of the lattice parameter from the Niobium concentration. Except for the lattice parameter for 1% Nb, all lattice parameters support substituting larger Zr/Hf atoms with Nb atoms. The new reflections that appear on the left side of the main one could be identified as $Ni_2Zr_{0.5}Hf_{0.5}Sn$. The new reflections that appear on the right side of the main one belong to a $Ni_{1.35}Sn$ impurity. The impurities of each sample are together below 5%.

The physical properties were investigated by the physical properties measurement system (PPMS, Quantum Design, San Diego, CA). In Fig. 2, the measured physical properties of the $(Zr_{0.5}Hf_{0.5})_{1-x}Nb_xNiSn$ samples are compared with the unsubstituted $Zr_{0.5}Hf_{0.5}NiSn$. The thermal conductivity $\kappa$ of the unsubstituted $Zr_{0.5}Hf_{0.5}NiSn$ has the lowest value. This could be partially explained by the low electrical

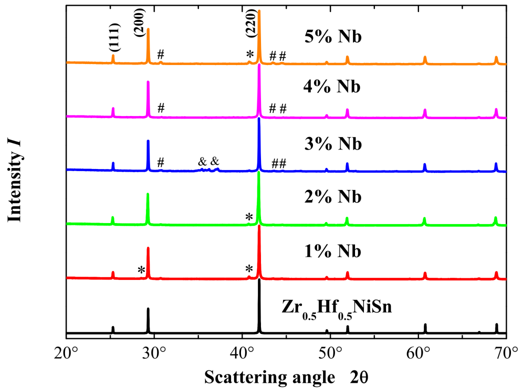

FIG. 1. (Color online) Powder diffraction of $(Zr_{0.5}Hf_{0.5})_{1-x}Nb_xNiSn$ and the simulated powder pattern of $Zr_{0.5}Hf_{0.5}NiSn$. Shown are the powder patterns measured with Cu K$_\alpha$ at room temperature for the compounds with $x$ =0.01–0.05. The impurities are marked: $Ni_2Zr_{0.5}Hf_{0.5}Sn$ (*), $Ni_{1.35}Sn$ (#), and $Hf_5Sn_4$ (&).

---

[a)] Electronic mail: balke@uni-mainz.de.

0003-6951/2011/98(4)/042106/3/$30.00

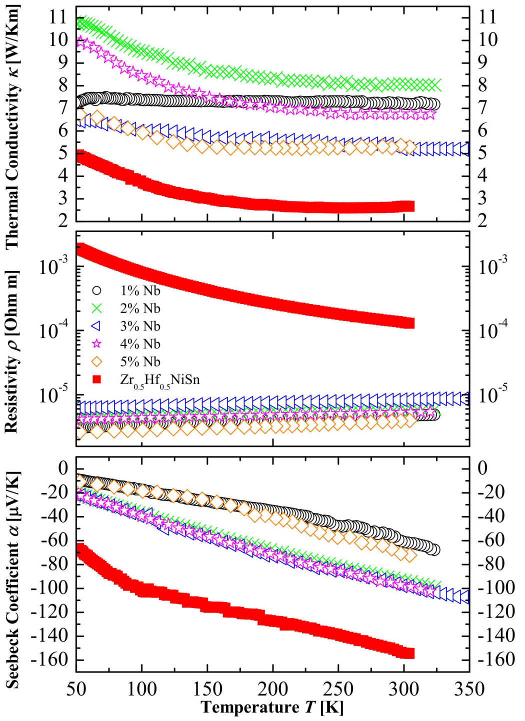

FIG. 2. (Color online) Physical properties of $(Zr_{0.5}Hf_{0.5})_{1-x}Nb_xNiSn$. Shown is the temperature dependence of the thermal conductivity, the Seebeck coefficient, and the resistivity. To compare the substituted $(Zr_{0.5}Hf_{0.5})_{1-x}Nb_xNiSn$ samples, the properties of $Zr_{0.5}Hf_{0.5}NiSn$ are plotted.

resistivity $\rho$ of the substituted compounds, which is almost two orders of magnitude higher than the unsubstituted compound and is directly related to the thermal conductivity through the Wiedemann–Franz Law

$$\kappa = \kappa_e + \kappa_l \tag{1}$$

and

$$\kappa_e = L\sigma T = \frac{LT}{\rho} = ne\mu LT, \tag{2}$$

where $L$ is the Lorenz number, $n$ is the carrier concentration, $e$ is the elementary charge, and $\mu$ is the mobility.

The increase of the electrical conductivity $\sigma$ by substituting the $(Zr_{0.5}Hf_{0.5})$ with Nb is the expected behavior because the carrier concentration is increased, and with it, the electrical conductivity. The substitution of $(Zr_{0.5}Hf_{0.5})$ with Nb is so strong that it changes the temperature dependence of the resistivity from a semiconducting behavior to metallic (see Fig. 2, middle panel). The sign of the Seebeck coefficient was negative for all samples in the temperature range from 50 to 300 K, which indicates $n$-type conduction. The comparison of the Seebeck coefficient $S$ of the $(Zr_{0.5}Hf_{0.5})_{1-x}Nb_xNiSn$ samples with the unsubstituted sample shows that the absolute values of the substituted samples are much lower. This is due to the higher carrier concentration. The Seebeck coefficient shows a monotonous dependence of the Niobium concentration until 5% Nb. This is the point at which the carrier concentration is so high that the Seebeck coefficient is decreased. Because of this, the resistivity for 5% Nb is the lowest of all samples. The other samples do not show a dependence of the resistivity or the thermal conductivity on the Niobium concentration; this could be explained by different grain sizes. The resistivity and thermal conductivity are very sensitive to the size of the grains because of the electrical and thermal scattering effects.

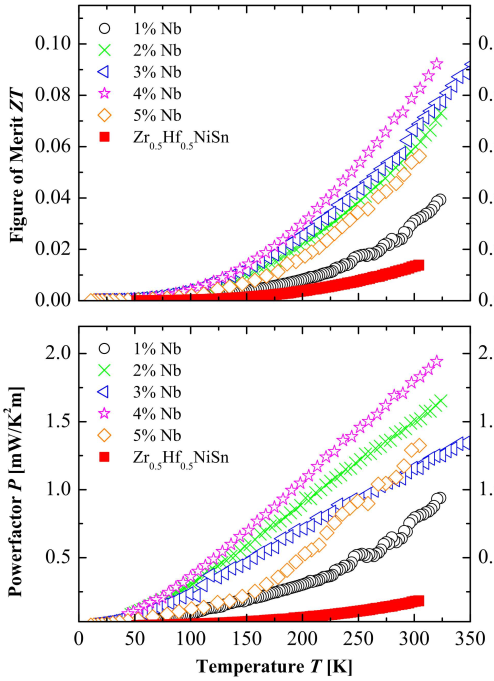

FIG. 3. (Color online) Thermoelectric quality factors of $(Zr_{0.5}Hf_{0.5})_{1-x}Nb_xNiSn$. Shown is the temperature dependence of the Figure of Merit and the Powerfactor. To compare the substituted $(Zr_{0.5}Hf_{0.5})_{1-x}Nb_xNiSn$ samples, the properties of $Zr_{0.5}Hf_{0.5}NiSn$ are plotted.

Figure 3 displays the dimensionless Figure of Merit and the Powerfactor $P$ calculated from the measured physical properties. The used equations are the following.

$$ZT = \frac{\sigma S^2}{\kappa} T = \frac{S^2}{\kappa\rho} T \tag{3}$$

and

$$P = \sigma S^2 = \frac{S^2}{\rho}. \tag{4}$$

In Fig. 3, the Figure of Merit of the unsubstituted $Zr_{0.5}Hf_{0.5}NiSn$ is set as a benchmark for the Nb substituted samples. The values of the dimensionless Figure of Merit of all samples increase with increasing temperature. All $ZT$ values of the substituted samples are higher than the unsubstituted. This is due to the higher electrical conductivity in all substituted samples; except for the sample with $x=0.05$, the Figure of Merit increases with the amount of Niobium. The maximum of the Figure of Merit is reached at $x=0.04$ Nb concentration with a value of 0.09 at 300 K. The fact is that the substituted samples exhibit higher *ZT* values as the unsubstituted sample is even bigger in the values of the Powerfactor. The highest value for the Powerfactor exhibits the sample with $x = 0.04$, which reaches a value of 1.8 $\mathrm{mW/K^2\,m}$ at 300 K. The determining factor of the high Powerfactors is the high electrical conductivity.

In summary, it has been shown that small substitutions of the $Zr_{0.5}Hf_{0.5}NiSn$ system can improve the thermoelectric properties. The best value for the substitution with Nb was found at $x = 0.04$ for the $(Zr_{0.5}Hf_{0.5})_{1-x}Nb_xNiSn$ series. Beyond this concentration of Nb, the thermoelectric properties are decreasing again due to the too much increased carrier concentration. The values of the dimensionless Figure of Merit *ZT* and the Powerfactor *P* of the sample with $x = 0.04$ were improved by the factors of 5 and 10 in comparison with the $Zr_{0.5}Hf_{0.5}NiSn$ sample, respectively.

The authors gratefully acknowledge the financial support by the "thermoHeusler" Project (Grant No. 0327876D) of the German Federal Ministry of Economics and Technology (BMWi).

[1] F. Heusler, Verhandl. DPG **5**, 219 (1903).
[2] S. Ouardi, G. H. Fecher, B. Balke, X. Kozina, G. Stryganyuk, C. Felser, S. Lowitzer, D. Ködderitsch, H. Ebert, and E. Ikenaga, Phys. Rev. B **82**, 085108 (2010).
[3] J. Barth, G. H. Fecher, B. Balke, S. Ouardi, T. Graf, C. Felser, A. Shkabko, A. Weidenkaff, P. Klaer, H. J. Elmers, H. Yoshikawa, S. Ueda, and K. Kobayashi, Phys. Rev. B **81**, 064404 (2010).
[4] B. Balke, S. Ouardi, T. Graf, J. Barth, C. G. F. Blum, G. H. Fecher, A. Shkabko, A. Weidenkaff, and C. Felser, Solid State Commun. **150**, 529 (2010).
[5] T. Graf, J. Barth, B. Balke, S. Populoh, A. Weidenkaff, and C. Felser, Scr. Mater. **63**, 925 (2010).
[6] C. Felser, G. H. Fecher, and B. Balke, Angew. Chem., Int. Ed. **46**, 668 (2007).
[7] H. Hohl, A. Ramirez, W. Kaefer, K. Fess, C. Thurner, C. Kloc, and E. Bucher, Mater. Res. Soc. Symp. Proc. **478**, 109 (1997).
[8] H. Hohl, A. P. Ramirez, C. Goldmann, G. Ernst, B. Wölfing, and E. Bucher, J. Phys.: Condens. Matter **11**, 1697 (1999).
[9] M. Prevel, S. Lemonnier, Y. Klein, S. Hbert, B. Ouladdiaf, J. G. Noudem, and D. Chateigner, J. Appl. Phys. **98**, 093706 (2005).
[10] E. Guilmeau, R. Funahashi, M. Mikami, K. Chong, and D. Chateigner, Appl. Phys. Lett. **85**, 1490 (2004).
[11] T. Caillat, J.-P. Fleurial, and A. Borshchevsky, J. Phys. Chem. Solids **58**, 1119 (1997).
[12] B. C. Sales, D. Mandrus, and R. K. Williams, Science **272**, 1325 (1996).
[13] K. F. Hsu, S. Loo, F. Guo, W. Chen, J. S. Dyck, C. Uher, T. Hogan, E. K. Polychroniadis, and M. G. Kanatzidis, Science **303**, 818 (2004).
[14] T. Caillat, M. Carle, P. Pierrat, H. Scherrer, and S. Scherrer, J. Phys. Chem. Solids **53**, 1121 (1992).
[15] C. B. Satterthwaite and R. W. Ure, Jr., Phys. Rev. **108**, 1164 (1957).
[16] I. Terasaki, Y. Sasago, and K. Uchinokura, Phys. Rev. B **56**, R12685 (1997).
[17] G. J. Snyder and E. S. Toberer, Nature Mater. **7**, 105 (2008).

ADVANCED FUNCTIONAL MATERIALS
www.afm-journal.de

# Thermomagnetic Properties Improved by Self-Organized Flower-Like Phase Separation of Ferromagnetic $Co_2Dy_{0.5}Mn_{0.5}Sn$

*Michael Schwall, Leslie M. Schoop, Siham Ouardi, Benjamin Balke,* Claudia Felser, Peter Klaer, and Hans-Joachim Elmers*

**A thermodynamically stable phase separation of $Co_2Dy_{0.5}Mn_{0.5}Sn$ into the Heusler compound $Co_2MnSn$ and $Co_8Dy_3Sn_4$ is induced by rapid cooling from the liquid phase. The phase separation forms an ordered flower-like structure on the microscale. The increased scattering of phonons at the phase boundaries reduces the thermal conductivity and thus improves thermoelectric and spincaloric properties.**

## 1. Introduction

Spincalorics, a field of research that has recently attracted a lot of interest, exploits pure spin currents induced by a thermal gradient.[1–5] Thus it promises the development of a new class of spintronic devices. In addition to a large Seebeck coefficient, a low thermal conductivity is an important physical property that has to be optimized in the course of development of advanced materials for spincalorics.

Heusler compounds with $C1_b$ or $L2_1$ structure have received much attention for thermoelectric and spincaloric applications.[6–12] The advantages of those compounds are their mechanical and thermal stability and the possibility of tailoring their physical properties via band-structure tuning.[13,14] This tuning can be realized by partial substitution of elements in the parent phase or by adding small amounts of elements into the existing compound.[13,15–17]

A characteristic property of the Heusler compounds is their high electrical conductivity, which leads on the one hand to a high power factor and on the other hand to a large thermal conductivity according to the Wiedemann–Franz law.[13,18] The main obstacle for the use of Heusler compounds in spincaloric applications is their high lattice thermal conductivity, which must be reduced to achieve a large figure-of-merit. Several approaches to reduce the lattice thermal conductivity have been proposed. Hohl et al. reported that mass disorder in the X-site lattice causes additional phonon scattering and thereby reduces the thermal conductivity.[19,20] Another approach is the creation of a nano- or microstructure in the sample by increasing the number of grain boundaries, for example by sintering of nanoparticles, by inducing a fine-grained phase separation by rapid quenching or by introducing nanoinclusions.[21–27] The challenge of this approach is to preserve structural stability over a wide temperature range. In many inhomogeneous compounds the grains of the polycrystalline sample tend to grow at higher temperatures and with increasing time. This grain coarsening reduces the grain boundaries and increases the thermal conductivity. We have achieved thermal stability in the phase separated ferromagnetic compound $Co_2Dy_{0.5}Mn_{0.5}Sn$ and show that the lattice conductivity is decreased by a factor of two due to the occurence of well-ordered flower-like phase separated structures on a very small length scale.

## 2. Results

### 2.1. Structural Properties

In **Figure 1** the X-ray diffraction (XRD) pattern of $Co_2Dy_{0.5}Mn_{0.5}Sn$ is shown. Almost all reflections of the XRD pattern can be described by the reflections of $Co_2MnSn$ (*225, Fm-3m*) and $Co_8Dy_3Sn_4$ (*186, $P6_3mc$*). The lattice parameter of the $Co_2MnSn$ phase is $a = 5.950$ Å and the lattice parameters of the $Co_8Dy_3Sn_4$ phase are $a = b = 8.844$ Å and $c = 7.518$ Å, which fit well with the literature data.[28]

### 2.2. Phase Separation

**Figure 2**a shows the distribution of elements in the phase-separated $Co_2Dy_{0.5}Mn_{0.5}Sn$ compound, which form a sixfold

---

M. Schwall, L. M. Schoop,
S. Ouardi, Dr. B. Balke, Prof. C. Felser
Institut of Inorganic and Analytical Chemistry
University of Mainz
Staudingerweg 9, 55099 Mainz, Germany
E-mail: balke@uni-mainz.de
M. Schwall, L. M. Schoop,
Graduate School Material Science in Mainz
University of Mainz
Staudingerweg 9, 55099 Mainz, Germany
P. Klaer, Prof. H.-J. Elmers
Institut of Physics
University of Mainz
Staudingerweg 7, 55099 Mainz, Germany

DOI: 10.1002/adfm.201102792

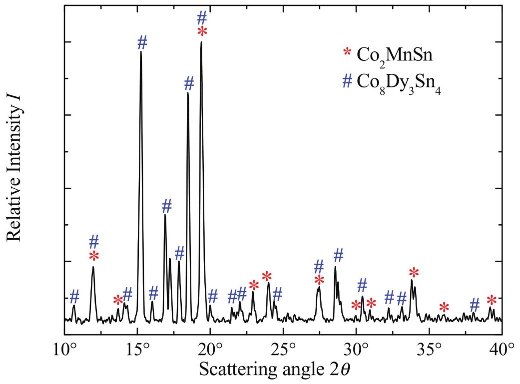

**Figure 1.** XRD pattern of the phase-separated $Co_2Dy_{0.5}Mn_{0.5}Sn$ alloy.

symmetry pattern. While the Co concentration is equally distributed, the Dy forms a flower-like sixfold pattern. The Dy-rich regions have a small concentration of Mn and vice versa. Sn also shows a more or less homogeneous distribution except in small regions at the grain boundaries. A linear combination of the element-specific EDX mappings shown in Figure 2b, reveals three distinct phases. Region I (light blue) shows a sixfold flower pattern embedded in region II (violet). Region III (green) fills the interstitial space inbetween region II.

The energy-dispersive X-ray (EDX) line-scan shown in Figure 2c quantifies the stoichiometry of the three regions. Region I with composition $Co_{1.95}Dy_{0.84}Mn_{0.26}Sn_{0.95}$ has the lowest Mn concentration and forms the flower-like sixfold pattern surrounded by region II with a sixfold pattern $Co_{1.95}Dy_{0.84}Mn_{0.26}Sn_{0.95}$ structure. The compositions are formally close to the Heusler alloy $Co_xDy_xMn_{1-x}Sn$. Region III consists of an intermediate composition $Co_2Dy_{0.83}Mn_{0.45}Sn_{0.72}$.

The structure in the lower left corner of Figure 2b reveals an inner pattern, roughly repeating the sixfold flower-like pattern on a smaller scale. All three phases reveal inhomogeneities that could hardly be resolved by EDX. Taking into account the XRD analysis, that has identified cubic $L2_1$ ordered $Co_2MnSn$ and hexagonal $Co_8Dy_3Sn_4$ as pure constituent phases, the observed stoichiometry for region I and II may be interpreted in the following way: region I is dominated by the $Co_8Dy_3Sn_4$ with additional inclusions of $Co_2MnSn$ amounting to 20% volume fraction and region II is dominated by $Co_2MnSn$ with an amount of 10%. The scanning electron microscopy (SEM) and EDX measurements on a surface cut parallel to the temperature gradient reveals parallel stripes at up 1 mm length that can be clearly identified with regions I, region II, and region III. In contrast, EDX images on surfaces perpendicular to the temperature gradient show the flower-like structure (Figure 2). A sketch of the resulting 3D structure is shown in **Figure 3**.

The 3D cellular microstructure is formed by a dendritic crystal growth similar to observations for binary alloys, e.g., Pb-Sn.[29] The different melting points of $Co_2MnSn$ and $Co_8Dy_3Sn_4$ are most likely the origin of the observed cellular microstructure. $Co_8Dy_3Sn_4$, with the highest melting point, solidifies as the observed region I in the remaining liquid phase. The sixfold pattern formation in region I originates from the strong epitaxial strain imposed by the hexagonal $Co_8Dy_3Sn_4$ phase with the cubic $Co_2MnSn$ phase formed during the solidifying process.

A phase separation has also been observed for the Heusler alloys $Co_2Mn_{1-x}Ti_xSn$ and $CoTi_{1-x}Mn_xSb$.[22,30] These alloys exhibit a separation into two Heusler phases, but they show a rather irregular structure. Moreover, the phase separation disappears after high temperature annealing, in contrast to the compound discussed here.

### 2.3. Magnetic Properties

**Figure 4**a shows the magnetization as a function of the sample temperature. Two magnetic phase transitions occur at different Curie temperatures $T_{C,1} = 95 \pm 10$ K and $T_{C,2} = 830 \pm 10$ K. The $T_C$ values were determined by fitting the temperature dependent magnetization with $M(t) = M_0(1 - T/T_C)^{1/2}$ as obtained from the mean field theory.[31] Previous measurements have shown that $Co_2MnSn$ has a Curie temperature of $T_C = 830$ K.[9]

Therefore, the $T_{C,2}$ can be attributed to this phase. $T_{C,1}$ is likely the Curie temperature of $Co_8Dy_3Sn_4$. For pure $Co_8Dy_3Sn_4$ we found a Curie temperature of $T_C = 70 \pm 10$ K in good agreement with $T_{C,1}$. Figure 4b shows for the phase separated compound the field-dependent magnetization above and below $T_{C,1}$.

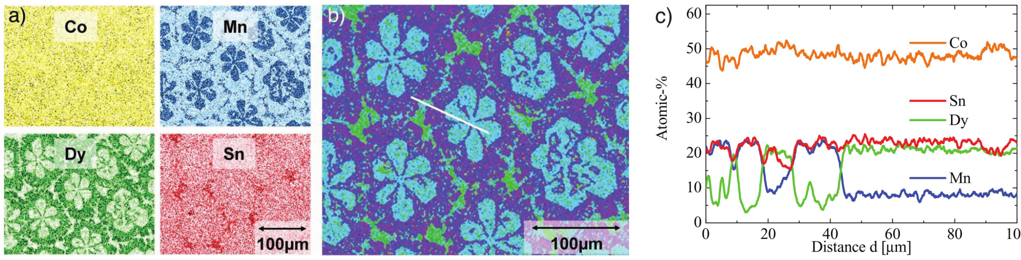

**Figure 2.** a) Element-specific (EDX) mappings of the four constituents of the phase separated $Co_2Dy_{0.5}Mn_{0.5}Sn$ alloy with brightness proportional to the concentration. b) Linear combina-tion of the EDX mapping shown in (a) revealing three distinct regions with different compositions: region I (light blue), region II (violet), and region III (green). c) Line-scan along the path (white line) indicated in (b).

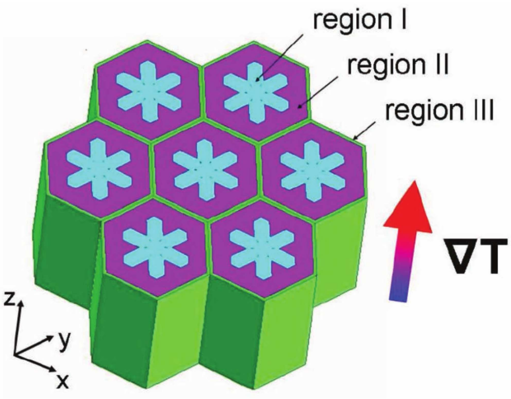

**Figure 3.** Sketch of the 3D phase-separated $Co_2Dy_{0.5}Mn_{0.5}Sn$ alloy. The temperature gradient $\nabla T$ is along the $z$ direction.

At 5 K both phases are ferromagnetic, which explains the large saturation magnetization. At 300 K only $Co_2MnSn$ exhibits ferromagnetic behavior, resulting in a much smaller magnetization. The $M(H)$ curve at 300 K reveals a coercive field of $H_{c,2} = 9 \times 10^{-4}$ T. This comparatively small coercive field is on the order of magnitude observed for other Co-based Heusler alloys and indicates soft magnetic behavior.[32] At 5 K, however, the coercive field $H_{c,1} = 0.130$ T is much larger due to the crystal anisotropy of the $Co_8Dy_3Sn_4$ alloy.

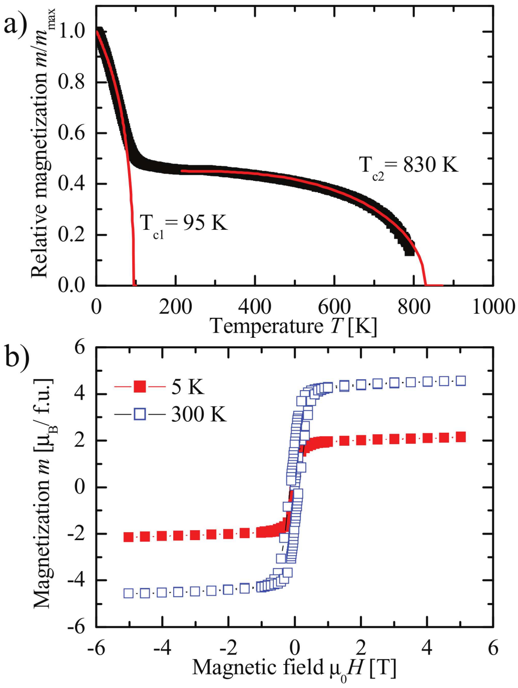

**Figure 4.** a) Temperature-dependent magnetization of phase separated $Co_2Dy_{0.5}Mn_{0.5}Sn$. The measurements were performed in an induction field of 1 T. b) Field-dependent magnetization at 5 K and 300 K in units of Bohr magnetons per formula unit ($\mu B$ f.u.$^{-1}$).

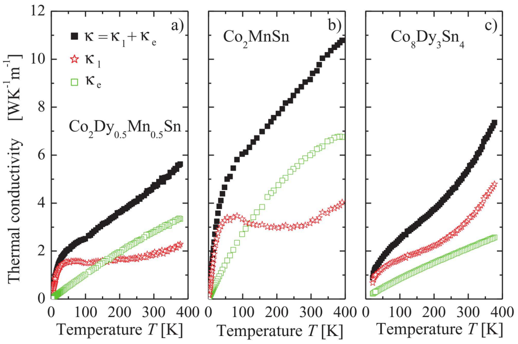

**Figure 5.** Temperature-dependent thermal conductivity of a) $Co_2Dy_{0.5}Mn_{0.5}Sn$, b) $Co_2MnSn$, and c) $Co_8Dy_3Sn_4$. Shown are the thermal conductivity, the lattice thermal conductivity and the electronic contribution to the thermal conductivity, calculated using the Wiedemann-Franz law.

### 2.4. Thermoelectric Properties

**Figure 5** shows the thermal conductivity of the phase separated $Co_2Dy_{0.5}Mn_{0.5}Sn$ sample compared with the Heusler alloy $Co_2MnSn$ and $Co_8Dy_3Sn_4$. The electronic contribution to the thermal conductivity $\kappa_e$ was calculated using the Wiedemann-Franz Law:[18]

$$\kappa_e = L\sigma T = \frac{LT}{\rho} \tag{1}$$

where $L$ is the Lorenz number ($2.44 \times 10^{-8}$ W Ω K$^{-2}$[33]), $\sigma$ is the electric conductivity, $\rho$ is the electric resistivity, and $T$ is the absolute temperature. With the relation

$$\kappa = \kappa_e + \kappa_l \tag{2}$$

the lattice contribution to the thermal conductivity $\kappa_l$ was calculated. In comparison to $Co_2MnSn$ the electronic part of the thermal conductivity of $Co_2Dy_{0.5}Mn_{0.5}Sn$ is lower due to the slightly higher resistivity (**Figure 6**). The higher resistivity is probably an effect of the phase separation because there are more grain and phase boundaries than in the $Co_2MnSn$ sample. Electrons are scattered more often at these grain boundaries. The resistivity of $Co_8Dy_3Sn_4$ is slightly higher than in the mixed compound leading to a lower electronic contribution to the thermal conductivity. The lattice thermal conductivity is about one third lower for $Co_2Dy_{0.5}Mn_{0.5}Sn$ than for $Co_2MnSn$. In comparison with $Co_8Dy_3Sn_4$, $K_l$ is slightly lower than the mixed phase up to 250 K. Above 250 K the lattice thermal conductivity of $Co_8Dy_3Sn_4$ increases strongly and is about 40% higher than that of $Co_2Dy_{0.5}Mn_{0.5}Sn$.

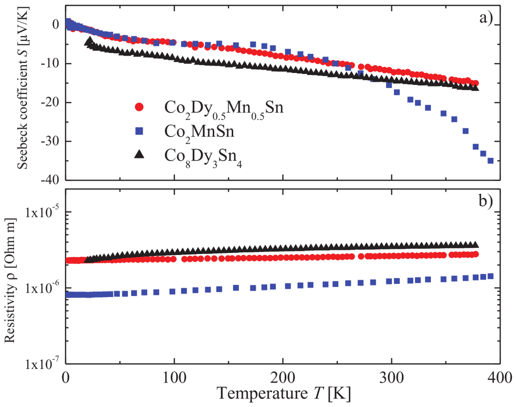

**Figure 6.** a) Seebeck coefficient and b) electrical resistivity for $Co_2Dy_{0.5}Mn_{0.5}Sn$, $Co_2MnSn$, and $Co_8Dy_3Sn_4$.

The lower $\kappa_l$ value can be explained by the phase separation as well. The additional grain boundaries act as very efficient scattering centers for phonons and electrons, thus decreasing the thermal conductivity.

The lattice thermal conductivity is expected to show a maximum at intermediate temperatures due to a compensation of the increasing number of phonons contributing to the transport and increasing contribution from Umklapp processes causing scattering with increasing temperature. The additional scattering at grain boundaries cause a temperature-independent decrease of $\kappa_l$. This expected temperature dependence of $\kappa_l(T)$ is observed at lower temperatures with the maximum located at $T = 50$ K. The slight increase of the lattice thermal conductivity near 300 K can be explain by a temperature-dependent Lorenz number instead of a constant used here for the calculation of the electronic contribution to the thermal conductivity. The lattice thermal conductivity of $Co_8Dy_3Sn_4$ shows a typical behavior of a compound with a complex unit cell in a quasicrystal or amorphous metals.[34,35] $\kappa_l(T)$ can be divided into three intervals. In interval I (0–75K) the thermal conductivity increases linearly. Interval II (75–150 K) covers an almost constant $\kappa_l(T)$. In interval III ($T > 150$ K) $\kappa(T)$ increases with increasing temperature. Interval I is determined by an almost constant mean free path of the phonons, which is limited by extrinsic defects like grain boundaries, defects, or lattice distortions. In interval II, the plateau, all available phonons are saturated in the Dulong–Petit limit.[35] Interval III can be explained by the interaction of high-energy critical modes with low-energy extended phonons similar to the phonon-assisted fraction hopping in glasses.[34,35] Electrical resistivities show metallic behavior, i.e., resistivity in-creases with increasing temperature. The resistivity of $Co_2Dy_{0.5}Mn_{0.5}Sn$ is a factor of two larger. As mentioned above this is probably an effect of the phase separation. $Co_8Dy_3Sn_4$ shows a slightly higher resistivity than the mixed compound.

The Seebeck coefficient was also measured and the samples exhibit a negative Seebeck coefficient indicating n-type conduction. The Seebeck coefficient of $Co_2MnSn$ decreases above 250 K to a value of –35 µV $K^{-1}$ at 400 K. The Seebeck coefficient of $Co_2Dy_{0.5}Mn_{0.5}Sn$ decreases linearly with temperature in the total measured temperature range between 2 K to 400 K. Similar behavior is seen for $Co_8Dy_3Sn_4$. The electronic properties of the mixed compound $Co_2Dy_{0.5}Mn_{0.5}Sn$ seem to be dominated by the electronic properties of $Co_8Dy_3Sn_4$.

## 3. Conclusions

In summary, it has been shown that grain boundaries between structurally different grains can reduce the lattice thermal conductivity $\kappa_l$ significantly. The lattice thermal conductivity of $Co_2Dy_{0.5}Mn_{0.5}Sn$ is lower than the mean value of the $\kappa_l$ of the constituent phases. This is a consequence of the phase separation, which is temperature-stable over a wide temperature range. The temperature dependence of the magnetization reflects the phase separation into two main phases. In contrast, the magnetization curve indicates a homogeneous magnetization rotation with a large coercive field dominated by the $Co_8Dy_3Sn_4$ phase at low temperature. The Seebeck effect and the electronic resistivity in the phase separated compound are dominated by the $Co_8Dy_3Sn_4$ phase. The results of this study show that the obstacle of a large lattice thermal conductivity commonly observed for Heusler compounds can be removed by a temperature-stable phase separation. Further improvements are expected from an increase of the Seebeck coefficient by optimization of the carrier concentration through hole or electron doping.

## 4. Experimental Section

$Co_2Dy_{0.5}Mn_{0.5}Sn$ samples were prepared by arc melting of stoichiometric amounts of the constituents (Co 99.95%, Dy 99.9%, Mn 99.99%, Sn 99.99% from Chempur) in an argon atmosphere of 10 mbar. The samples were remelted several times to increase their homogeneity. The resulting polycrystalline ingots were annealed at 1273 K in an evacuated quartz tube for 7 days afterwards. The crystalline structure was determined by XRD using excitation by Mo $K_{\alpha1,2}$ radiation(Bruker, AXS D8). A scanning electron microscope (Jeol JSM-6400) equipped with an EDX detection system (EUMEX EDX) was used to identify the microstucture and local stoichiometry of the phase-separated compound. The measurements were carried out at a pressure of $3 \times 10^{-6}$ mbar. An acceleration voltage of 20 kV was applied and an inspection angle of 35° was set up. For the correction of the quantitative data the ZAF method was applied, which relies on atomic number (*Z*), absorption (*A*), and fluorescence (F) effects. The magnetic properties were investigated by a super-conducting quantum interference device (SQUID, Quantum Design MPMS-XL-5) using nearly punctual pieces of approximately 10 mg of the sample. The transport properties were investigated using a Physical Property Measurement System (PPMS, Quantum Design). For transport measurements the samples were cut into bars with the approximate dimensions $2 \times 2 \times 10$ $mm^3$. The samples were polished immediately before contacting in order to remove oxide layers. The bars were contacted with four copper leads that were wrapped around the bars to homogenize the current passing through. The sample chamber was flooded with helium and evacuated afterwards. The transport measurements were carried out at a pressure of $1.2 \times 10^{-4}$ mbar by a standard four point ac method.

## Acknowledgements

The authors gratefully acknowledge the financial support by the “thermoHeusler” Project (Project No. 0327876D) of the German

[1] F. Heusler, Verh. d. DPG **5**, 219 (1903).

[2] L. O. Grondahl and S. Karrer, Physical Review Series I **33**, 531 (1911).

[3] C. S. Birkel, W. G. Zeier, J. E. Douglas, B. R. Lettiere, C. E. Mills, G. Seward, A. Birkel, M. L. Snedaker, Y. Zhang, G. J. Snyder, et al., Chemistry of Materials **24**, 2558 (2012).

[4] G. Joshi, T. Dahal, S. Chen, H. Wang, J. Shiomi, G. Chen, and Z. Ren, Nano Energy (2012).

[5] J. W. Simonson, D. Wu, W. J. Xie, T. M. Tritt, and S. J. Poon, Phys. Rev. B **83**, 235211 (2011).

[6] H. Hazama, M. Matsubara, and R. Asahi, Journal of Electronic Materials **41**, 1730 (2012).

[7] H.-H. Xie, J.-L. Mi, L.-P. Hu, N. Lock, M. Chirstensen, C.-G. Fu, B. B. Iversen, X.-B. Zhao, and T.-J. Zhu, CrystEngComm **14**, 4467 (2012).

[8] M.-S. Lee, F. P. Poudeu, and S. D. Mahanti, Phys. Rev. B **83**, 085204 (2011).

[9] Y. Gelbstein, N. T. Aviad Yarmek, Y. Rosenberg, M. P. Dariel, S. Ouardi, B. Balke, C. Felser, and M. Köhne, Journal of Materials Research **26** (2011).

[10] B. Balke, J. Barth, M. Schwall, G. Fecher, and C. Felser, Journal of Electronic Materials **40**, 702 (2011).

[11] H.-H. Xie, C. Yu, T.-J. Zhu, C.-G. Fu, G. J. Snyder, and X.-B. Zhao, Applied Physics Letters **100**, 254104 (2012).

[12] T. Jaeger, C. Mix, M. Schwall, X. Kozina, J. Barth, B. Balke, M. Finsterbusch, Y. U. Idzerda, C. Felser, and G. Jakob, Thin Solid Films **520**, 1010 (2011).

[13] M. Mikami, Y. Kinemuchi, K. Ozaki, Y. Terazawa, and T. Takeuchi, Journal of Applied Physics **111**, 093710 (2012).

[14] J. P. A. Makongo, D. K. Misra, X. Zhou, A. Pant, M. R. Shabetai, X. Su, C. Uher, K. L. Stokes, and P. F. P. Poudeu, Journal of the American Chemical Society **133**, 18843 (2011).

[15] M. A. Verges, P. J. Schilling, P. Upadhyay, W. K. Miller, R. Yaqub, K. L. Stokes, and P. F. Poudeu, Science of Advanced Materials **3** (2011).

[16] P. Klaer, M. Kallmayer, C. G. F. Blum, T. Graf, J. Barth, B. Balke, G. H. Fecher, C. Felser, and H. J. Elmers, Phys. Rev. B **80**, 144405 (2009).

[17] P. Klaer, T. Bos, M. Kallmayer, C. G. F. Blum, T. Graf, J. Barth, B. Balke, G. H. Fecher, C. Felser, and H. J. Elmers, Phys. Rev. B **82**, 104410 (2010).

[18] M. Schwall and B. Balke, Appl. Phys. Lett. **98**, 042106 (2011).

[19] H. Hohl, A. Ramirez, W. Kaefer, K. Fess, C. Thurner, C. Kloc, and E. Bucher, Mater. Res. Soc. Symp. Proc. p. 109 (1997).

[20] H. Hohl, A. Ramirez, C. Goldmann, G. Ernst, B. Wolfing, and E. Bucher, J. Phys.: Condens. Matter **11**, 1697 (1999).

[21] T. Graf, J. Barth, C. G. F. Blum, B. Balke, C. Felser, P. Klaer, and H. J. Elmers, Phys. Rev. B **82**, 194420 (2010).

[22] T. Graf, P. Klaer, J. Barth, B. Balke, H. J. Elmers, and C. Felser, Scripta Materialia **63**, 1216 (2010).

[23] M. Schwall, L. M. Schoop, S. Ouardi, B. Balke, C. Felser, P. Klaer, and H.-J. Elmers, Advanced Functional Materials **22**, 1773 (2012).

[24] J. S. Tse and D. D. Klug, *CRC Thermoelectrics Handbook - MACRO TO NANO* (CRC Thermoelectrics Handbook - MACRO TO NANO, 2006).

[25] C. Wood, Reports on Progress in Physics **51**, 459 (1988).

[26] T. M. Tritt and M. A. Subramanian, MRS Bulletin **31**, 188 (2006).

[27] G. J. Snyder and E. S. Toberer, Nature Materials **7**, 105 (2008).

[28] J. M. Ziman and P. W. Levy, Physics Today **14**, 64 (1961).

[29] H. J. Goldsmid and P. L. Balise, Physics Today **14**, 72 (1961).

[30] J. Sootsman, D. Chung, and M. Kanatzidis, Angewandte Chemie International Edition **48**, 8616 (2009).

[31] J. P. Heremans, V. Jovovic, E. S. Toberer, A. Saramat, K. Kurosaki, A. Charoenphakdee, S. Yamanaka, and G. J. Snyder, Science **321**, 554 (2008).

[32] N. F. Mott and H. Jones, *The theory of the properties of metals and alloys* (1958).

[33] P. A. Cox, *The Electronic Structure And Chemistry of Solids* (Oxford University Press, 1987).

[34] E. S. Toberer, A. F. May, and G. J. Snyder, Chemistry of Materials **22**, 624 (2010).

[35] A. F. May, E. S. Toberer, A. Saramat, and G. J. Snyder, Phys. Rev. B **80**, 125205 (2009).

[36] J. Yang, in *Thermal Conductivity*, edited by T. Tritt (Springer US, 2004), Physics of Solids and Liquids, pp. 1–20.

[37] A. Sommerfeld and H. Bethe, vol. 24 (Handbuch der Physik, 1933), 2nd ed.

[38] A. J. Minnich, M. S. Dresselhaus, Z. F. Ren, and G. Chen, Energy Environ. Sci. **2**, 466 (2009).

[39] V. Murashov and M. A. White, in *Theory of Thermal Conductivity*, edited by T. Tritt (2004),

chap. 1.3, pp. 93–104.

[40] P. F. P. Poudeu, J. D'Angelo, A. D. Downey, J. L. Short, T. P. Hogan, and M. G. Kanatzidis, Angewandte Chemie International Edition **45**, 3835 (2006).

[41] R. W. Keyes, Physical Review **115**, 564 (1959).

[42] F. Heusler, Angewandte Chemie **17**, 260 (1904).

[43] F. Heusler, Zeitschrift für anorganische Chemie **88**, 185 (1914).

[44] F. Heusler and F. Richarz, Zeitschrift für anorganische Chemie **61**, 265 (1909).

[45] O. Heusler, Zeitschrift für anorganische und allgemeine Chemie **159**, 37 (1927).

[46] O. Heusler, Zeitschrift für anorganische und allgemeine Chemie **171**, 126 (1928).

[47] F. Heusler, Zeitschrift für anorganische und allgemeine Chemie **161**, 159 (1927).

[48] J. Young, Philosophical Magazine Series 6 **46**, 291 (1923).

[49] A. J. Bradley and J. W. Rodgers, Royal Society of London Proceedings Series A **144**, 340 (1934).

[50] D. Jung, H. J. Koo, and M. H. Whangbo, J. Molec. Struct. Theochem. **527**, 113 (2000).

[51] J. Pierre, R. V. Skolozdra, Y. K. Gorelenko, and M. A. Kouacou, J. Magn. Magn. Mater. **134**, 95 (1994).

[52] J. Tobola, J. Pierre, S. Kaprzyk, R. V. Skolozdra, and M. A. Kouacou, J. Phys. Condens. Matter **10**, 1013 (1998).

[53] D. A. Porter, K. E. Easterling, and M. Y. Sherif, *Phase Transformation in Metals and Alloys* (CRC Press, 2009).

[54] J. Freudenberger and L. Schultz, in *Physikalische Werkstoffeigenschaften* (2010), chap. 9, p. 151.

[55] R. Nicholson, G. Thomas, and J. Nutting, journal of the Institute of Metals **87**, 431 (1958-1959).

[56] G. Chadwick, *Metallography of Phase Transformations* (Butterworths, 1972).

[57] F. R. N. Nabarro, Proceedings of the Royal Society of London. Series A. Mathematical and Physical Sciences **175**, 519 (1940).

[58] J. P. Heremans, B. Wiendlocha, and A. M. Chamoire, Energy Environ. Sci. **5**, 5510 (2012).

[59] J. Korringa and A. Gerritsen, Physica **19**, 457 (1953).

[60] K. Ahn, M.-K. Han, J. He, J. Androulakis, S. Ballikaya, C. Uher, V. P. Dravid, and M. G. Kanatzidis, Journal of the American Chemical Society **132**, 5227 (2010).

[61] G. D. Mahan and J. O. Sofo, Proceedings of the National Academy of Sciences **93**, 7436 (1996).

[62] L. D. Hicks and M. S. Dresselhaus, Phys. Rev. B **47**, 16631 (1993).

[63] S. Alexander, O. Entin-Wohlman, and R. Orbach, Phys. Rev. B **34**, 2726 (1986).

[64] C. Janot, Phys. Rev. B **53**, 181 (1996).

[65] G. Wiedemann and R. Franz, Ann. Phys. **165**, 497 (1853).

[66] T. Graf, P. Klaer, J. Barth, B. Balke, H.-J. Elmers, and C. Felser, Scripta Materialia **63**, 1216 (2010).

[67] T. Graf, J. Barth, C. Blum, B. Balke, P. Klaer, H.-J. Elmers, and C. Felser, Phys. Rev. B **82**, 104420 (2010).

[68] Y. Gelbstein, Y. Rosenberg, Y. Sadia, and M. Dariel, J. Phys. Chem. C **114**, 13126 (2010).

[69] M. Hatami, G. E. W. Bauer, Q. Zhang, and P. J. Kelly, Phys. Rev. B **79**, 174426 (2009).

[70] F. Canepa, S. Cirafici, M. Fornasini, P. Manfrinetti, F. Merlo, A. Palenzona, and M. Pani, Journal of Alloys and Compounds **297**, 109 (2000).

[71] S. Tewari, R. Shah, and H. Song, Metallurgical and Materials Transactions A **25**, 1535 (1994).

[72] T. Graf, G. H. Fecher, J. Barth, J. Winterlik, and C. Felser, Journal of Physics D: Applied Physics **42**, 084003 (2009).

[73] B. Balke, S. Ouardi, T. Graf, J. Barth, C. G. Blum, G. H. Fecher, A. Shkabko, A. Weidenkaff, and C. Felser, Solid State Communications **150**, 529 (2010).

[74] B. Balke, G. H. Fecher, H. C. Kandpal, C. Felser, K. Kobayashi, E. Ikenaga, J.-J. Kim, and S. Ueda, Phys. Rev. B **74** (2006).

[75] Y. Kimura, T. Kuji, A. Zama, Y. Shibata, and Y. Mishima, MRS Proceedings **886** (2005).

[76] N. Shutoh and S. Sakurada, Journal of Alloys and Compounds **389**, 204 (2005).

[77] S. Sakurada and N. Shutoh, Applied Physics Letters **86**, 082105 (pages 3) (2005).

[78] S. R. Culp, J. W. Simonson, S. J. Poon, V. Ponnambalam, J. Edwards, and T. M. Tritt, Applied Physics Letters **93**, 022105 (2008).

[79] T. Sekimoto, K. Kurosaki, H. Muta, and S. Yamanaka, Thermoelectrics, 2006. ICT ’06. 25th International Conference on thermoelectrics (2006).

[80] S. R. Culp, J. W. Simonson, S. J. Poon, V. Ponnambalam, J. Edwards, and T. M. Tritt, Applied Physics Letters **93**, 022105 (2008).

[81] T. Wu, W. Jiang, X. Li, Y. Zhou, and L. Chen, Journal of Applied Physics **102**, 103705

(2007).

[82] X. Yan, G. Joshi, W. Liu, Y. Lan, H. Wang, S. Lee, J. W. Simonson, S. J. Poon, T. M. Tritt, G. Chen, et al., Nano Letters **11**, 556 (2011).

[83] P. Romans, O. Paasche, and H. Kato, Journal of the Less Common Metals **8**, 213 (1965).

[84] S. Ouardi, G. H. Fecher, C. Felser, M. Schwall, S. S. Naghavi, A. Gloskovskii, B. Balke, J. Hamrle, K. Postava, J. Pištora, et al., Phys. Rev. B **86**, 045116 (2012).

[85] S. Ouardi, G. H. Fecher, B. Balke, X. Kozina, G. Stryganyuk, C. Felser, S. Lowitzer, D. Ködderitzsch, H. Ebert, and E. Ikenaga, Phys. Rev. B **82**, 085108 (2010).